Transient bioheat transfer analysis in biological tissues by fundamental-solution-based numerical methods

Zewei Zhang

A Thesis Submitted for the Degree of Doctor of Philosophy

of

The Australian National University

March 2015

Declaration

This thesis is an account of work undertaken between March 2010 and March 2015 in the School of Engineering at the Australian National University, Acton, Australia.

This thesis contains no material that has been previously accepted for the award of any other degree in any university, and contains no material previously published or written by another person, except where acknowledged in the customary manner.

Zewei Zhang

June 2015

Publications

Ze-Wei Zhang, Hui Wang, Qing-Hua Qin, Transient Bioheat Simulation of the Laser-Tissue Interaction in Human Skin Using Hybrid Finite Element Formulation, *Molecular & Cellular Biomechanics*, 2012, 9(1), 31-53 (Journal Paper)

Ze-Wei Zhang, Hui Wang, Qing-Hua Qin, Method of Fundamental Solutions for Nonlinear Skin Bioheat Model, *Journal of Mechanics in Medicine and Biology*, 2014, 14(4), 1450060 (20 pages) (Journal Paper)

Zewei Zhang, Hui Wang, Qing-Hua Qin, Meshless Method with Operator Splitting Technique for Transient Nonlinear Bioheat Transfer in Two-dimensional Skin Tissues, *International Journal of Molecular Sciences*, 2015, 16(1), 2001-2019 (Journal Paper)

Ze-Wei Zhang, Hui Wang, Qing-Hua Qin, Analysis of Transient Bioheat Transfer in the Human Eye Using Hybrid Finite Element Model, presented on the First Australasian Conference on Computational Mechanics (ACCM2013), 3rd-4th, October, 2013, Sydney, Australia. *Applied Mechanics and Materials*, 2014, 553, 356-361 (Conference paper)

Acknowledgements

I would like to express thanks from the bottom of my heart to my supervisor, Prof. Qing-Hua Qin, who has provided outstanding guidance, supervision, encouragement and support in my project.

I also thank Dr. Hui Wang and Dr. Yi Xiao for their advice and discussion. I also express my gratitude to the administrators of the School of Engineering for their help and general support on a daily basis.

I also offer my regards and gratitude to all those who supported me in any respect during the completion of the project, especially our biomechanics research group members: Leilei Cao, Jin Tao, Cheuk-Yu Lee, Changyong Cao and Song Chen.

Last, I thank my parents. Most importantly, special thanks go to my wife Wenjia for her love and support.

Abstract

In this thesis, fundamental-solution-based numerical methods, namely the hybrid finite element method with element boundary integrals and the meshless method of fundamental solutions, were developed for solving two-dimensional (2D) bioheat transfer problems, which are described by the Pennes bioheat transfer equation and related boundary conditions.

First, a fundamental-solution-based hybrid finite element method (HFS-FEM) coupling radial basis functions (RBFs) was formulated for describing quantitatively the transient thermal response of skin tissue under laser irradiation. In this method, temporal discretization of the transient bioheat system of the laser-tissue interaction problem is conducted to convert the transient problem into the steady-state inhomogeneous modified Helmholtz equation problem, which is solved at each time step. Their corresponding particular and homogeneous solutions are respectively obtained by RBF interpolation and the HFS-FEM, in which two independent temperature fields linked by a two-variable variational functional are assumed to be a frame temperature field and an intra-element temperature field. The intra-element field is approximated through a linear combination of fundamental solutions at a number of source points outside the element domain, while the frame temperature field is expressed in

terms of nodal temperature and a shape function. Numerical results from the developed approach were validated by comparison with analytical solutions, and good agreement was observed. Then, sensitivity analysis was performed by tuning certain control parameters such as the ambient convection coefficient, ambient temperature, laser power and tissue heat conductivity. The burn degree of skin tissue was evaluated at different levels of power laser radiation. Additionally, simulation of transient bioheat transfer in 2D human eye tissue was conducted using the developed method. The results obtained were compared with those from ABAQUS and good agreement was also observed.

Secondly, the method of fundamental solution (MFS) coupled with the dual reciprocity method (DRM) was developed to solve steady-state nonlinear bioheat transfer problems, in which the temperature-dependent blood perfusion rate is under consideration. Taylor’s expansion approach was applied to linearize the nonlinear term in the original nonlinear bioheat transfer governing equation. Then the meshless strategy combining the DRM and the MFS was established to obtain the particular and homogeneous solutions of the linear system, including the linearized governing equation and the specific boundary conditions. To demonstrate the accuracy and efficiency of the proposed meshless method, the relation between the blood perfusion rate and the temperature was assumed to be linear, quadratic and exponential. The influence of blood perfusion rate on temperature distribution in the skin tissue was analysed by changing the coefficients in the three expressions of blood perfusion rate with respect to temperature. Numerical results showed that the variation of blood perfusion rate plays a significant role in the temperature distribution within the skin tissue, as the second and third coefficients in the expression of quadratic blood perfusion rate can cause evident temperature changes.

Finally, a meshless numerical scheme combining the operator splitting method (OSM), the RBF interpolation and the MFS was developed for solving transient nonlinear bioheat problems in two-dimensional skin tissue. In the numerical scheme, the nonlinearity caused by linear and exponential relationships of temperature-dependent blood perfusion rate (TDBPR) is taken into consideration. In the procedure, the OSM is used first to separate the Laplacian operator and the nonlinear source term, and then second-order time-stepping schemes are employed for approximating two splitting operators in order to convert the original governing equation into a linear nonhomogeneous Helmholtz-type governing equation (NHGE) at each time step. Subsequently, the RBF interpolation and the MFS involving the fundamental solution of the Laplace equation are respectively employed to obtain approximated particular and homogeneous solutions of the NHGE. Finally, the full fields consisting of the particular and homogeneous solutions are enforced to fit the NHGE at interpolation points and the boundary conditions at boundary collocations to determine unknowns at each time step. The proposed method was verified by comparison with other methods. Furthermore, the sensitivity of the coefficients in cases of a linear and an exponential relationship of TDBPR was investigated to reveal their bioheat effect on the skin tissue.

Contents

List of Tables

List of Figures

Acronym

AB: Adams-Bashforth

AEM: analog equation method

AM: Adams-Moulton

BEM: boundary element method

CS-RBF: piecewise polynomial compactly supported RBF

DRBEM: dual reciprocity boundary element method

DRM: dual reciprocity method

DRM-MFS: method of fundamental solutions coupled with the dual reciprocity method

FEM: finite element method

GS-RBF: globally supported RBF

HFS-FEM: fundamental-solution-based hybrid finite element method

L-TKP: laser thermokeratoplasty

MFS: method of fundamental solutions

NHGE: nonhomogeneous Helmholtz-type governing equation

OSM: operator splitting method

PDEs: partial differential equations

RBFs: radial basis functions

TDBPR: temperature-dependent blood perfusion rate

TPS: thin plate spline

2D, 3D: two-dimensional, three-dimensional

Chapter 1 Introduction

1.1 Basic Tissue Bioheat Transfer Biology

Bioheat transfer in tissue includes heat generation, heat absorption, heat transmission, evaporation, heat radiation and conduction, etc. [1-9]. It is a very complex process which couples with temperature distribution, tissue strain, stress on tissue and thermal damage of tissue [10-14].

As an example of biological tissue, the skin tissue shown in Figures 1.1 and 1.2 [1, 2] contains three layers consisting of subcutaneous tissue, dermis and epidermis. Bioheat transfer in skin tissue is mainly a heat conduction process with blood perfusion, sweating, bioheat metabolic, heat generation and conduction between skin tissue and the outside surface environment [15-17]. Many factors, such as thermal properties, temperature, skin tissue damage, age of human, pressure on the skin, etc., affect the bioheat transfer process in skin tissue [18, 19].

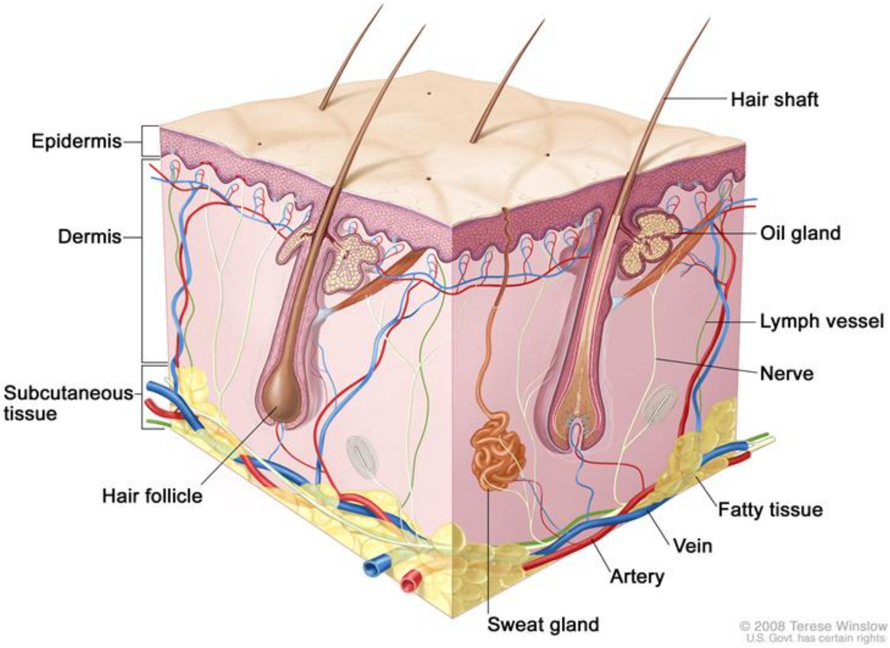

Figure 1.1 Anatomy of the human skin

(http://www.cancer.gov/cancertopics/pdq/treatment/skin/Patient/page1)

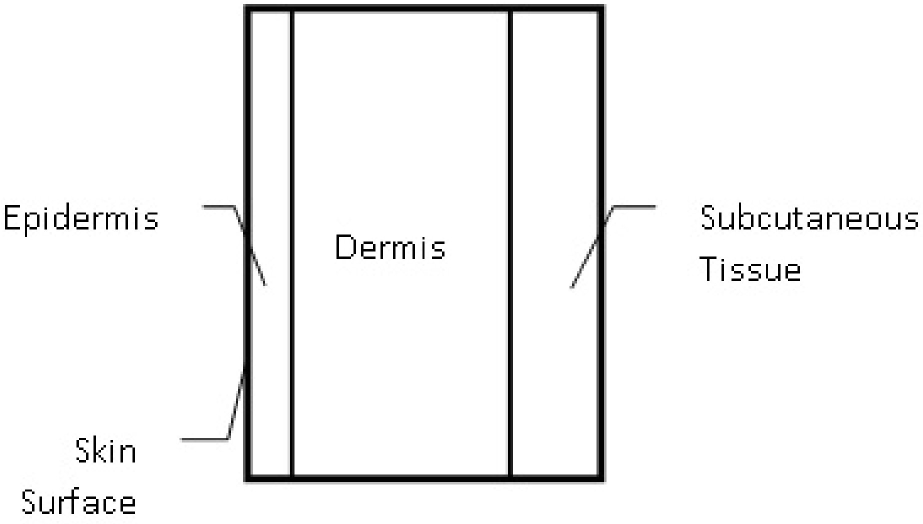

Figure 1.2 Simplified model of three-layered skin

As another example of biological tissue, there are five parts in a human eyeball, the cornea, aqueous humor, lens, vitreous and sclera [20]. Some tissue layers such as the retina and choroid can be neglected due to their thickness [21-23]. Each of the parts has different material properties such as thermal conductivity, density and specific heat [23-25]. In the Cartesian coordinate system, the bioheat transfer in biological tissue such as the skin and human eyeball is generally described by the well-known Pennes equation [23, 26, 27]. How to efficiently solve the bioheat system and establish effective prediction of thermal distribution in biological tissue is always of interest and the results can be useful for accurate assessment of burn severity, thermal protection, etc.

1.2 Research Background

Prediction of tissue temperature distribution in a biological system is required in many diagnostic applications to biological systems. For example, doctors would like to know heat and temperature changes during surgery on a skin tumour or the human eye so that they can adjust the power of laser therapy to avoid extra burning injury of healthy tissue [1, 28-32]. Cost and other factors may preclude real time measurement of temperature distribution [33], and also its theoretical solution is very difficult in real tissue structure due to its complex geometry and loading conditions. Therefore, numerical simulation of bioheat transfer may be more attractive and necessary in practical noninvasive diagnostics than theoretical and experimental predictions.

Some numerical methods have been widely developed to simulate and analyse bioheat transfer behaviours for various skin materials. Linear or nonlinear steady-state bioheat models involving changed thermal conductivity and blood perfusion rate have been numerically solved to analyse the induced temperature distribution in biological tissues [34-37]. A non-Fourier heat conduction model in one-dimensional multilayered systems has been analysed by Laplace transform and the fast inversion technique [16, 38, 39]. For instance, Marqa et al. investigated bioheat and thermal damage behaviour under laser irradiation using the conventional FEM [40], which was also used by Shibib to determine the thermal damage in human skin due to laser irradiation [41]. Ansari et al. studied short-pulse laser propagation in biological tissue by means of the boundary element method (BEM) with time-dependent fundamental solutions [42]. The Monte Carlo method and the dual reciprocity boundary element method (DRBEM) have also been applied to evaluate transient or steady-state thermal behaviours in biological tissues [43-45]. An axisymmetric boundary element formulation using the time-dependent fundamental solution was derived by Majchrzak for the analysis of freezing and thawing processes in biological tissues [46]. Xu et al. reviewed mathematical models and experimental methods to detail the progress of thermal damage in skin tissue [47]. For simplicity, some parameters in a complex biological system, such as blood perfusion rate and thermal conductivity, are generally assumed to be constants. As a result, the biological heat conduction system in skin tissues is usually approximated by a linear bioheat governing equation. Currently, the linear bioheat model has been well developed and simulated successfully using various numerical methods. However, these parameters actually change with temperature in the bioheat system, rather than remaining constant [35, 48, 49]. From the viewpoint of material, the skin can be viewed as a kind of functionally graded material for changed material properties with different location [50]. For this case, the commonly used linear biological system should be replaced by a nonlinear governing equation in order to obtain more accurate and reliable results.

Regarding nonlinear bioheat transfer, some research has been conducted to simulate the effect of TDBPR on temperature distribution in the biological system using numerical methods rather than analytical methods, because of the complexity of the nonlinear bioheat system. For example, Liu et al. used the DRBEM to investigate plane nonlinear bioheat skin model with linear and exponential case of TDBPR for tumour hyperthermia diagnostics [45]. Deng et al. also employed the

DRBEM to study the response of temperature and heat flux in a transient nonlinear biological model [51]. In their research work, three linear cases of TDBPRs with different constants were involved. The FEM was used by Kim et al. to investigate nonlinear temperature behaviour by introducing various blood perfusion rates in a model of laser coagulation of human tissue [52]. Their research indicated that tissue temperature could be significantly overestimated if the temperature dependence of blood perfusion rate was ignored. Similar conclusions were drawn by Drizdal et al. in their research into prediction of three-dimensional temperature distribution for superficial hyperthermia using the commercial finite element software, COMSOL Multi-physics package [53]. Among the numerical methods mentioned above, the DRBEM can be viewed as a mixed-boundary-type element method, which integrates the domain boundary discretization by the boundary element technique and domain interior collocation implemented by the simple basis function interpolation. Thus, only boundary integrals are included in the procedure of DRBEM. Unlike the DRBEM, the FEM is a classical domain-type element method, which employs domain discretization by large number of elements, based on a weak energy integral functional [54-58]. Therefore the domain integrals are involved.

Alternatively, a meshless method such as the method of fundamental solutions coupled with the dual reciprocity method (DRM-MFS) has also been well developed to predict the temperature distribution for linear bioheat transfer problems [59-62]. The kernel functions, that is, fundamental solutions, in the conventional MFS can theoretically be viewed as one type of Trefftz basis [63, 64]. The meshless DRM-MFS is a type of collocation method and is usually performed by allocating internal and boundary points in the solution domain to achieve the proper particular and homogeneous solutions, respectively. The particular solutions are usually approximated by the RBF interpolation at interior points, while the homogeneous solutions are approximated by constructing an explicit solution with the superposition of a finite number of source points on an artificial boundary, in terms of the fundamental solutions of the homogeneous problems. Since no mesh generation process and integrals are involved in the DRM-MFS procedure, it is purely meshless or mesh-free. Additionally, it can be easily implemented and programmed because of the ease of collocation. These are advantages of the meshless DRM-MFS over the element-type methods like the DRBEM and the FEM. Moreover, to deal with problems in which complex governing equations are encountered and no explicit fundamental solutions are available, the DRM-MFS has been improved by introducing the analog equation method (AEM) [65] for the solution of nonlinear steady-state heat conduction problems in anisotropic and isotropic inhomogeneous systems [61, 62]. Furthermore, some potential problems in the use of DRM-MFS have been discussed, such as the location of the virtual boundary, the differential and integrating strategies and the effect of shape parameter in a multiquadric basis [66].

In the context of transient nonlinear bioheat transfer, some numerical models have been developed for various biological tissues and nonlinear engineering problems [67-73] where there is a need to dynamically monitor the changes of temperature in time and space during the bioheat transfer process. For instance, Trakic et al. predicted the transient temperature rise in a nonlinear heat transfer model of tumour and healthy mouse tissue by the commercial finite element software FEMLAB [74]. Feng et al. applied finite element technology coupled with a nested-blocked optimization algorithm to predict the temperature distribution in a prostate during a nanoshell-mediated laser surgery [75].

It is noted that in these numerical methods, either the Laplace transform method or finite difference technology with respect to time has been applied to handle the time variable in the bioheat transfer governing equation. However, the Laplace transform method is usually limited to linear transient problems [76]. For other cases, the finite difference scheme needs careful consideration of the time step length to obtain accurate, stable and convergent results [77, 78]. These difficulties have motivated researchers to develop other methods for effective handling of the time derivative term and for approximating the nonlinear source terms in the governing equation. For example, the operator splitting method (OSM) for uniformly handling the transient term and nonlinear source term explicitly using two-level higher-order time step schemes has received considerable attention [79, 80].

In addition to numerical analysis of bioheat in skin tissue, some research has involved numerical results of bioheat transfer in eye tissues [81-87]. As well, Arunn et al. [88] investigated the variation of transient temperature in a 2D human eye computational model using the finite volume method. Ooi et al. [23] applied a time-stepping DRBEM to simulate corneal temperature during the treatment of laser thermokeratoplasty (L-TKP). The finite volume method developed by Chua et al. was able to calculate the temperature distribution in the human eyeball subjected to laser irradiation [22]. Brinkmann et al. [21, 89] developed a cylindrical eye model based on the FEM. Wang et al. evaluated the transient bioheat response in a two-dimensional human eye tissue by the FEM which was implemented by COMSOL. On the other hand, a novel HFS-FEM based on the fundamental solution was recently developed for human eye bioheat analysis [27, 90].

Among existing computational methods, Green's functions or fundamental-solution-based methods such as the BEM/DRBEM and the MFS have been successfully developed to obtain highly accurate numerical approximations of solutions to linear elliptic partial differential equations (PDEs) [91-93]. The use of fundamental solutions makes the boundary element or collocation discretization possible in these methods to preserve their boundary-only merits. As an alternative to the BEM and the MFS, another numerical method dependent of on fundamental solutions, the fundamental-solution-based HFS-FEM, was presented by Wang and Qin [94-99], which retains the advantages of both boundary integrals in the BEM [100-102], the eigenstrain boundary integral approach [103-105], and the flexible element division in the FEM [106, 107], and has been applied for solving thermal or elastic problems in human eyes [27], multilayer skins [108], functionally graded materials [109-112], fibre-reinforced composites [113-115], heat transfer problems [116-118], anisotropic materials [119, 120] and materials with defects or inclusions [102, 121-123]. In the proposed HFS-FEM formulation, the solution inside an element is approximated by a linear combination of fundamental solutions with sources located outside the element, as in the MFS [61, 66], and the conventional shape function interpolation is used to approximate the independent frame field defined over the element boundary. The linkage of the two groups of independent fields is established through the use of a two-variable hybrid variational functional.

1.3 Aims and Organisation of the Research

In this study, a HFS-FEM model coupled with the dual reciprocity technique is developed for analysing transient bioheat transfer of laser treatment in a skin tissue and heat transfer in a human eye. First, a backward time-stepping scheme is employed to perform the time discretization, leading to the inhomogeneous modified Helmholtz system. Then, the particular solution part of the inhomogeneous system is obtained using the interpolation of RBFs at a number of points in the solution domain. The homogeneous solution part is obtained using the hybrid FEM. Finally, numerical results are presented to verify and assess the numerical approach and to illustrate the effect of laser power on temperature distribution in a skin tissue.

To the author’s knowledge, the application of the DRM-MFS to nonlinear bioheat problems has not as yet been investigated. In this thesis, a meshless DRM-MFS is developed to determine temperature distribution in a nonlinear skin system in which the blood perfusion rate is assumed to be a function of temperature. For this, a two-dimensional skin tissue model with temperature-dependent blood perfusion is presented first. Then, solution procedures including AEM, the DRM, and the MFS are described. The numerical results from the proposed DRM-MFS are compared with those obtained via MATLAB PDE Toolbox. Sensitivity analysis for various blood perfusions is also included.

A further aim of this work is to develop a mixed meshless method for analysing transient nonlinear bioheat transfer in a 2D skin tissue by way of the OSM. In the proposed solution procedure, the OSM is employed first to isolate the transient and nonlinear terms in the original Penney bioheat governing equation by the explicit second-order Adams-Bashforth (AB) time-marching for the half time step and the second-order Adams-Moulton (AM) scheme for the next time step. Then, the new equation in the form of a modified Helmholtz equation can be derived and solved at each time step. Next, the mesh-free dual-reciprocity method implemented by the RBF interpolation and the mesh-free MFS in terms of fundamental solution kernels are respectively utilised to determine the particular solutions and the homogeneous solutions of the modified Helmholtz problem at each time step by simple internal and boundary collocations.

1.4 The Structure of the Thesis

This thesis is organised as follows: In Chapter 2, the basic formulations of bioheat transfer in biological tissues are reviewed. The formulations of fundamental solutions are also described. In Chapter 3, transient linear bioheat transfer is analysed in human skin under laser-tissue interaction. In Chapter 4, the nonlinear bioheat transfer in the steady state with TDBPR is analysed. In Chapter 5, the transient nonlinear bioheat transfer with TDBPR is analysed. Finally, in Chapter 6 the conclusion of this thesis is presented and possible future work is suggested. Parameter values and descriptions are listed in Appendix A and MATLAB code is attached in Appendix B.

Chapter 2 Basic Formulation of Bioheat Transfer in Tissues

2.1 General Bioheat Transfer Governing Equation

The bioheat transfer in biological tissue is adequately described by the well-known Pennes equation, which was introduced by Pennes in 1948 to model the temperature distribution in a human forearm [18], in the following general form [124]

$$k\nabla^2 T + \rho_b c_b \omega_b \left(T_a - T\right) + Q_m + Q_r = \rho c \frac{\partial T}{\partial t} \qquad \mathbf{x} \in \Omega \tag{2.1}$$

where ∇^2 represents the Laplacian operator, $T(\mathbf{x},t)$ is the sought temperature field variable, t denotes time ($t > 0$). k is the thermal conductivity dependent on the special variables $\mathbf{x} \in \Omega$; ρ is the mass density and c is the specific heat. $Q_t = Q_m + Q_r$ stands for the general internal heat generation per unit volume due to metabolic heat and the interior heat caused by outer heating sources such as a laser beam. ρ_b, c_b and ω_b are respectively density, specific heat and perfusion rate of blood, T_b is the temperature of arterial blood, Q_m and Q_r are respectively metabolic heat generation and heat deposition in tissues caused by outer heating factors such as laser and microwave. The constant T_a is artery temperature.

The above Pennes equation (2.1) is based on the assumption that the heat exchange between blood vessels and the surrounding tissue occurs mainly across the walls of capillaries (blood vessels with diameters of the order of 0.01mm), where the blood velocity is very slow [18]. The first term on the left-hand side of Eq. (2.1) represents conduction of heat in the tissue caused by the temperature gradient [38], and the second term describes the heat transport between the tissue and microcirculatory blood perfusion [52]. The third and last terms are internal heat generation due to tissue metabolism and outer heating sources. On the right-hand side of Eq. (2.1), $\rho c \frac{\partial T}{\partial t}$ represents the changing rate of the temperature.

In the next subsection, the PDE (2.1) is derived from the fundamental principles of heat conduction to facilitate deep understanding of the origin of each term in the Pennes equation.

(1) Heat gain term caused by heat source

A typical tissue segment generates heat per unit volume at a variable rate, $Q_t(\mathbf{X}, t)$, where $\mathbf{X}$ is the spatial coordinate set. When the contributions of all tissue elements in the volume V are summed, the following expression is obtained for the rate of gain

$$U_{gain} = \int_V Q_t\left(\mathbf{X}, t\right) dV \tag{2.2}$$

(2) Thermal energy storage term

When heat production or consumption is unsteady, part of the heat flow is stored in the control volume. The stored heat is reflected in temperature changes of the various tissues. The local rate of heat change of temperature is controlled by the intrinsic heat capacity (the product of density, ρ, and specific heat capacity, c, at a constant pressure). Then, the total rate of stored thermal energy over the tissue control volume V can be given by

$$U_{storage} = \int_V \rho c \frac{\partial T\left(\mathbf{X}, t\right)}{\partial t} dV \tag{2.3}$$

(3) Heat conduction term

Heat conduction U_c is the thermal energy transferred through a medium due to an internal temperature gradient. It is governed by the well-known Fourier law of heat conduction [125]. This law states that the amount of thermal energy is directly proportional to the cross-sectional area A, which is perpendicular to the heat conduction direction, i.e. the x-direction, the temperature difference ΔT across the medium, the time length Δt of heat conduction, and simultaneously is inversely proportional to the length ΔL across which conduction occurs. Also, introducing a proportionality constant, thermal conductivity *k*, the Fourier law can be written as

$$U_c = -k\frac{A\Delta T\Delta t}{\Delta L} \tag{2.4}$$

In Eq. (2.4), the minus sign is dictated by the second law of thermodynamics which states that heat flows from regions of higher temperature to regions of lower temperature. From Eq. (2.4), we can obtain the heat flow along the heat conduction direction, which is defined as the rate of heat per unit area per unit time, that is,

$$\frac{U_c}{A\Delta t} = -k\frac{\Delta T}{\Delta L} \tag{2.5}$$

Further, the differential form of the heat flow component along the heat conduction direction can be obtained by letting $\Delta L \to 0$, i.e.,

$$q_x = \lim_{\Delta L\to 0}\frac{U_c}{A\Delta t} = \lim_{\Delta L\to 0}\left(-k\frac{\Delta T}{\Delta L}\right) = -k\frac{\mathrm{d}T}{\mathrm{d}x} \tag{2.6}$$

which can be extended to the standard Fourier's law of heat conduction in vector form

$$\mathbf{q} = \left(q_x, q_y\right) = \left(-k\frac{\mathrm{d}T}{\mathrm{d}x}, -k\frac{\mathrm{d}T}{\mathrm{d}x}\right) = -k\nabla T \tag{2.7}$$

Integrating Eq. (2.7) over an arbitrary area A, which is perpendicular to the heat conduction direction, yields the following rate of heat production through the control volume

$$U_c = -\int_A k\nabla T\left(\mathbf{X},t\right)\cdot\mathbf{n}dA \tag{2.8}$$

where $\mathbf{n}$ is the unit vector normal to the incremental surface area dA.

(4) Blood perfusion term

In perfused biological tissue, which is made up of cells, blood vessels, etc., one must consider the blood flow distribution. The perfusion distribution markedly influences the local temperature. For such cases, convection is the most important mechanism for thermal energy transfer between tissue and blood flow.

To mathematically represent the local contribution of blood perfusion to energy exchange, the most common approach is based on the application of Fick's principle: "*the amount of substance taken up by an organ (or control volume) per unit time is equal to the arterial level of the substance minus the venous level times the rate of blood flow*", that is,

$$q_b = \rho_b c_b w_b \left(T_a - T_v\right) \tag{2.9}$$

where T_a and T_v are the temperature of the blood entering the tissue from the arterioles and the temperature of the venous blood leaving the tissue, respectively. Generally, the venous temperature is a function of the temperature of the tissue at the point of exit. However, considering the very slow blood flow, a further assumption of equality in the venous blood temperature and the tissue temperature may be applied. Thus, setting $T_v = T$ in Eq. (1.7), one obtains

$$q_b = \rho_b c_b w_b \left(T_a - T\right) \tag{2.10}$$

Further, the total amount of thermal energy over the tissue control volume can be expressed in the following equation [52, 126, 127]

$$U_b = \int_V \rho_b c_b w_b \left(T_a - T\right) dV \tag{2.11}$$

which is the heat loss to adjacent tissues (convection and conduction)

Finally, applying the principle of conservation of energy to a tissue control volume, we obtain

$$U_{gain} = U_{storage} + U_{loss} \tag{2.12}$$

where the term U_{loss} denotes heat loss to adjacent tissues by convection and conduction, that is, $U_{loss} = U_c - U_b$.

For a tissue control volume, substitution of the heat gain, storage, and loss terms into Eq. (2.12) gives [90, 94]

$$\int_V Q_t\left(\mathbf{X},t\right) dV = \int_V \rho c \frac{\partial T\left(\mathbf{X},t\right)}{\partial t} dV - \int_A k \nabla T\left(\mathbf{X},t\right)\cdot \mathbf{n} dA - \int_V \rho_b c_b w_b \left(T_a - T\right) dV \tag{2.13}$$

Applying the divergence theorem to the surface integral and observing that Eq. (2.13) must hold for any arbitrary volume element, we obtain

$$k\nabla^2 T + \rho_b c_b \omega_b \left(T_a - T\right) + Q_t = \rho c \frac{\partial T}{\partial t} \tag{2.14}$$

2.2 Boundary Conditions

In this work, the following three types of boundary condition are involved [15, 27, 43, 51, 59, 84, 94, 128]

(1) Temperature condition on the boundary Γ_1 *of the tissue*

Since the boundary Γ_1 is assumed to be connected or adjacent to the body core of the tissue, the temperature on this boundary is assumed to be

$$T(\mathbf{x},t)=\bar{T}(\mathbf{x},t) \quad \mathbf{x}\in\Gamma_1 \tag{2.15}$$

where $T(\mathbf{x},t)$ is the tissue temperature on the boundary Γ_1 and $\bar{T}(\mathbf{x},t)$ is the assumed constant temperature.

(2) Heat flux condition on the boundary Γ_2 *of the tissue*

On the boundary Γ_2 the magnitude of the normal heat flow is assumed to be given. So the boundary conditions can be written as

$$q(\mathbf{x},t)=\bar{q}(\mathbf{x},t) \quad \mathbf{x}\in\Gamma_2 \tag{2.16}$$

where q represents the boundary normal heat flux defined and $\bar{q}$ is a constant normal heat flux value.

(3) Convection conditions on the boundary Γ_3

If the boundary Γ_3 is exposed to the environment, the heat loss caused through convection should be considered. For this case, the convection boundary condition is written as

$$q(\mathbf{x},t)=h_\infty\left(T-T_\infty\right) \quad \mathbf{x}\in\Gamma_3 \tag{2.17}$$

where h_∞ is the heat transfer coefficient between the tissue and ambient environment, T_∞ is the sink temperature of the environment fluid.

2.3 Elements of Fundamental Solutions

Because fundamental-solution-based methods were developed in this work for numerically solving the bioheat transfer problem, the basic concept of fundamental solutions is reviewed here.

Considering the following generic equation [59, 129, 130]

$$Lu(\mathbf{x}) = f(\mathbf{x}) \tag{2.10}$$

where $\mathbf{x} = (\mathbf{r}, t)$ are the space-time coordinates related to the spatial variable $\mathbf{r}$ and time variable t, L is a general linear differential operator and $u(\mathbf{x})$ is the sought field and $f(\mathbf{x})$ is a given function.

If the linear differential operator L is invariant with respect to the translations in space and time, a generic solution in terms of the Green's function can be given as [131]

$$u(\mathbf{x}) = \int G(\mathbf{x} - \mathbf{x}_0) f(\mathbf{x}_0) d\mathbf{x}_0 \tag{2.11}$$

with the Green's function G satisfying the equation

$$LG(\mathbf{x}, \mathbf{x}_0) = \delta(\mathbf{x}, \mathbf{x}_0) \tag{2.12}$$

where $\delta(\mathbf{x},\mathbf{x}_0)$ is the Dirac delta function centred at the field point $\mathbf{x}$ and $\mathbf{x}_0$ is the source point. Also, the function $G(\mathbf{x},\mathbf{x}_0)$ is sometimes called the fundamental solution of the operator L [26, 132].

In this work, some types of PDE such as the Laplace equation and the modified Helmholtz equation are involved. Therefore the corresponding fundamental solutions are reviewed in this section.

The first consideration is the modified Helmholtz equation. Correspondingly, the linear differential operator L is $L=\nabla^2-\lambda^2$. Typically, the two-dimensional free-space fundamental solution of the modified Helmholtz operator can be obtained as the solution of the equation [133]

$$\nabla^2 G^*\left(\mathbf{x},\mathbf{x}_0\right)-\lambda^2 G^*\left(\mathbf{x},\mathbf{x}_0\right)=\delta\left(\mathbf{x},\mathbf{x}_0\right) \tag{2.14}$$

which gives [129]

$$G^*\left(\mathbf{x},\mathbf{x}_0\right)=-\frac{1}{2\pi}K_0\left(\lambda\left\|\mathbf{x}-\mathbf{x}_0\right\|\right) \tag{2.15}$$

where K_0 denotes the modified Bessel function of the second kind with order 0.

For the Laplace operator $L=\nabla^2$, its fundamental solution is required to satisfy [132]

$$\nabla^2 G\left(\mathbf{x},\mathbf{x}_0\right)=\delta\left(\mathbf{x},\mathbf{x}_0\right) \tag{2.15}$$

which has a solution [66, 108, 119, 121]

$$G\left(\mathbf{x},\mathbf{x}_0\right)=\frac{1}{2\pi}\ln\left\|\mathbf{x}-\mathbf{x}_0\right\| \tag{2.16}$$

for the two-dimensional case.

2.4 Elements of Radial Basis Functions (RBFs)

In this work, the summation of RBFs [134, 135] is used to approximate the given function, i.e. the right-handed inhomogeneous term of the PDE. Therefore the basics of RBFs are reviewed here.

A RBF ϕ is a real-valued function whose value depends only on the distance from the origin, i.e. $\phi(r)=\phi(\|\mathbf{x}\|)$, or alternatively on the distance from a reference point $\boldsymbol{\xi}$, so that $\phi(r)=\phi(\|\mathbf{x}-\boldsymbol{\xi}\|)$. Any function ϕ that satisfies the property $\phi(r)=\phi(\|\mathbf{x}\|)$ is a radial function. The norm is usually the Euclidean distance [132]

$$r=\|\mathbf{x}-\boldsymbol{\xi}\|=\sqrt{(x_1-\xi_1)^2+(x_2-\xi_2)^2} \tag{2.17}$$

for the two-dimensional case, and

$$r=\|\mathbf{x}-\boldsymbol{\xi}\|=\sqrt{(x_1-\xi_1)^2+(x_2-\xi_2)^2+(x_3-\xi_3)^2} \tag{2.18}$$

for the three-dimensional case, although other distance functions are also possible.

Generally, there are two categories of RBF. One is the piecewise polynomial compactly supported RBF (CS-RBF) in the local domain and the other is the globally supported RBF (GS-RBF) in the entire domain [136]. The commonly used types of GS-RBF include

- Gaussian (c is a shape parameter)

$$\phi(r) = e^{-(cr)^2} \tag{2.19}$$

- Multiquadric (c is a shape parameter)

$$\phi(r) = \sqrt{1 + cr^2} \tag{2.20}$$

- Polyharmonic spline

$$\begin{aligned} \phi(r) &= r^k, & k &= 1,3,5,\cdots \\ \phi(r) &= r^k \ln(r), & k &= 2,4,6,\cdots \end{aligned} \tag{2.21}$$

- Thin plate spline (a special polyharmonic spline)

$$\phi(r) = r^2 \ln(r) \tag{2.22}$$

We know that RBFs are very suitable for building up an approximation function of a given function. For example, the right-hand inhomogeneous term $b(\mathbf{x})$ of the Helmholtz-type PDE

$$\nabla^2 u_p(\mathbf{x}) - \lambda^2 u_p(\mathbf{x}) = b(\mathbf{x}) \tag{2.23}$$

can be approximated by a serial linear combination of RBFs centred at different reference points $\mathbf{x}_j$ $(j = 1, 2, \cdots, N)$ as below [66, 132, 136, 137]

$$b(\mathbf{x}) = \sum_{j=1}^{M} \alpha_j \phi_j(\mathbf{x}) \tag{2.24}$$

where M is the number of reference points, α_j is the unknown weight coefficient, and $\phi_j(\mathbf{x}) = \phi(r_j) = \phi(\|\mathbf{x} - \mathbf{x}_j\|)$.

Correspondingly, the particular solution $u_p(\mathbf{x})$ can be determined numerically by the dual reciprocity technique and has the form of [59, 138, 139]

$$u_p(\mathbf{x}) = \sum_{j=1}^{M} \alpha_j \Phi(r_j) \tag{2.25}$$

where the kernel function of the particular solution is governed by

$$\nabla^2 \Phi(r_j) - \lambda^2 \Phi(r_j) = \phi(r_j) \tag{2.26}$$

If the thin plate spline (TPS)

$$\phi(r_j) = r_j^2 \ln(r_j) \tag{2.27}$$

is used in Eq. (2.24), the approximate particular solution $\Phi(r_j)$ can be obtained by the annihilator method as [140]

$$\Phi(r_j) = \begin{cases} -\dfrac{4}{\lambda^4} - \dfrac{4}{\lambda^4} \ln r_j - \dfrac{1}{\lambda^2} r_j^2 \ln r_j - \dfrac{4}{\lambda^4} K_0(\lambda r_j), & r_j \neq 0 \\ -\dfrac{4}{\lambda^4} + \dfrac{4\gamma}{\lambda^4} + \dfrac{4}{\lambda^4} \ln\left(\dfrac{\lambda}{2}\right), & r_j = 0 \end{cases} \tag{2.28}$$

where $\gamma = 0.5772156649015328$ is Euler's constant.

Chapter 3 Transient Linear Bioheat Transfer Analysis in Human Skin under Laser-tissue Interaction

3.1 Problem Description

The two-dimensional rectangular skin model used in [45] is taken into consideration here, in which the skin material is assumed to be homogeneous and isotropic. In the model displayed in Figure 3.1, the outer surface of the skin tissue is subjected to the convention condition and the inner boundary is assumed to be distant from the skin surface so that its temperature is the same as the constant core temperature of the body. The upper and lower surfaces are treated as adiabatic boundaries by assuming that the tissue remote from the area of interest is not affected by the imposed thermal disturbance. Moreover, a Gaussian type laser beam is introduced in Figure 3.1 as the internal spatial heating source and the Beer-Lambert law is used to model the exponential decay of heat generation by laser heating inside the tissue.

Due to the symmetry of the skin model, only half of the model is taken into consideration in the practical analysis (see the upper half shaded region displayed in Figure 3.1). Also in Figure 3.1, a Cartesian rectangular coordinate system is established and x denotes the tissue depth from the skin surface while y is the vertical distance along the skin surface. The length and width of the half rectangular solution are 4cm and 3cm, respectively [45]. The thermal properties of skin tissue used in the analysis are listed in [59].

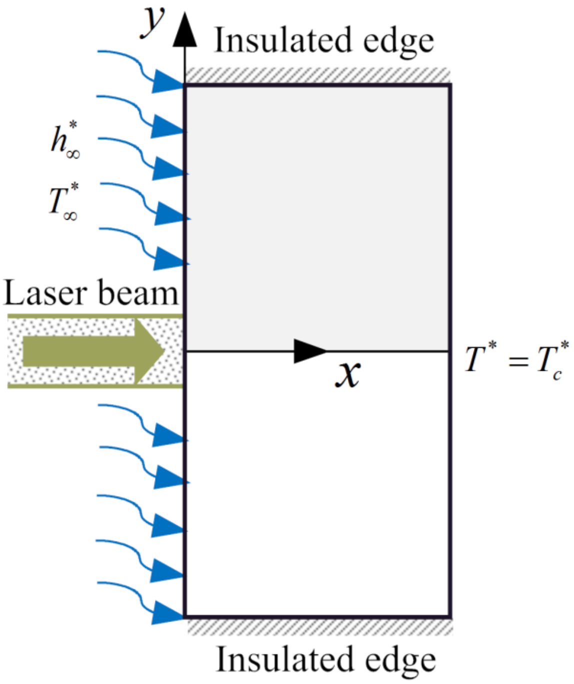

Figure 3. 1 Simplified skin model of two-dimensional skin tissue

Table 3.1 Thermal properties of skin tissue

Thermal properties of skin	*Value*
Thermal conductivity k ($Wm^{-1}K^{-1}$)	0.5
Density ρ (kgm^{-3})	1000
Specific heat c ($Jkg^{-1}K^{-1}$)	4200
Blood perfusion rate ω_b ($m^3s^{-1}m^{-3}$)	0.0005
Density of blood ρ_b (kgm^{-3})	1000
Specific heat of blood c_b ($Jkg^{-1}K^{-1}$)	4200
Metabolic heat Q_m (Wm^{-3})	4200

As shown in Figure 3.1, the laser beam, assumed to be produced from a CO_2 laser with scanner head and beam expander, injects directly onto the mid-point (0, 0) of the skin surface. In the present work, the pattern of the laser beam is that of Gaussian distribution with 2.85mm standard deviation [141]. The Beer-Lambert law is used to model the laser heat absorption in the two-dimensional skin model, and thus the spatial heat source Q_r^* caused by the laser heating is described by

$$Q_r^*(x,y,t) = P_{in}\mu_a e^{(-\mu_a x)}\frac{1}{\sigma\sqrt{2\pi}}e^{\left(\frac{-y^2}{2\sigma^2}\right)} \qquad (3.1)$$

where P_{in} represents the laser power setting, μ_a is the absorption coefficient of the skin tissue determined by the wave length of the laser, and σ is the standard deviation of the laser beam profile.

Referring to the Cartesian coordinate system shown in Figure 3.1, the bioheat transfer in the biological skin tissue of interest is adequately described by the well-known Pennes equation in the following general form [124]

$$k^*\nabla^2 T^* + \rho_b^* c_b^* \omega_b^* \left(T_a^* - T^*\right) + Q_t^* = \rho^* c^* \frac{\partial T^*}{\partial t^*} \qquad \mathbf{x}\in\Omega \tag{3.2}$$

with the boundary conditions

$$\begin{cases} T^*(\mathbf{x},t^*) = \overline{T}^*(\mathbf{x},t^*) & \mathbf{x}\in\Gamma_1 \\ q^*(\mathbf{x},t^*) = \overline{q}^*(\mathbf{x},t^*) & \mathbf{x}\in\Gamma_2 \\ q^*(\mathbf{x},t^*) = h_\infty^*(T^* - T_\infty^*) & \mathbf{x}\in\Gamma_3 \end{cases} \tag{3.3}$$

where ∇^2 represents the Laplacian operator, $T^*(\mathbf{x},t^*)$ is the sought temperature field variable, t^* denotes time ($t^* > 0$). k^* is the thermal conductivity dependent on the spatial variables $\mathbf{x}\in\Omega$, ρ^* is the mass density and c^* is the specific heat. $Q_t^* = Q_m^* + Q_r^*$ stands for the general internal heat generation per unit volume due to metabolic heat and the laser beam. q^* represents the boundary normal heat flux defined by

$$q^* = -k^*\nabla T^* \bullet \mathbf{n} = -k^* \frac{\partial T^*}{\partial n} \tag{3.4}$$

n is the unit outward normal to the boundary Γ. A variable with over-bar denotes the variable being specified on given boundary. The constant T_a^* is artery temperature. The constant h_∞^* is the convection coefficient and T_∞^* is the environmental temperature. For a well-posed problem, we have $\Gamma = \Gamma_1 \cup \Gamma_2 \cup \Gamma_3$.

Finally, the initial condition is defined as

$$T^*(\mathbf{x}, t^* = 0) = T_0^*\left(x\right) \tag{3.5}$$

To avoid the potential numerical overflow of the present algorithm, the following dimensionless variables are employed in the analysis [142]

$$\begin{aligned} &X = \frac{x}{L_0}, \quad Y = \frac{y}{L_0}, \quad T = \frac{\left(T^* - T_a^*\right)k_0}{Q_0 L_0^2}, \quad k = \frac{k^*}{k_0} \\ &\rho = \frac{\rho^*}{\rho_0}, \quad c = \frac{c^*}{c_0}, \quad t = \frac{t^* k_0}{L_0^2 \rho_0 c_0}, \quad Q_t = \frac{Q_t^*}{Q_0} \end{aligned} \tag{3.6}$$

where L_0 is the reference length of the biological body, k_0, ρ_0, c_0 and Q_0 are respectively reference values of the thermal conductivity, density, specific heat of tissue and heat source term.

From Eq. (3.6) and using the chain rule of the derivative of the composite function, we obtain

$$\begin{aligned} &\frac{\partial T^*}{\partial x} = \frac{Q_0 L_0^2}{k_0}\frac{1}{L_0}\frac{\partial T}{\partial X}, \quad \frac{\partial T^*}{\partial y} = \frac{Q_0 L_0^2}{k_0}\frac{1}{L_0}\frac{\partial T}{\partial Y} \\ &\frac{\partial^2 T^*}{\partial x^2} = \frac{Q_0 L_0^2}{k_0}\frac{1}{L_0^2}\frac{\partial^2 T}{\partial X^2}, \quad \frac{\partial^2 T^*}{\partial y^2} = \frac{Q_0 L_0^2}{k_0}\frac{1}{L_0^2}\frac{\partial^2 T}{\partial Y^2} \\ &\frac{\partial T^*}{\partial t^*} = \frac{Q_0 L_0^2}{k_0}\frac{k_0}{L_0^2 \rho_0 c_0}\frac{\partial T}{\partial t}, \end{aligned} \tag{3.7}$$

Substitution of Eq. (3.7) into the bioheat transfer governing equation (3.2) yields

$$k\nabla^2 T(\mathbf{x},t) - \rho_b c_b \omega_b T(\mathbf{x},t) + Q_t(\mathbf{x}) = \rho c \frac{\partial T(\mathbf{x},t)}{\partial t} \tag{3.8}$$

where

$$\rho_b c_b \omega_b = \frac{\rho_b^* c_b^* \omega_b^* L_0^2}{k_0} \tag{3.9}$$

Correspondingly, the boundary conditions are rewritten as

$$\begin{cases} T(\mathbf{x},t) = \overline{T}(\mathbf{x},t) & \mathbf{x} \in \Gamma_1 \\ q(\mathbf{x},t) = \overline{q}(\mathbf{x},t) & \mathbf{x} \in \Gamma_2 \\ q(\mathbf{x},t) = h_\infty (T - T_\infty) & \mathbf{x} \in \Gamma_3 \end{cases} \tag{3.10}$$

with

$$\overline{T} = \frac{\left(\overline{T}^* - T_a^*\right) k_0}{Q_0 L_0^2}, \quad \overline{q} = \frac{\overline{q}^*}{Q_0 L_0}, \quad h_\infty = \frac{h_\infty^* L_0}{k_0}, \quad T_\infty = \frac{\left(T_\infty^* - T_a^*\right) k_0}{Q_0 L_0^2} \tag{3.11}$$

and

$$q = -k \frac{\partial T}{\partial n} \tag{3.12}$$

Making use of finite difference method, the derivative of temperature can be written as [78]

$$\frac{\partial T(\mathbf{x},t)}{\partial t} = \frac{T^{n+1}(\mathbf{x}) - T^n(\mathbf{x})}{\Delta t} \tag{3.13}$$

where Δt is the time step, $T^{n+1}(\mathbf{x}) = T(\mathbf{x}, t^{n+1})$ and $T^n(\mathbf{x}) = T(\mathbf{x}, t^n)$ represent the temperature at the time instances t^{n+1} and t^n, respectively.

As a result, Eq. (3.8) at the time instance t^{n+1} can be rewritten as

$$k\nabla^2 T^{n+1}(\mathbf{x}) - \rho_b c_b \omega_b T^{n+1}(\mathbf{x}) + Q_t(\mathbf{x}) = \rho c \frac{T^{n+1}(\mathbf{x}) - T^n(\mathbf{x})}{\Delta t} \tag{3.14}$$

Rearranging Eq. (3.14) gives

$$\nabla^2 T^{n+1}(\mathbf{x}) - \lambda^2 T^{n+1}(\mathbf{x}) = b(\mathbf{x}) \tag{3.15}$$

with

$$\lambda = \sqrt{\frac{\rho c}{k\Delta t} + \frac{\rho_b c_b \omega_b}{k}} \tag{3.16}$$

and

$$b(\mathbf{x}) = -\frac{1}{k} Q_t(\mathbf{x}) - \frac{\rho c}{k\Delta t} T^n(\mathbf{x}) \tag{3.17}$$

Accordingly, the boundary conditions at time instance t^{n+1} can be represented as

$$\begin{cases} T^{n+1}(\mathbf{x}) = \overline{T}(\mathbf{x}, t^{n+1}) & \mathbf{x} \in \Gamma_1 \\ q^{n+1}(\mathbf{x}) = \overline{q}(\mathbf{x}, t^{n+1}) & \mathbf{x} \in \Gamma_2 \\ q^{n+1}(\mathbf{x}) = h_\infty (T^{n+1} - T_\infty) & \mathbf{x} \in \Gamma_3 \end{cases} \tag{3.18}$$

3.2 Algorithm Implementation

The linear system consisting of the governing PDE (3.15) and boundary conditions (3.18) is a standard inhomogeneous modified Helmholtz system, which will be solved by means of the present HFS-FEM and the dual reciprocity technique based on RBF interpolation described in this section.

3.2.1 RBF for Particular Solutions

Let T_p^{n+1} be a particular solution of the governing equation (3.15). Then we have

$$\nabla^2 T_p^{n+1}(\mathbf{x}) - \lambda^2 T_p^{n+1}(\mathbf{x}) = b(\mathbf{x}) \tag{3.19}$$

It is necessary to point out that the particular solution is not required to satisfy the boundary condition (3.18). Then, the system consisting of Eqs. (3.15) and (3.18) can be reduced to a homogeneous system by introducing two new variables as follows

$$\begin{aligned} T_h^{n+1}(\mathbf{x}) &= T^{n+1}(\mathbf{x}) - T_p^{n+1}(\mathbf{x}) \\ q_h^{n+1}(\mathbf{x}) &= q^{n+1}(\mathbf{x}) - q_p^{n+1}(\mathbf{x}) \end{aligned} \tag{3.20}$$

where

$$q_h^{n+1}(\mathbf{x}) = -k \frac{\partial T_h^{n+1}(\mathbf{x})}{\partial n}, \qquad q_p^{n+1}(\mathbf{x}) = -k \frac{\partial T_p^{n+1}(\mathbf{x})}{\partial n} \tag{3.21}$$

Substituting Eq. (3.20) into Eqs. (3.15) and (3.18), we obtain the following homogeneous equation

$$\nabla^2 T_h^{n+1}(\mathbf{x}) - \lambda^2 T_h^{n+1}(\mathbf{x}) = 0 \tag{3.22}$$

with modified boundary conditions

$$\begin{cases} T_h^{n+1}(\mathbf{x}) = \overline{T}_h(\mathbf{x}) = \overline{T}(\mathbf{x}, t^{n+1}) - T_p^{n+1}(\mathbf{x}) & \mathbf{x} \in \Gamma_1 \\ q_h^{n+1}(\mathbf{x}) = \overline{q}_h(\mathbf{x}) = \overline{q}(\mathbf{x}, t^{n+1}) - q_p^{n+1}(\mathbf{x}) & \mathbf{x} \in \Gamma_2 \\ q_h^{n+1}(\mathbf{x}) = h_\infty \left\{ T_h^{n+1}(\mathbf{x}) - T_\infty^{n+1}(\mathbf{x}) \right\} & \mathbf{x} \in \Gamma_3 \end{cases} \tag{3.23}$$

where

$$T_\infty^{n+1}(\mathbf{x}) = -T_p^{n+1}(\mathbf{x}) + T_\infty + \frac{q_p^{n+1}(\mathbf{x})}{h_\infty} \tag{3.24}$$

The above homogeneous system can be solved using the hybrid finite element model described in the next section.

In what follows, we describe the solution procedure for the particular solution part $T_p^{n+1}(\mathbf{x})$. For the arbitrary right-handed source term $b(\mathbf{x})$, the particular solution $T_p^{n+1}(\mathbf{x})$ can be determined numerically by the dual reciprocity technique, in which it is essential to approximate the source term by a series of RBFs, as described in Chapter 2.

Let ϕ be a RBF. Then the source term $b(\mathbf{x})$ in Eq. (3.19) can be approximated as follows [132, 136]

$$b(\mathbf{x}) = \sum_{j=1}^{M} \alpha_j \phi(r_j) \tag{3.25}$$

where $r_j = \left\| \mathbf{x} - \mathbf{x}_j \right\|$ denotes the Euclidean distance between the field point $\mathbf{x}$ and reference point $\mathbf{x}_j$, and α_j are unknown coefficients.

Making use of Eq. (3.24), the particular solution can be obtained as

$$T_p^{n+1}(\mathbf{x}) = \sum_{j=1}^{M} \alpha_j \Phi\left(r_j\right) \tag{3.26}$$

where the kernel function $\Phi\left(r_j\right)$ is governed by

$$\nabla^2 \Phi\left(r_j\right) - \lambda^2 \Phi\left(r_j\right) = \phi\left(r_j\right) \tag{3.27}$$

Taking the TPS

$$\phi\left(r_j\right) = r_j^2 \ln\left(r_j\right) \tag{3.28}$$

as an example, the approximate particular solution $\Phi\left(r_j\right)$ can be obtained by the annihilator method as [140]

$$\Phi(r_j) = \begin{cases} -\dfrac{4}{\lambda^4} - \dfrac{4}{\lambda^4} \ln r_j - \dfrac{1}{\lambda^2} r_j^2 \ln r_j - \dfrac{4}{\lambda^4} K_0\left(\lambda r_j\right), & r_j \neq 0 \\ -\dfrac{4}{\lambda^4} + \dfrac{4\gamma}{\lambda^4} + \dfrac{4}{\lambda^4} \ln\left(\dfrac{\lambda}{2}\right), & r_j = 0 \end{cases} \tag{3.29}$$

where $\gamma = 0.5772156649015328$ is Euler's constant.

3.2.2 Fundamental-solution-based Hybrid Finite Element for Homogeneous Solutions

To perform the hybrid finite element analysis in a convenient way, the boundary conditions given in Eq. (3.23) are rewritten as

$$\begin{cases} T_h^{n+1}(\mathbf{x}) = \overline{T}_h(\mathbf{x}) & \mathbf{x} \in \Gamma_1 \\ \chi_h^{n+1}(\mathbf{x}) = \overline{\chi}_h(\mathbf{x}) & \mathbf{x} \in \Gamma_2 \\ \chi_h^{n+1}(\mathbf{x}) = \overline{h}_\infty \left\{ T_h^{n+1}(\mathbf{x}) - T_\infty^{n+1}(\mathbf{x}) \right\} & \mathbf{x} \in \Gamma_3 \end{cases} \tag{3.30}$$

with

$$\chi_h^{n+1}(\mathbf{x}) = \frac{\partial T_h^{n+1}(\mathbf{x})}{\partial n}, \quad \bar{\chi}_h(\mathbf{x}) = -\bar{q}_h(\mathbf{x})/k, \quad \bar{h}_\infty = -\frac{h_\infty}{k} \tag{3.31}$$

Then, the following hybrid variational functional expressed at element level can be constructed as [132]

$$\Pi_{me} = \frac{1}{2}\int_{\Omega_e} \left(T_{,i}T_{,i} + \lambda^2 T^2\right) \mathrm{d}\Omega - \int_{\Gamma_{2e}} \bar{\chi}\tilde{T}\mathrm{d}\Gamma + \int_{\Gamma_e} \chi\left(\tilde{T} - T\right)\mathrm{d}\Gamma - \frac{1}{2}\int_{\Gamma_{3e}} \bar{h}_\infty \left(\tilde{T} - T_\infty\right)^2 \mathrm{d}\Gamma \tag{3.32}$$

in which T is the temperature field defined inside the element domain Ω_e with the boundary Γ_e, $\tilde{T}$ denotes the frame field defined along the element boundary, and $\Gamma_{2e} = \Gamma_2 \cap \Gamma_e$, $\Gamma_{3e} = \Gamma_3 \cap \Gamma_e$. Note that in equation (3.32), the superscript ‘*n*+1’ and the subscript ‘*h*’ are discarded for the sake of simplicity.

By invoking the divergence theorem and assuming that $\tilde{T}$ satisfies the specified temperature boundary condition (the first equation of (3.30)) and the compatibility condition on the interface between the element under consideration and its adjacent elements as prerequisites, equation (3.32) can be written as

$$\begin{aligned}\delta\Pi_{me} = &-\int_{\Omega_e} \left(T_{,ii} - \lambda^2 T\right)\delta T \mathrm{d}\Omega + \int_{\Gamma_{2e}} \left(\chi - \bar{\chi}\right)\delta\tilde{T}\mathrm{d}\Gamma + \int_{\Gamma_e} \delta\chi\left(\tilde{T} - T\right)\mathrm{d}\Gamma \\ &+ \int_{\Gamma_{3e}} \left[\chi - \bar{h}_\infty\left(\tilde{T} - T_\infty\right)\right]\delta\tilde{T}\mathrm{d}\Gamma\end{aligned} \tag{3.33}$$

from which it can be seen that the third integral enforces the equality of T and $\tilde{T}$ along the element boundary Γ_e. The first, second and fourth integrals enforce respectively the governing equation, flux and convection boundary conditions.

If the internal temperature field T satisfies the homogeneous modified Helmholtz equation, i.e.

$$\nabla^2 T - \lambda^2 T = 0 \tag{3.34}$$

then applying the divergence theorem again to the functional (3.32), we have

$$\Pi_{me} = -\frac{1}{2}\int_{\Gamma_e} \chi T \mathrm{d}\Gamma - \int_{\Gamma_{2e}} \overline{\chi} \tilde{T} \mathrm{d}\Gamma + \int_{\Gamma_e} \chi \tilde{T} \mathrm{d}\Gamma - \int_{\Gamma_{3e}} \frac{\overline{h}_\infty}{2}\left(\tilde{T} - T_\infty\right)^2 \mathrm{d}\Gamma \tag{3.35}$$

which involves boundary integrals only.

In the proposed HFS-FEM, the variable T is given as a superposition of fundamental solutions $G^*(P,Q_j)$ at n_s source points to guarantee satisfaction of equation (3.34)

$$T_h^{n+1}(P) = \sum_{j=1}^{N_s} G^*(P,Q_j) c_{ej} = \mathbf{N}_e(P)\mathbf{c}_e, \quad P \in \Omega_e, Q_j \notin \Omega_e \tag{3.36}$$

where c_{ej} is undetermined coefficients and N_s is the number of virtual sources Q_j applied at points outside the element.

The free-space fundamental solution of the modified Helmholtz operator can be obtained as the solution of

$$\nabla^2 G^*(P,Q_j) - \lambda^2 G^*(P,Q_j) = -\delta(P,Q_j) \tag{3.37}$$

and is given by [132]

$$G^*(P,Q_j) = -\frac{1}{2\pi} K_0(\lambda \left\| P - Q_j \right\|) \tag{3.38}$$

where $\delta(P,Q_j)$ is the Dirac delta function and K_0 denotes the modified Bessel function of the second kind with order 0.

Simultaneously, the independent frame variable on the element boundary can be defined by the standard shape function interpolation

$$\tilde{T}(P)=\sum_{i=1}^{n}\tilde{N}_i(P)d_{ei}=\tilde{\mathbf{N}}_e(P)\mathbf{d}_e,\quad P\in\Gamma_e \tag{3.39}$$

where n is the number of nodes of the element under consideration, $\tilde{N}_i$ is the shape function and d_{ei} is the nodal temperature. Their descriptions can be found in standard finite element texts and are not repeated here.

By substituting equations (3.36) and (3.39) into equation (3.35) we obtain

$$\Pi_{me}=-\frac{1}{2}\mathbf{c}_e^{\mathrm{T}}\mathbf{H}_e\mathbf{c}_e-\mathbf{d}_e^{\mathrm{T}}\mathbf{g}_e+\mathbf{c}_e^{\mathrm{T}}\mathbf{G}_e\mathbf{d}_e-\frac{1}{2}\mathbf{d}_e^{\mathrm{T}}\mathbf{F}_e\mathbf{d}_e+\mathbf{d}_e^{\mathrm{T}}\mathbf{f}_e-\mathbf{a}_e \tag{3.40}$$

in which

$$\begin{aligned}&\mathbf{H}_e=\int_{\Gamma_e}\mathbf{Q}_e^{\mathrm{T}}\mathbf{N}_e\mathrm{d}\Gamma,\quad \mathbf{G}_e=\int_{\Gamma_e}\mathbf{Q}_e^{\mathrm{T}}\tilde{\mathbf{N}}_e\mathrm{d}\Gamma,\quad \mathbf{g}_e=\int_{\Gamma_{2e}}\tilde{\mathbf{N}}_e^{\mathrm{T}}\bar{\chi}\mathrm{d}\Gamma\\&\mathbf{F}_e=\int_{\Gamma_{3e}}\bar{h}_\infty\tilde{\mathbf{N}}_e^{\mathrm{T}}\tilde{\mathbf{N}}_e\mathrm{d}\Gamma,\quad \mathbf{f}_e=\int_{\Gamma_{3e}}\bar{h}_\infty T_\infty\tilde{\mathbf{N}}_e^{\mathrm{T}}\mathrm{d}\Gamma,\quad \mathbf{a}_e=\int_{\Gamma_{3e}}\frac{\bar{h}_\infty T_\infty^2}{2}\mathrm{d}\Gamma\end{aligned} \tag{3.41}$$

and

$$\mathbf{Q}_e=\frac{\partial\mathbf{N}_e}{\partial n} \tag{3.42}$$

3.3 Results and Discussion

In this section, the proposed numerical model is applied to several examples for validating and assessing its applicability and effectiveness. Values of the parameters employed in the following analysis are listed in Table 3.2 for convenience [143, 144].

Table 3.2 Control parameters related to boundary conditions

Control parameters	*Value*
Ambient temperature T_∞ (ºC)	0~30
Ambient convection coefficient h_∞ ($\mathrm{Wm^{-2}K^{-1}}$)	40~12500
Heat conductivity of tissue k ($\mathrm{Wm^{-1}K^{-1}}$)	0.2~0.9
Laser power setting P_{in} (W)	100~250
Absorption coefficient μ_a ($\mathrm{m^{-1}}$)	5~20

To validate and assess the performance of the present HFS-FEM for analysing the transient heat transfer of skin materials with blood perfusion and metabolic heat, a benchmark example is considered whose steady-state analytical solution is expressed as [43]

$$T^*(x) = A + \frac{\left(T_c^* - A\right)\left[\mu\cosh\left(\mu x\right) + B\sinh\left(\mu x\right)\right]}{\mu\cosh\left(\mu L\right) + B\sinh\left(\mu L\right)} + \frac{B\left(T_\infty^* - A\right)\sinh\left[\mu\left(L - x\right)\right]}{\mu\cosh\left(\mu L\right) + B\sinh\left(\mu L\right)} \quad (3.43)$$

where

$$\begin{aligned} A &= T_a^* + \frac{Q_m^*}{\rho_b^* \omega_b^* c_b^*} \\ B &= \frac{h_\infty^*}{k^*} \\ \mu &= \sqrt{\frac{\rho_b^* \omega_b^* c_b^*}{k^*}} \end{aligned} \quad (3.44)$$

and L is the thickness of the skin tissue.

In the computation, the solution domain is modelled with 20 eight-node quadratic elements including 99 nodes. Three different time steps, Δt =50s, 80s and 100s, are employed to assess the performance of the time-stepping scheme employed in this work. It is assumed that a relatively steady state is reached when the inter-iteration difference between adjacent time instances is less than or equal to 10^{-3}. After 120, 82 and 68 iterations respectively, the corresponding distributions of temperature to these three time steps along x axis are plotted. The results from the analytical solution equation (3.43) are also plotted for the purpose of comparison. As is evident in Figure 3.2, the numerical results from the proposed HFS-FEM are in good agreement with the analytical solutions. At the origin point of the coordinate system, the percentage relative errors of surface temperature are respectively 0.022%, 0.45% and 0.56% for the three time steps used during the computation. The maximum value of the percentage relative errors is 1.44%, which occurs at the region close to the skin surface. Here it is necessary to point out that a smaller time step does not produce better results. It can be explained that in $\lambda = \sqrt{\frac{\rho_b c_b \omega_b}{k} + \frac{\rho c}{k\Delta t}}$, the second term representing the blood perfusion effect $\frac{\rho_b c_b \omega_b}{k}$ is much smaller than the first term associated with time discretization $\frac{\rho c}{k\Delta t}$, that is

$$\frac{\rho c}{k\Delta t} \gg \frac{\rho_b c_b \omega_b}{k} \tag{3.45}$$

if the time step becomes smaller. This will cause a round-off error during computation.

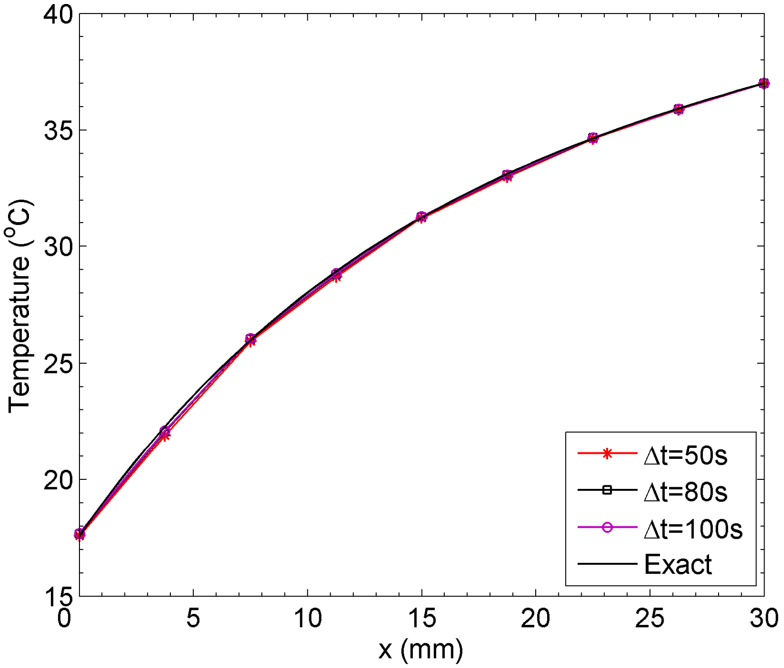

Figure 3.2 Steady-state temperature distribution along *x* axis

In Figure 3.3 the temperature distribution of skin tissues at 500s, 1000s, 3000s and steady state is displayed, showing that, with the increase of time, the temperature curves do not become steeper but finally tend to a steady state. The surface temperature of the skin decreases gradually. This procedure clearly displays the propagation of the thermal wave inside the tissue and the heat exchange between the skin and the ambient fluid. Therefore, accurate results can be obtained for the transient thermal simulation in skin tissue using the present algorithm.

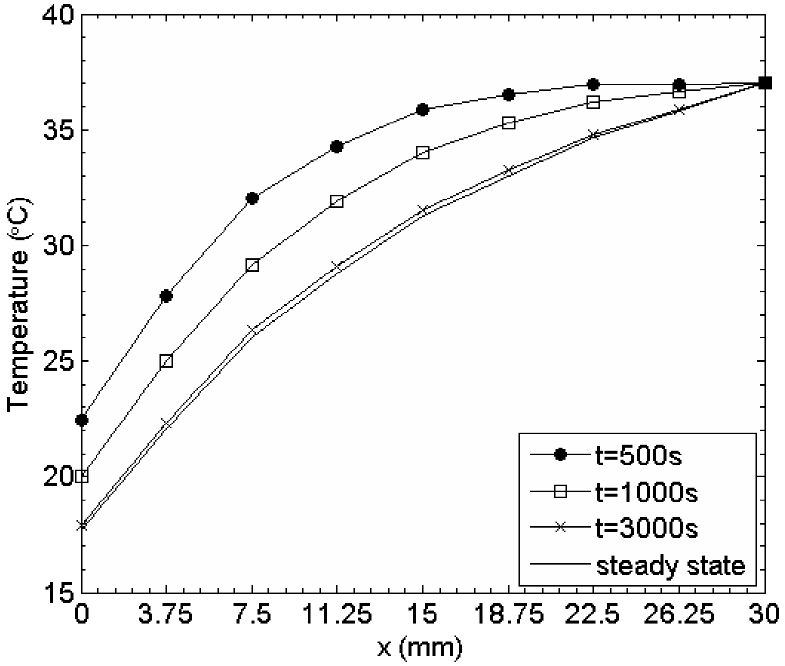

Figure 3.3 Temperature variation vs time along *x* axis

The effect of environmental fluids on skin temperature is evaluated by changing the ambient convection coefficient and ambient temperature. In this study, the ambient convection coefficient is assumed to be 40, 2500 and 12500Wm^{-2}K^{-1}, to represent different fluids such as air, oil and water [143], and the ambient temperature is set to be within the interval [0ºC, 30ºC]. The transient temperature variations are presented in Figure 3.4 and Figure 3.5 respectively. In Figure 3.4, the ambient temperature T_∞ is specified at 0ºC while the ambient convection coefficient changes from 40 to 12500Wm^{-2}K^{-1}. Figure 3.4 shows that there is very little difference between the numerical results for h_∞=12500Wm^{-2}K^{-1} and h_∞=2500Wm^{-2}K^{-1}, whereas the difference between h_∞=40Wm^{-2}K^{-1} and h_∞=2500Wm^{-2}K^{-1} is significant. The main reason for this significant difference is that the effect of forced convection increases as the convection coefficient increases. The larger convection coefficient permits more heat flow from tissue to environment. As a result, the temperature at the convection surface is significantly reduced. Hence it is necessary to increase the convection coefficient to prevent thermal damage during treatment. When the convection coefficient reaches its critical value, however, further increases in its value do not continuously increase the heat flow from tissue to environment. In Figure 3.5, the ambient convection coefficient h_∞ is set to be 40Wm^{-2}K^{-1}, which corresponds to a general forced convection, while the ambient temperature changes. As expected, there is a significant increase in temperature at the origin of the coordinate system (0, 0) when the ambient temperature increases from 0ºC to 30ºC. This is because heat energy transfers rapidly from skin tissue to the environmental fluid by convection when there is a large temperature difference between the fluid and the tissue.

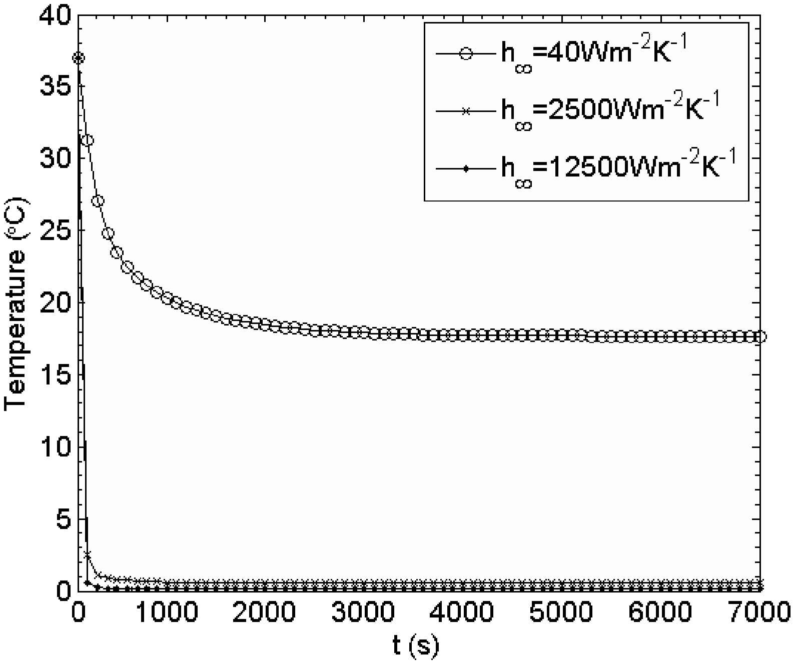

Figure 3.4 Surface temperature variation for various ambient convection coefficients

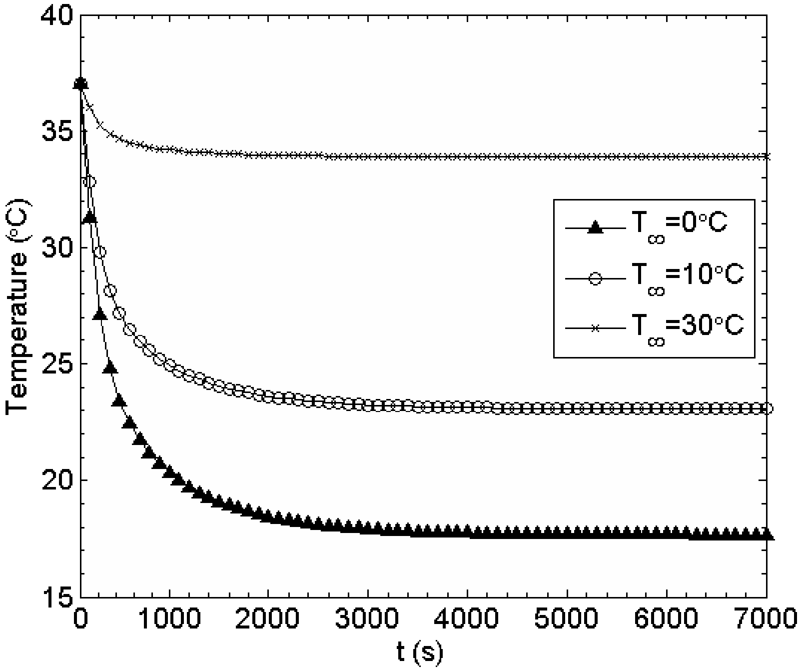

Figure 3.5 Surface temperature variation for various ambient temperatures

To study the effect of tissue thermal conductivity on skin temperature, the thermal conductivity of the tissue is assumed to vary from 0.2Wm^{-1}K^{-1} to 0.9Wm^{-1}K^{-1} in this example. In the calculation, the ambient temperature and convection coefficient are assumed to be 0°C and 40Wm^{-2}K^{-1} respectively. The variation of temperature is plotted along the *x* axis in Figure 3.6. As expected, the tissue temperature increases with the increase of thermal conductivity. This is reasonable, because higher values of thermal conductivity mean more heat transfer from high-temperature regions like the body core and arteries to the low-temperature region (the skin surface), causing the increase in surface temperature.

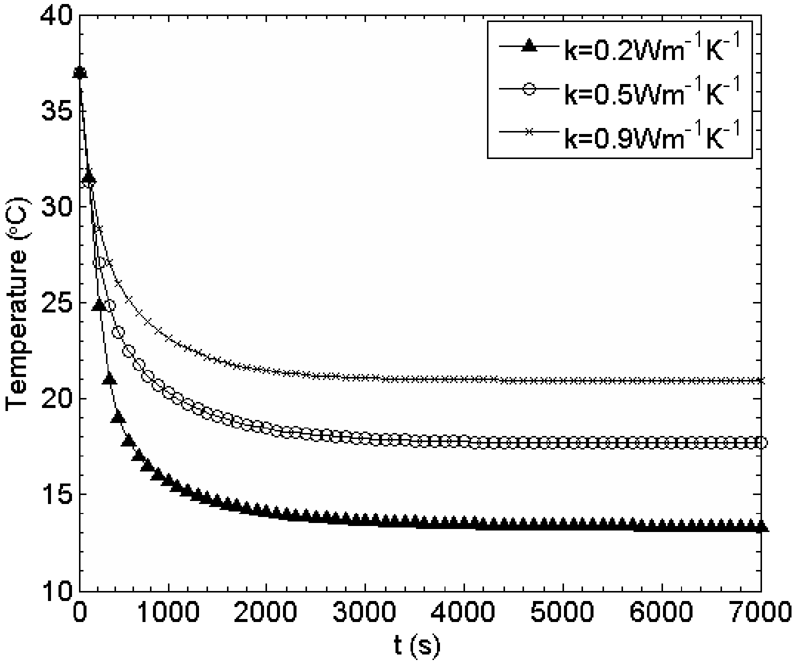

Figure 3.6 Surface temperature variation for various heat conductivities

In the fourth example, the effect of laser heating on skin temperature is studied. In practice, there are many different types of laser for various applications. In the present work, the Beer-Lambert law is used for modelling heat absorption in two-dimensional skin tissue. The induced spatial heat source Q_r caused by the laser beam is described by Eq. (3.1). In accordance with reference [141, 144], the parameters of the laser beam are taken as P_{in}=100~250W, μ_a=20m^{-1} and σ=2.85mm, respectively. The ambient temperature, ambient convection coefficient and tissue heat conductivity are respectively assumed to be 25ºC, 2500Wm^{-2}K^{-1} and 0.5Wm^{-1}K^{-1}. Figure 3.7 presents the variation of temperature at the origin (0, 0) with power settings 100W, 150W, 200W and 250W. It is clearly seen from Figure

3.7 that the temperature increases significantly as the laser power increases, because the higher laser power generates more internal heat energy inside the tissue. In addition, it is also evident from Figure 3.7 that temperature increases by about 5.4°C at each sampling point along with an increment of laser power by 50W. Figure 3.8 displays the steady-state temperature distribution along the *x* axis at 4100s and it is observed that the peak value of the temperature occurs in the region close to the body core. For comparison, the temperature distribution in the absence of laser beam is also plotted in Figure 3.8. Finally, the spatial temperature variations in the entire tissue domain are shown in Figure 3.9 and Figure 3.10 respectively for the cases with and without laser heating. It can be clearly seen that the effect of the laser beam prevents the temperature from being distributed one-dimensionally, and in the local region close to the centre of the laser beam at several penetration depths there is greater temperature gradation. Moreover, the heating effect of the laser in the thickness direction of the tissue is more obvious than that in the vertical direction.

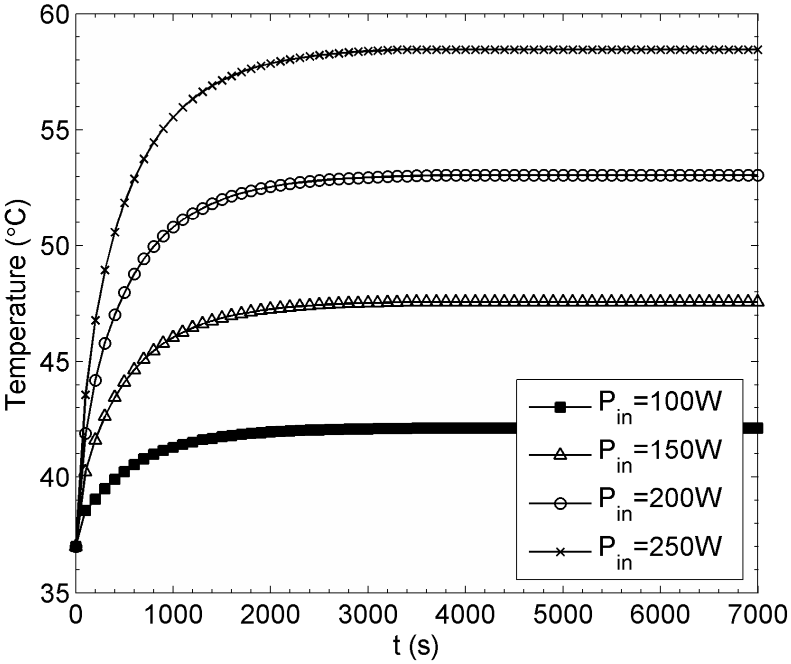

Figure 3.7 Temperature variation at origin for various laser power settings

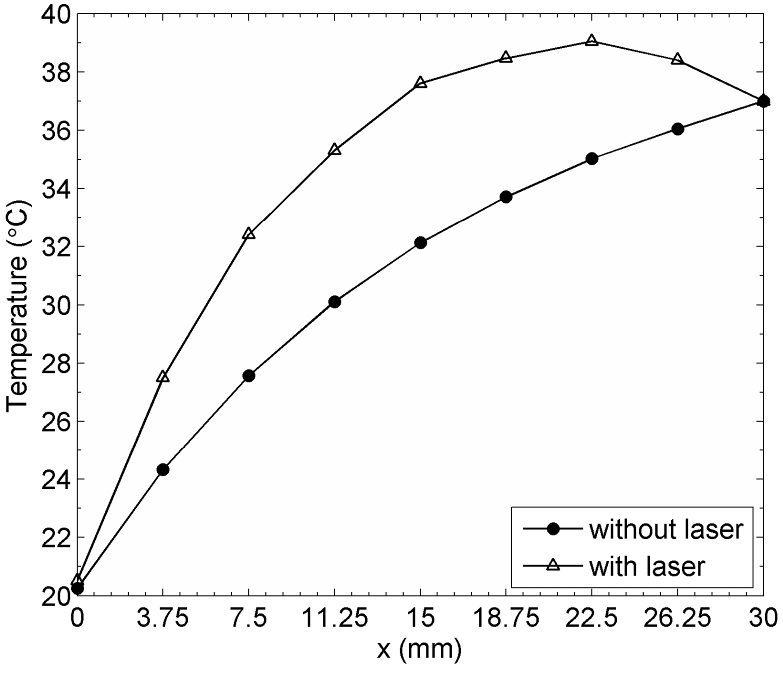

Figure 3.8 Steady temperature variation along *x* axis for laser

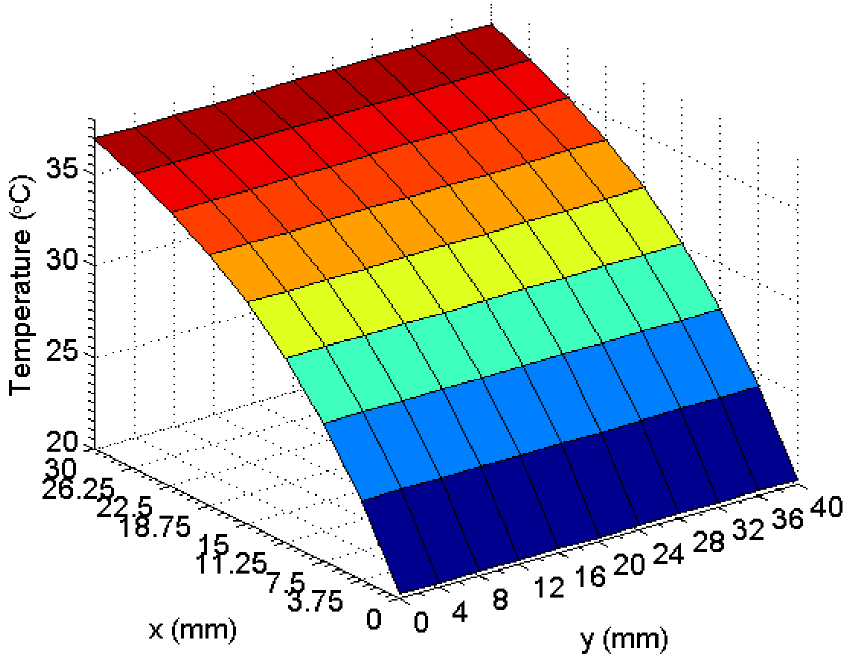

Figure 3.9 Steady-state temperature distribution without laser

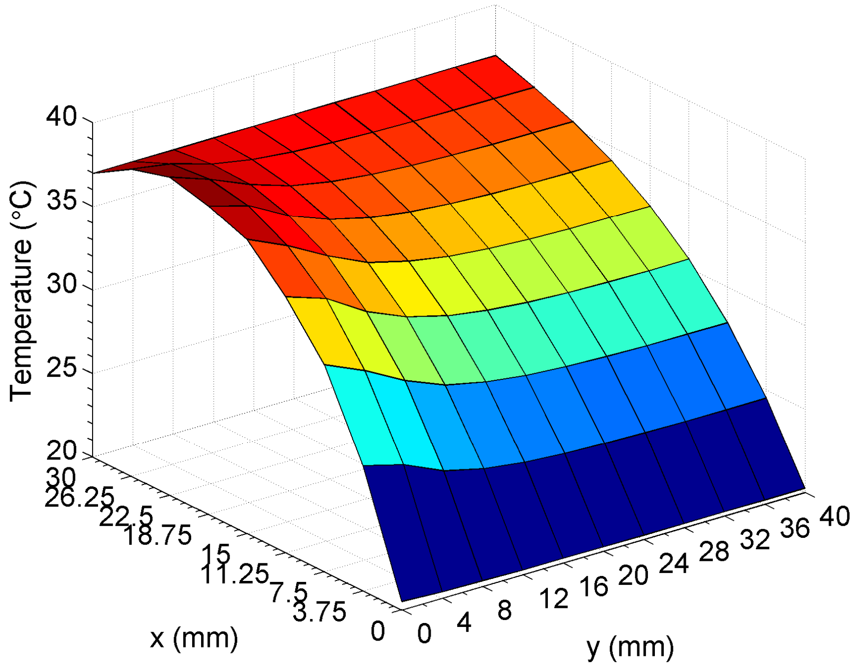

Figure 3.10 Steady-state temperature distribution with laser

As evident from Figure 3.7, the temperature of skin tissue increases rapidly along with an increase in laser power. Consequently, thermal injury or damage to biological tissue may occur as a result of laser heating [145]. The burn degree of biological tissue is usually estimated by means of the tissue damage rate Ω(t) expressed in the form [143, 146]

$$\Omega(t) = \int_0^t P \exp\left(\frac{-\Delta E}{R(T+273)}\right) d\tau \tag{3.46}$$

where P is a constant determined by the tissue properties and local temperature. ΔE represents the activation energy and R is the universal gas constant. T is the local tissue temperature at time t.

Figure 3.11 and Figure 3.12 present the numerical results for skin tissue damage rate at the point (3.75mm, 0mm) of laser heating with power settings at 250W and 150W respectively. According to references [143, 146], the threshold values of first, second and third degree burns are $\Omega=0.53$, $\Omega=1$ and $\Omega=10^4$ respectively. Figure 3.11 shows that at about 2900s the burn degree of skin tissue increases from second degree to third degree. That means that the damage to skin tissue induced by laser heating at 250W power setting exacerbates as time progresses. First and second degree burns occur very quickly at the beginning of laser heating. Therefore, a 250W laser can cause skin damage easily and quickly. As evident in Figure 3.12, under 150W laser irradiation, first degree burning occurs at about 1800s and second degree burning occurs at about 2400s. It would be expected that users avoid burning of skin tissue by reducing the laser power setting or the laser irradiation time flexibly in different applications.

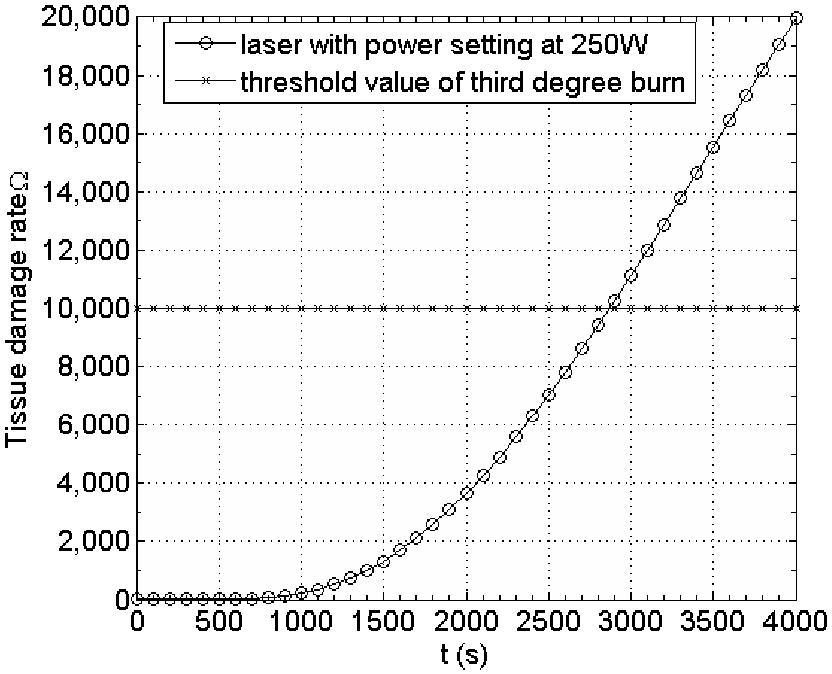

Figure 3.11 Skin tissue damage rate of laser with power setting at 250W

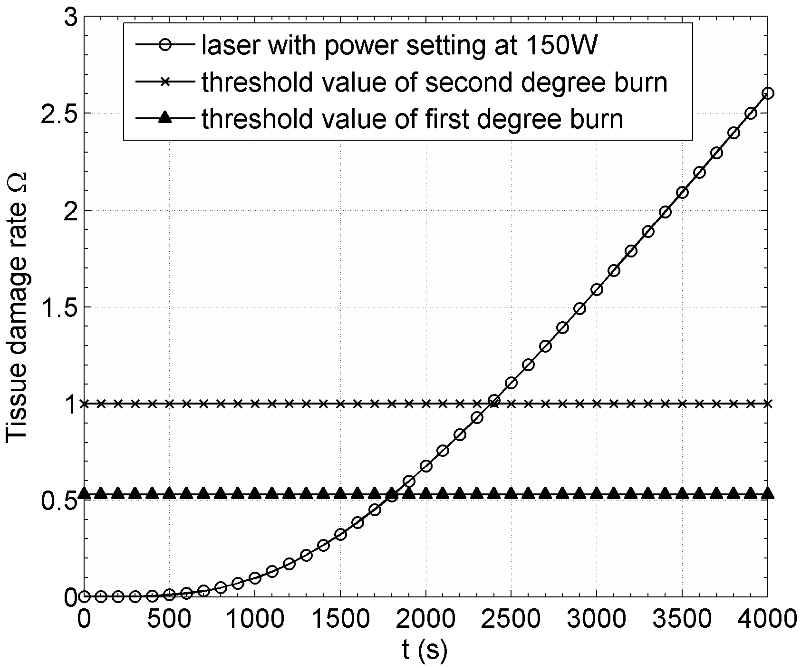

Figure 3.12 Skin tissue damage rate of laser with power setting at 150W

3.4 Summary

In this chapter, a transient HFS-FEM algorithm is developed to analyse bioheat transfer in two-dimensional skin tissue under laser irradiation. The effects of blood perfusion, metabolic heat and spatial heating induced by a Gaussian type laser beam are considered by way of the Pennes bioheat governing equation. Numerical results from the HFS-FEM coupled with RBF are first validated by comparing with the analytical solutions, and good agreement is observed. Then, sensitivity analyses are conducted by tuning the control parameters ambient convection coefficient, ambient temperature, tissue heat conductivity and laser power setting. Finally, the burn degree of skin tissue is estimated under laser radiation with different powers.

Chapter 4 Steady-State Nonlinear Bioheat Analysis with Temperature-Dependent Blood Perfusion Rate

4.1 Problem Description

We know that the governing equation for two-dimensional steady-state bioheat transfer in a homogeneous biological tissue can be expressed as [27]

$$k\nabla^2 T + \rho_b c_b \omega_b \left(T_b - T\right) + Q_r + Q_m = 0 \tag{4.1}$$

which can be obtained by discarding the right-hand term representing the changing rate of temperature in Eq. (2.1).

In Eq. (4.1), the second term on the left side describes the heat transport between the tissue and microcirculatory blood perfusion, and the blood perfusion rate is denoted as ω_b. Practically, in the physiology of biological tissue containing blood vessels, the blood vessels expand with an increase in temperature to allow greater blood flow to dissipate the heat accumulated in the body [12, 51, 85]. Therefore, the blood perfusion rate varies practically with varying tissue temperature T. In such cases, the blood perfusion rate ω_b is a function with respect to the tissue temperature T. As a result, the governing equation (4.1) can be rewritten as follows

$$k\nabla^2 T + \rho_b c_b \omega_b(T)\left(T_b - T\right) + Q_r + Q_m = 0 \tag{4.2}$$

In hyperthermia treatment, blood perfusion is usually assumed to vary in the following form

- Linear form in terms of T [51, 147, 148]

$$\omega_b\left(T\right) = a_1 + a_2 T \tag{4.3}$$

- Exponential form in terms of T [35, 48, 52, 148]

$$\omega_b\left(T\right) = a_1 e^{a_2 T} \tag{4.4}$$

- Quadratic form in terms of T

$$\omega_b\left(T\right) = a_1 + a_2 T + a_3 T^2 \tag{4.5}$$

where a_1, a_2 and a_3 are positive constants.

For convenience, we introduce a new temperature variable θ as

$$\theta = T - T_b \tag{4.6}$$

Then, the governing equation (4.2) can be rewritten in terms of the new variable as

$$k\nabla^2\theta - \rho_b c_b \omega_b(\theta + T_b)\theta + Q_r + Q_m = 0 \tag{4.7}$$

To deal with the nonlinearity caused by the TDBPR, the following linearized strategy is introduced using the first order Taylor-series expansion, i.e.

$$\rho_b c_b \omega_b (\theta + T_b)\theta = \theta f_1(\theta^n) + f_2(\theta^n) \tag{4.8}$$

where θ^n is the solution at the n^{th} iteration and

$$\begin{aligned} f_1(\theta^n) &= \rho_b c_b \left(\theta \frac{\partial \omega_b}{\partial \theta} + \omega_b \right)\bigg|_{\theta=\theta^n} \\ f_2(\theta^n) &= \rho_b c_b \omega_b (\theta^n + T_b)\theta^n - f_1(\theta^n)\theta^n \end{aligned} \tag{4.9}$$

Making use of the three types of blood perfusion rate defined by Eqs. (4.3)-(4.5), the term f_1 can be written as

$$f_1(\theta^n) = \begin{cases} \rho_b c_b \left(a_2 \theta^n + \omega_b \right) & \text{linear case} \\ \rho_b c_b \left[a_1 a_2 e^{a_2(\theta^n + T_b)} \theta^n + \omega_b \right] & \text{exponential case} \\ \rho_b c_b \left[2a_3 \left(\theta^n\right)^2 + \left(a_2 + 2a_3 T_b\right)\theta^n + \omega_b \right] & \text{quadratic case} \end{cases} \tag{4.10}$$

Substituting Eq. (4.8) into Eq. (4.7), we have

$$k\nabla^2\theta - f_1(\theta^n)\theta - f_2(\theta^n) + Q_r + Q_m = 0 \tag{4.11}$$

or

$$\nabla^2\theta - \frac{f_1(\theta^n)}{k}\theta = \frac{f_2(\theta^n) - Q_r - Q_m}{k} \tag{4.12}$$

Eqs. (4.11) and (4.12) are nonhomogeneous potential equations and the coefficient $f_1\left(\theta^n\right)$ changes with spatial position, because the iteration temperature θ is generally a function of spatial coordinates.

To solve the governing equation (4.11) or (4.12) at each iteration, the corresponding boundary conditions must be provided. Consider the two-dimensional homogeneous skin model shown in Figure 4.1.

(1) Specified temperature condition

In Figure 4.1, the boundary Γ_1 represents the right-most surface of the skin, so the temperature on Γ_1 can be approximately assumed to be the body core temperature θ_c [45], that is

$$\theta = \theta_c \quad \text{at boundary } \Gamma_1 \tag{4.13}$$

Moreover, at the left surface of the tissue, the temperature is assumed to be constant and approximately equal to the temperature of the contact heating body, i.e. the heating disc [34, 149], that is

$$\theta = \theta_s \quad \text{at boundary } \Gamma_4 \tag{4.14}$$

(2) Adiabatic condition

At the upper and bottom surfaces, no heat flow occurs along these two edges, assuming that tissue distant from the area of interest is not affected by the imposed thermal disturbance [34, 150]. Therefore, the thermally insulated conditions at these two surfaces are given by

$$-k\frac{\partial T}{\partial n} = 0 \quad \text{at boundaries } \Gamma_2 \text{ and } \Gamma_3 \tag{4.15}$$

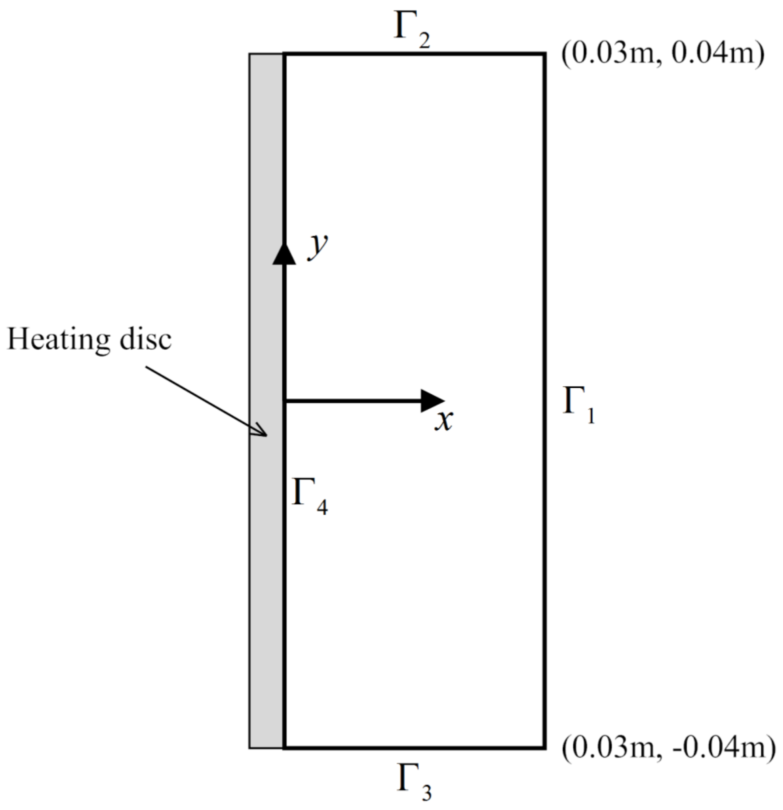

Figure 4.1 Two-dimensional skin model with heating disc

4.2 Algorithm Implementation

To solve the system consisting of the PDE (4.11) or (4.12) with a variable coefficient at each iteration and the boundary conditions (4.13)-(4.15), a mixed meshless strategy, referred to as the DRM-MFS, coupling of the MFS and the RBF approximation is established as described in this section.

4.2.1 The Analog Equation Method (AEM)

Due to nonhomogeneity of the PDE (4.11) or (4.12) caused by the variable coefficient f_1, no explicit fundamental solutions or particular solutions are available. This absence can be overcome, however, by the indirect AEM [15].

According to the basic theory of the AEM [15], if the temperature θ is twice-differentiable with respect to spatial variable $\mathbf{x}$, we can apply the Laplace operator to the sought solution θ leading to the following equivalent system [61, 65]

$$\nabla^2\theta(\mathbf{x}) = b(\mathbf{x}) \tag{4.16}$$

in which the right-hand term b is referred to as a fictitious source and is not an explicit expression due to the unknown temperature field θ. Eq. (4.16), which is referred to as an analog equation, indicates that the solution of the original equation (4.11) can be established by solving this Poisson's equation under the boundary conditions (4.13)-(4.15), if the fictitious source b is known.

Due to the linearity of the Laplace operator, the solution to equation (4.16) can be divided into two parts

$$\theta(\mathbf{x}) = \theta_h(\mathbf{x}) + \theta_p(\mathbf{x}) \tag{4.17}$$

where $\theta_h(\mathbf{x})$ is the homogeneous solution satisfying

$$\nabla^2\theta_h(\mathbf{x}) = 0 \tag{4.18}$$

and $\theta_p(\mathbf{x})$ stands for the particular solution satisfying [136]

$$\nabla^2 \theta_p(\mathbf{x}) = b(\mathbf{x}) \tag{4.19}$$

Equations (4.18) and (4.19) respectively represent the Laplace equation and Poisson's equation. Their solutions can be obtained separately using the DRM and the MFS.

4.2.2 RBF for Particular Solutions

In the dual reciprocity technique, it is essential to approximate the fictitious source term $b(\mathbf{x})$ by a series of RBFs [132, 139]. Let ϕ be a RBF, then the fictitious source term *b* in equation (4.19) can be approximated as [151]

$$b(\mathbf{x}) = \sum_{i=1}^{M} \alpha_i \phi_i(r) \tag{4.20}$$

where $r = \|\mathbf{x} - \mathbf{x}_i\|$ and $\{\mathbf{x}_i\}_1^M$ is a set of points for interpolation in the domain of interest.

Then, the particular solution of Eq. (4.19) can be obtained in the following way [152]

$$\theta_p(\mathbf{x}) = \sum_{i=1}^{M} \alpha_i \Phi_i(r) \tag{4.21}$$

where

$$\nabla^2 \Phi_i(r) = \phi_i(r) \tag{4.22}$$

If we employ the following TPS as the interpolating basis to approximate the fictitious source term *b* in Eq. (4.20) [132]

$$\phi_i(r) = r^{2n} \ln r \qquad n = 1, 2, 3, ... \tag{4.23}$$

then the particular solution $\Phi_i(r)$ can be obtained directly as [132]

$$\Phi_i(r) = \frac{(n+1)\ln r - 1}{4(n+1)^3} r^{2+2n} \qquad n = 1, 2, 3, ... \tag{4.24}$$

4.2.3 MFS for Homogeneous Solutions

In the proposed MFS, *N* virtual source points $\mathbf{s}_j$ $(j = 1, 2, \cdots, N)$ are placed on a pseudo boundary, which is geometrically similar to the physical boundary and is outside the domain [60, 66, 153]. Then, the homogeneous solution of Eq. (4.18) can be approximated by the linear combination of the fundamental solutions at different source points, that is,

$$\theta_h(\mathbf{x}) = \sum_{j=1}^{N} \beta_j G_j(\mathbf{x}), \quad \mathbf{x} \neq \mathbf{s}_j \tag{4.25}$$

where $\mathbf{x}(x, y)$ is a field point within the domain of interest or on its boundary, $\mathbf{s}_j(x_s^j, y_s^j)$ are the fictitious source points outside the domain and $G_j(\mathbf{x}) = G(\mathbf{x}, \mathbf{s}_j)$ is the fundamental solution for the Laplacian operator, which satisfies [132]

$$\nabla^2 G(\mathbf{x}, \mathbf{s}_j) + \delta(\mathbf{x}, \mathbf{s}_j) = 0 \tag{4.26}$$

and has the form

$$G_j(\mathbf{x}) = -\frac{1}{2\pi}\ln\sqrt{\left(x-x_s^j\right)^2+\left(y-y_s^j\right)^2} \tag{4.27}$$

Obviously, the approximation (4.25) exactly satisfies the Laplace governing equation (4.18).

4.2.4 Complete Solutions

Based on the process above, the final complete solution can be expressed as

$$\theta(\mathbf{x}) = \sum_{i=1}^{M}\alpha_i\Phi_i(\mathbf{x}) + \sum_{j=1}^{N}\beta_j G_j(\mathbf{x}) \tag{4.28}$$

Correspondingly, the derivative of the temperature field (4.28) gives

$$q(\mathbf{x}) = -\sum_{i=1}^{M}\alpha_i\frac{\partial\Phi_i(\mathbf{x})}{\partial n} - \sum_{j=1}^{N}\beta_j\frac{\partial G_j(\mathbf{x})}{\partial n} \tag{4.29}$$

For the sake of the subsequent derivation, Eqs. (4.28) and (4.29) are rewritten in matrix form, i.e.

$$\theta(\mathbf{x}) = \mathbf{U}(\mathbf{x})\mathbf{c} \tag{4.30}$$

$$q(\mathbf{x}) = \mathbf{Q}(\mathbf{x})\mathbf{c} \tag{4.31}$$

where

$$\mathbf{U}(\mathbf{x}) = \left[\Phi_1(\mathbf{x}) \quad \cdots \quad \Phi_M(\mathbf{x}) \quad G_1(\mathbf{x}) \quad \cdots \quad G_N(\mathbf{x})\right] \tag{4.32}$$

$$\mathbf{Q}(\mathbf{x}) = \left[-\frac{\partial\Phi_1(\mathbf{x})}{\partial n} \quad \cdots \quad -\frac{\partial\Phi_M(\mathbf{x})}{\partial n} \quad -\frac{\partial G_1(\mathbf{x})}{\partial n} \quad \cdots \quad -\frac{\partial G_N(\mathbf{x})}{\partial n}\right] \tag{4.33}$$

$$\mathbf{c}^{\mathrm{T}} = \left[\alpha_1 \quad \cdots \quad \alpha_M \quad \beta_1 \quad \cdots \quad \beta_N\right] \tag{4.34}$$

These $N+M$ unknowns can be uniquely determined by imposing the temperature θ to satisfy the governing equation at M internal points and the boundary conditions at N boundary points. In the practical computation, as can be seen from Figure 4.1, the complete boundary Γ of the two-dimensional skin domain is composed of four boundaries, Γ_1, Γ_2, Γ_3 and Γ_4. A set of points $\{P_i\}_{i=1}^{N}$ are selected on the boundary Γ. There are N_1, N_2, N_3 and N_4 points uniformly distributed on boundaries Γ_1, Γ_2, Γ_3 and Γ_4, respectively. Therefore, $N = N_1 + N_2 + N_3 + N_4$. Similarly, a set of fictitious source points $\{\mathbf{s}_i\}_{i=1}^{N}$ outside the solution domain are placed on the pseudo boundary Γ_{ps}. Correspondingly, N_1, N_2, N_3 and N_4 fictitious source points are uniformly distributed on the pseudo boundary segments parallel to Γ_1, Γ_2, Γ_3 and Γ_4 [130]. Finally, the resulting equation system can then be written as

$$\begin{cases} \left[\mathbf{B}(\mathbf{x}_i) - A(\mathbf{x}_i)\mathbf{U}(\mathbf{x}_i)\right]\mathbf{c} = F(\mathbf{x}_i), & i = 1\cdots M \\ \mathbf{U}(\mathbf{x}_j)\mathbf{c} = \theta_c, & j = 1\cdots N_1 \\ \mathbf{Q}(\mathbf{x}_k)\mathbf{c} = 0, & k = 1\cdots N_2 \\ \mathbf{Q}(\mathbf{x}_l)\mathbf{c} = 0, & l = 1\cdots N_3 \\ \mathbf{U}(\mathbf{x}_m)\mathbf{c} = \theta_s, & m = 1\cdots N_4 \end{cases} \tag{4.35}$$

in which

$$\begin{aligned} A(\mathbf{x}_i) &= \left.\frac{f_1(\theta^n)}{k}\right|_{\mathbf{x}_i} \\ F(\mathbf{x}_i) &= \left.\frac{f_2(\theta^n) - Q_r - Q_m}{k}\right|_{\mathbf{x}_i} \end{aligned} \tag{4.36}$$

and

$$\begin{aligned}\mathbf{B}(\mathbf{x}_i)=\nabla^2\mathbf{U}(\mathbf{x}_i)&=\left[\nabla^2\Phi_1(\mathbf{x}_i)\quad\cdots\quad\nabla^2\Phi_M(\mathbf{x}_i)\quad\nabla^2G_1(\mathbf{x}_i)\quad\cdots\quad\nabla^2G_N(\mathbf{x}_i)\right]\\&=\left[\phi_1(\mathbf{x}_i)\quad\cdots\quad\phi_M(\mathbf{x}_i)\quad 0\quad\cdots\quad 0\right]\end{aligned}\tag{4.37}$$

Solving the linear equation system yields the unknown coefficient vector **c** and then the temperature field can be determined using equation (4.30).

4.3 Results and Discussion

In all the calculations below, due to the symmetry of the bioheat model in the rectangular domain, only half of the domain is chosen as the solution domain. In total, 63 interpolation points inside the rectangular domain are used for modelling the particular solutions, while 32 boundary nodes along each of the four physical boundaries Γ_1, Γ_2, Γ_3 and Γ_4 ($N_2=N_3=7$ and $N_1=N_4=9$) and the same number of source points along the pseudo boundary are, respectively, used to determine the homogeneous solutions.

To investigate the convergence of the present algorithm with respect to the interpolation points, the results obtained using 486 interpolation points are compared with those using 63 points. The collocation scheme with 486 random interpolation points is displayed in Figure 4.2.

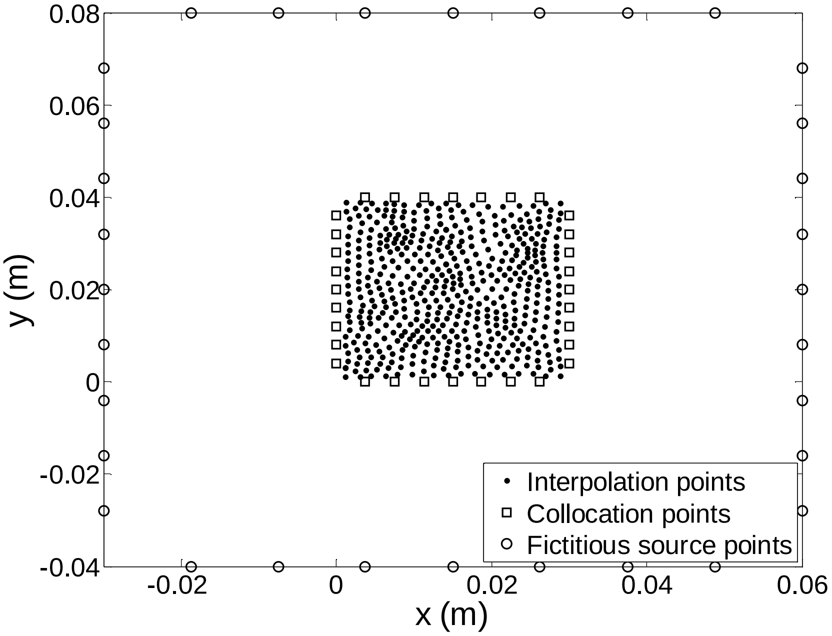

Figure 4.2 Collocation scheme with 486 random interpolation points

The thermal parameters used in the calculation are listed in Table 4.1 [59, 149]

Table 4.1 Thermal parameters of the skin tissue

Thermal properties of skin	*Value*
Thermal conductivity k (Wm^{-1}K^{-1})	0.5
Density of blood ρ_b (kgm^{-3})	1000
Specific heat of blood c_b (Jkg^{-1}K^{-1})	4200
Spatial heat Q_r (Wm^{-3})	30000
Metabolic heat Q_m (Wm^{-3})	4200
Temperature of body core T_c (ºC)	37
Temperature of skin surface T_s (ºC)	25

4.3.1 Validation of the Proposed Method

To validate the efficiency and accuracy of the proposed mixed meshless method DRM-MFS for analysing the steady-state nonlinear bioheat transfer in the two-dimensional skin tissue displayed in Figure 4.1 with the specified metabolic heat (see Table 4.1) and the TDBPR, MATLAB Partial Differential Equation (PDE) Toolbox is employed to simulate bioheat transfer in the same 2D skin tissue model. The results from DRM-MFS and PDE Toolbox are compared for the three cases of TDBPR. In the procedure with MATLAB PDE Toolbox, the finite element scheme is employed to produce the corresponding results, and the rectangular solution domain is discretized with 1044 triangular elements and 560 nodes to produce convergent results which can be viewed as a reference for comparison.

Consider first the linear case $\omega_b(T) = a_1 + a_2 T$ with $a_1 = 0.0005$ and $a_2 = 0.0001$. Figure 4.3 displays the temperature variation along the *x* axis. From Figure 4.3, the results from the proposed DRM-MFS algorithm (with 63 interpolation points inside the rectangular domain) show negligible difference from the finite element results obtained using MATLAB PDE Toolbox, and the results from the proposed DRM-MFS algorithm converge to those from the MATLAB PDE Toolbox when the interpolation points within the rectangular domain increase to 486. The relative errors of the temperature results from the DRM-MFS algorithm with respect to the results from the MATLAB PDE Toolbox are listed in Figure 4.4. Figure 4.4 shows that the maximum relative error for the DRM-MFS with 63 interpolation points is roughly 0.34%. In contrast, the maximum relative error for the DRM-MFS with 486 interpolation points is about 0.06%.

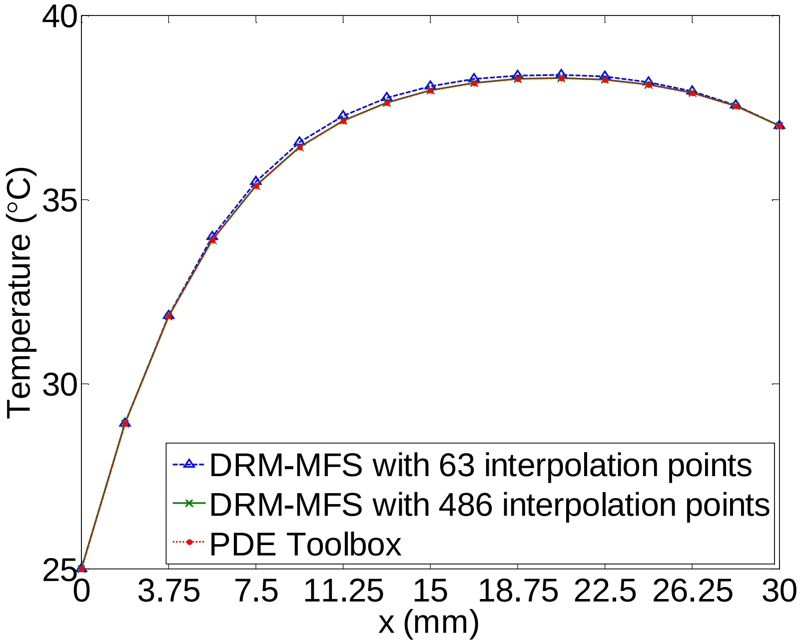

Figure 4. 3 Temperature distribution along *x* axis for the linear case of blood perfusion rate

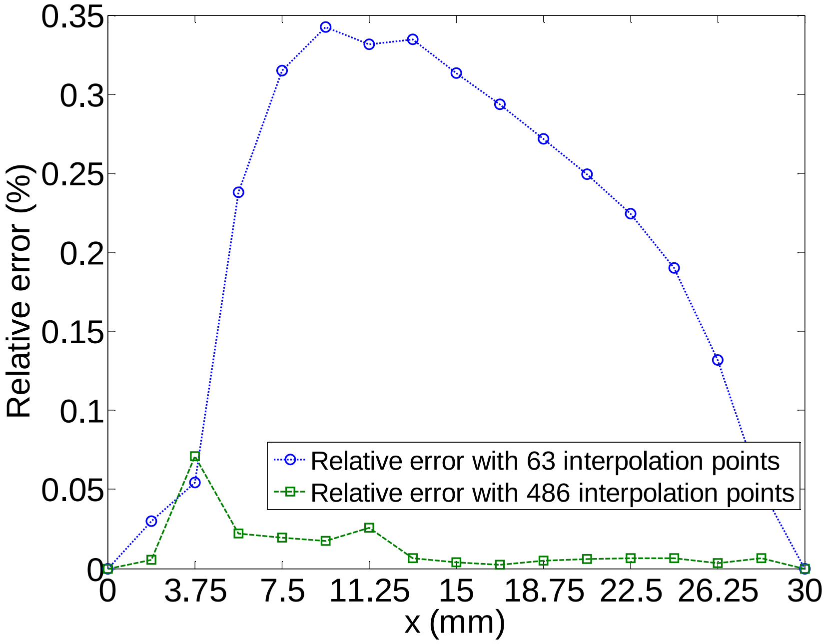

Figure 4.4 Relative error of temperature along *x* axis for the linear case of blood perfusion rate

Secondly, for the quadratic case of blood perfusion rate $\omega_b(T) = a_1 + a_2 T + a_3 T^2$, the positive constants $a_1 = 0.0005$, $a_2 = 0.0002$, and $a_3 = 0.000001$ are adopted for computation [35, 48]. Numerical results of the temperature distribution along the *x* axis from the present DRM-MFS with 63 and 486 interpolation points are presented in Figure 4.5 and the corresponding relative error is shown in Figure 4.6. From these two figures it is evident that the greater the number of interpolation points, the more accurate are the numerical results. Thus the convergence and accuracy of the present meshless method for the case of the quadratic form of the blood perfusion rate is verified.

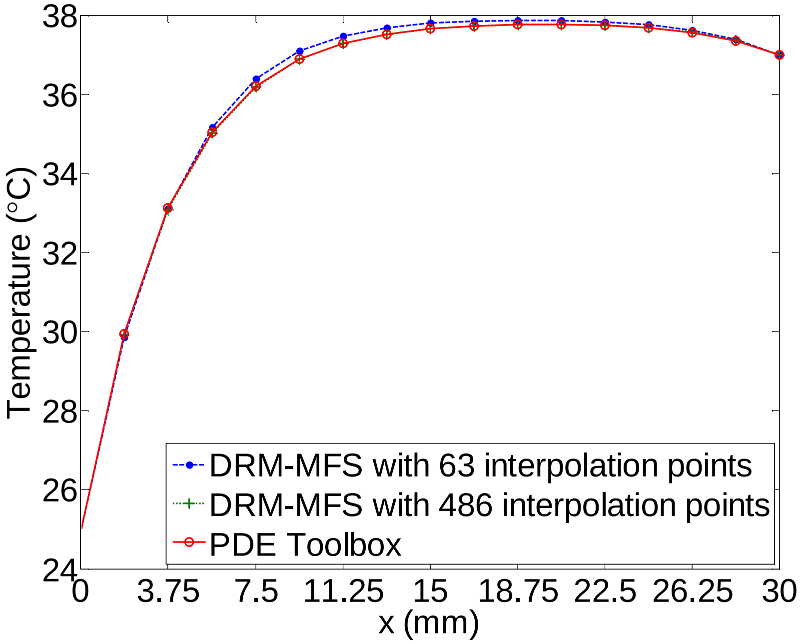

Figure 4.5 Temperature distribution along *x* axis for the quadratic case of blood perfusion rate

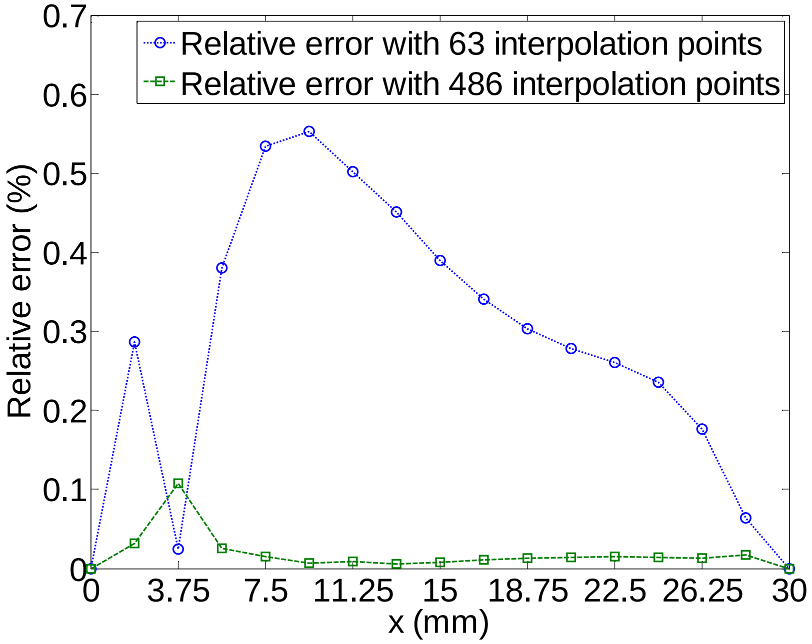

Figure 4.6 Relative error of temperature along *x* axis for the quadratic case of blood perfusion rate

Thirdly, consider the exponential case of blood perfusion rate $\omega_b(T)=a_1e^{a_2T}$ with $a_1=0.0005$ and $a_2=0.01$. Figure 4.7 and Figure 4.8 respectively plot the temperature variation along the *x* axis and the corresponding relative error. It can be seen from Figure 4.7 and Figure 4.8 that the DRM-MFS with 63 and 486 interpolation points within the solution domain have almost the same numerical results, although the results from DRM-MFS with 486 interpolation points are still more accurate than those from DRM-MFS with 63 internal points.

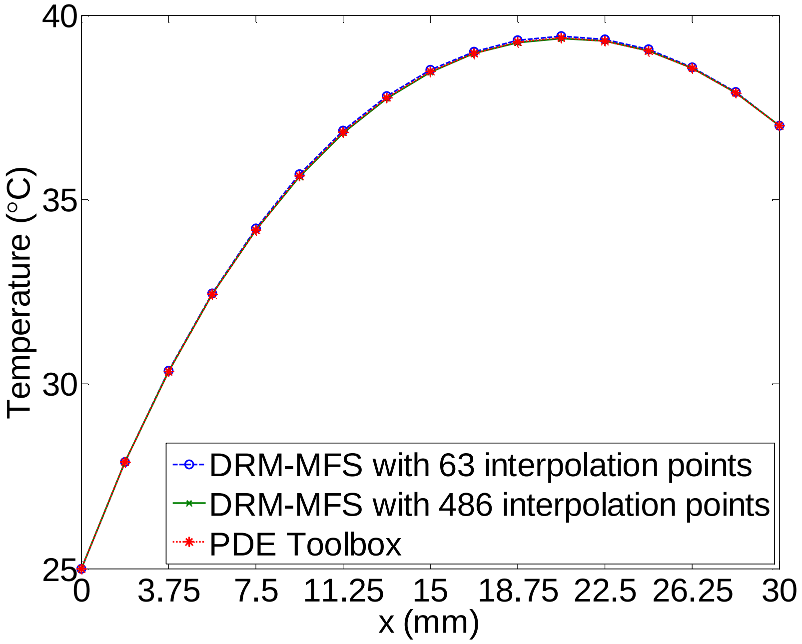

Figure 4. 7 Temperature distribution along *x* axis for the exponential case of blood perfusion rate

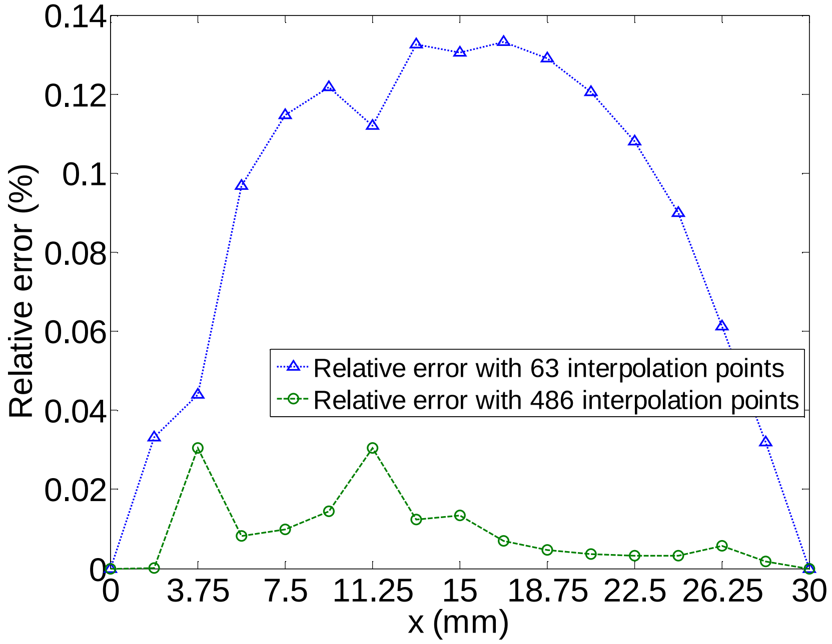

Figure 4.8 Relative error of temperature along *x* axis for the exponential case of blood perfusion rate

Finally, to investigate the effect of blood perfusion rate on temperature distribution, numerical results for problems with different blood perfusion rates are displayed in Figure 4.9, where the rates are viewed as a function of the temperature variable, including the linear, quadratic and exponential relations. In computation, 486 interpolation points are employed for RBF interpolation. It can be seen from Figure 4.9 that there is a relatively larger temperature gradient in the region near the skin surface for all three blood perfusion rate forms, due to the significant temperature difference between the skin surface and the body core or artery blood. The three temperature curves have an intersect point located at about *x*=12.18mm.

In the region $x < 12.18\text{mm}$, the quadratic form produces the highest tissue temperature and the exponential form produces the lowest tissue temperature, while in the region $x > 12.18\text{mm}$, the temperature distribution changes inversely. The highest temperature is found to exceed 39°C, due to the nonlinearity of the bioheat transfer equation.

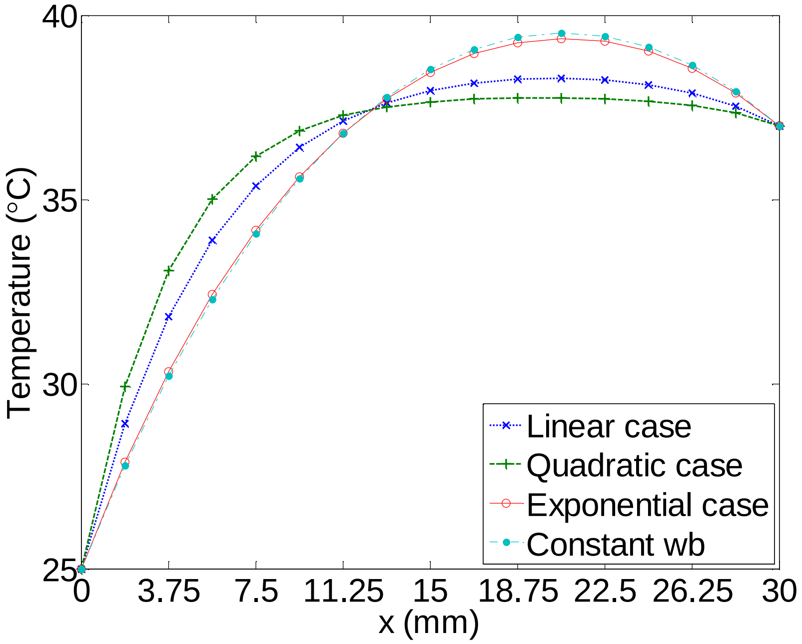

Figure 4.9 Temperature distribution along *x* axis for three cases of blood perfusion rate with 486 interpolation points

Further, to investigate the influence of TPS type of RBFs on temperature distribution, results for the order *n*=1 and *n*=2 are presented in Figure 4.10, with 63 interpolation points within the domain. In Figure 4.10, only the quadratic case of

TDBPR is taken into consideration. One can observe that the curve of the skin tissue temperature obtained by the proposed DRM-MFS with order n=2 matches much better with those from the MATLAB PDE Toolbox simulation results than the DRM-MFS with order n=1. Figure 4.11 shows the relative error of the proposed DRM-MFS with different orders of TPS basis function. The maximum error for n=1 is 0.56%, which is slightly higher than that for n=2 (0.17%). This result indicates that increasing the order of the TPS basis function can improve the accuracy of the DRM-MFS, without increasing the number of interpolation points within the domain.

From the foregoing analysis, it is concluded that numerical experiments using the DRM-MFS can converge to the reference value by increasing the number of internal interpolation points or increasing the order of the TPS basis function. The DRM-MFS seems to be a promising and simple method for solving nonlinear steady state bioheat transfer problems. In the next subsection, sensitivity analysis of parameters in the blood perfusion rate expression is conducted using the proposed meshless method.

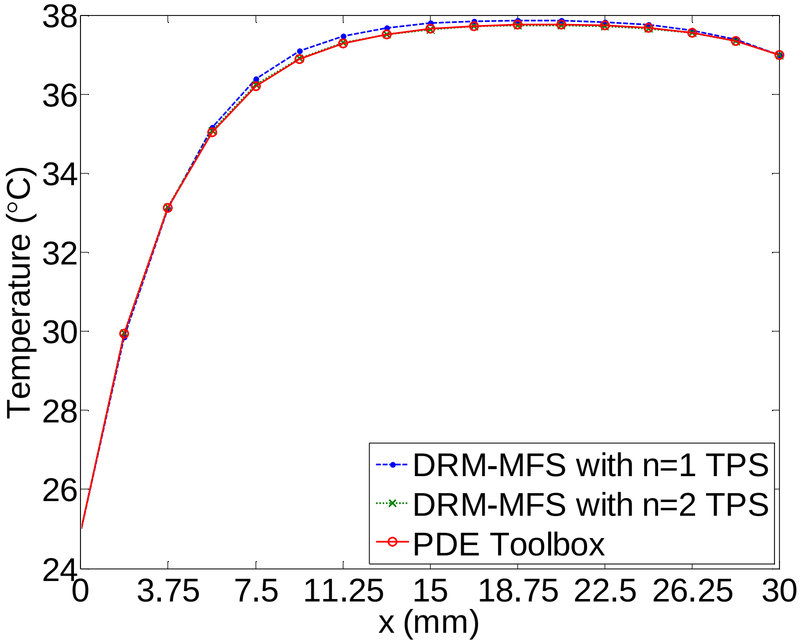

Figure 4.10 Temperature distributions along *x* axis for the quadratic case of blood perfusion rate with different TPS orders

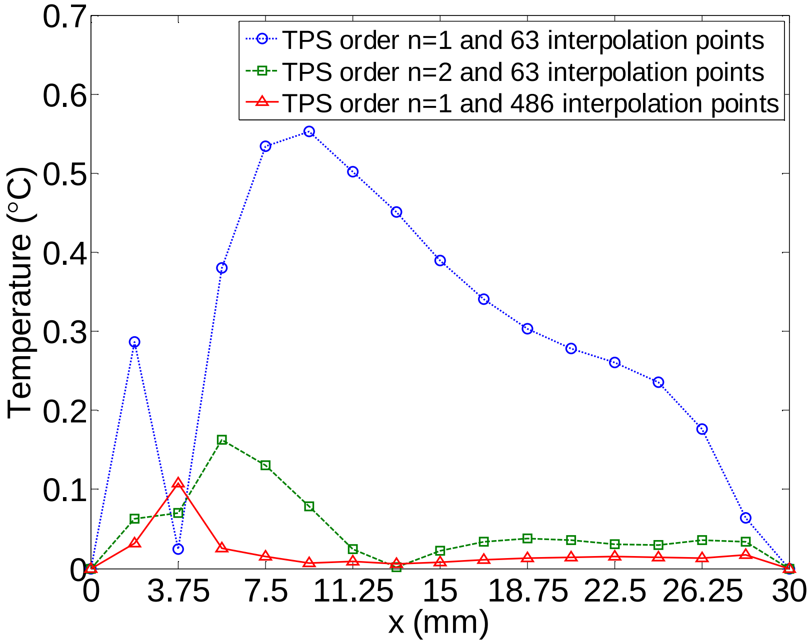

Figure 4.11 Relative error of temperature along *x* axis for the quadratic case of blood perfusion rate with different TPS orders

4.3.2 Sensitivity Analysis

In this subsection, the quadratic case of TDBPR $\omega_b(T) = a_1 + a_2 T + a_3 T^2$ is considered to investigate the sensitivity of tissue temperature to the variation of constants a_i. In the sensitivity analysis, 486 interpolation points and the first order TPS basis function are employed.

First of all, the constant term a_1 is assumed to be 0.00005, 0.0005 and 0.005 when the first order term constant a_2 and quadratic term constant a_3 are set to be 0.0002 and 0.000001. It is noted from Figure 4.12 that, when the constant a_1 is changed from 0.0005 to 0.00005, the variation of the skin tissue temperature curve is negligible. However, when the constant a_2 is changed from 0.0005 to 0.005, the variation of the skin tissue temperature curve is relatively large. The location at about (12.2mm, 0) is the crossing point of three curves with different constant a_1. That means that from location (1.875mm, 0) to (12.2mm, 0), the skin tissue temperature increases with an increase in the constant a_1. But between location (12.2mm, 0) and (28.125mm, 0), the skin tissue temperature decreases along with an increase in the constant a_1. The main reason is that before location (12.2mm, 0), the skin tissue temperature is lower than the blood temperature. Therefore, the heat flow is transferred from blood to skin tissue. A higher blood perfusion rate means that more heat flows from blood to skin tissue. In contrast, roughly after the location (12.2mm, 0) the skin tissue temperature is higher than the blood temperature. Thus the heat flow is transferred from skin tissue to blood. Therefore, a higher blood perfusion rate allows more heat flow to be lost from skin tissue to blood.

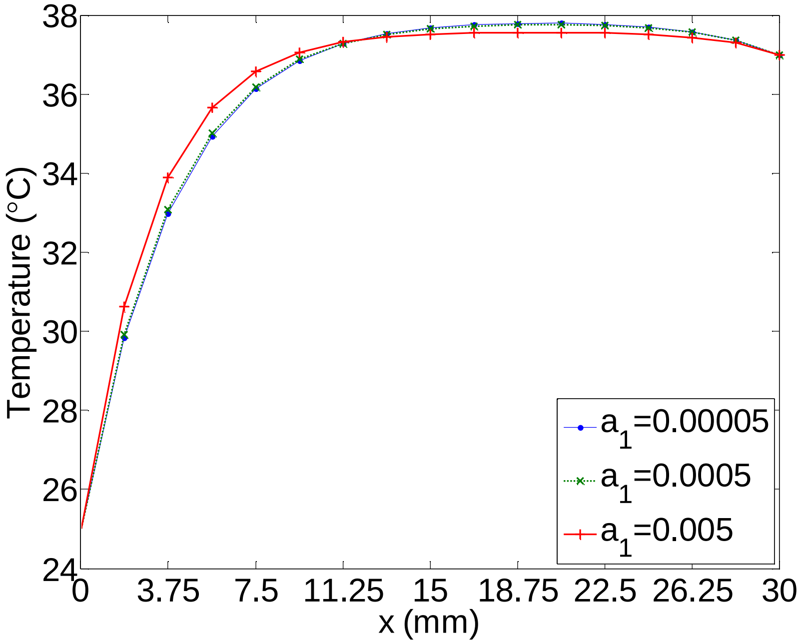

Figure 4.12 Sensitivity to constant a_1 in the quadratic case of blood perfusion rate

Next, the constant a_1 is set to be 0.0005 and the quadratic term a_3 is set to be 0.000001 while the first order term coefficient a_2 is changed from 0.00002 to 0.002. Compared with the situation in Figure 4.12, the variation of skin tissue temperature curve caused by change offing the first order coefficient a_2 is relatively greater than when changing constant a_1 (Figure 4.13). From Figure 4.13, it can also be found that increasing the first order coefficient a_2 makes the skin tissue temperature increase quickly to reach blood temperature and remain around $37^\circ C$, which is equal to the blood temperature. Thus a strong heat flow protection or regulation effect of blood to the skin tissue is shown in Figure 4.13, especially when the first order term coefficient a_2 is equal to 0.002.

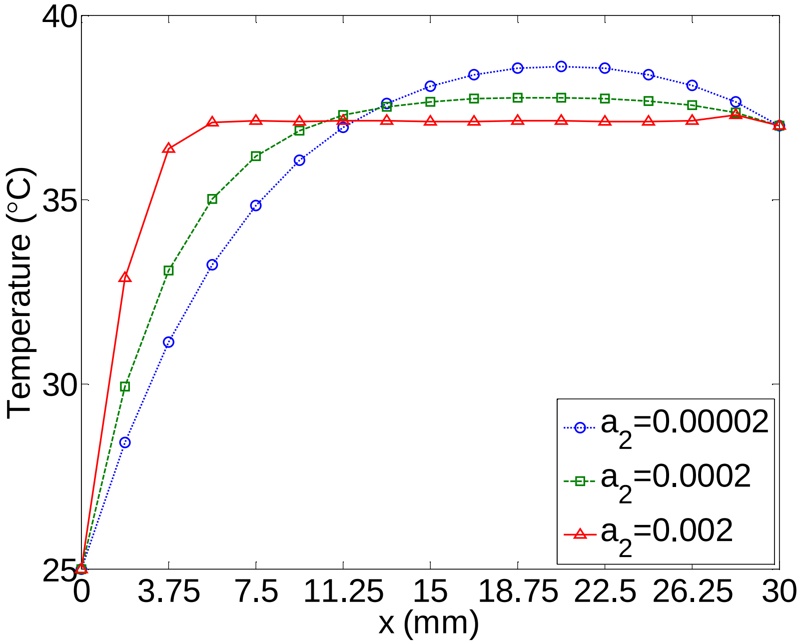

Figure 4.13 Sensitivity to constant a_2 in the quadratic case of blood perfusion rate

As evident from Figure 4.14, if the constants a_1 and a_2 are kept constant at 0.0005 and 0.0002, variation of a_3 makes the crossing point move to the location roughly at (11.25mm, 0). From the skin surface boundary to location (11.25mm, 0), a larger quadratic term coefficient a_3 produces a higher skin tissue temperature. In contrast, from the crossing point location (11.25mm, 0) to the body core boundary, a lower skin tissue temperature is induced by the larger quadratic term coefficient

a_3. It is clear that when the quadratic term coefficient of the temperature-dependent blood perfusion a_3 is equal to 0.00001, the skin tissue temperature maintains stability from location (11.25mm, 0) to (26.25mm, 0) at $37^{\circ}\mathrm{C}$, which is the same as the blood temperature.

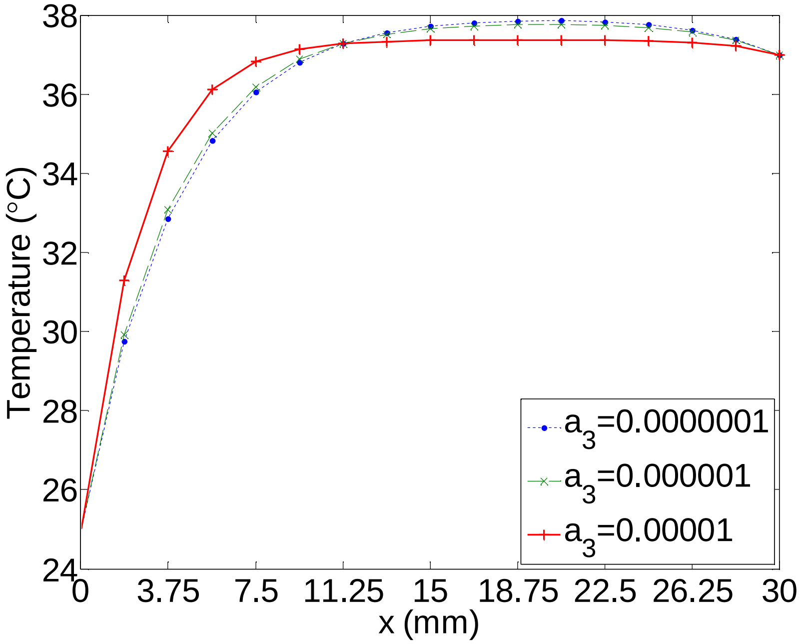

Figure 4.14 Sensitivity to constant a_3 in the quadratic case of blood perfusion rate

4.4 Summary

In this chapter, a meshless DRM-MFS algorithm is developed for analysing the nonlinear bioheat transfer in a 2D skin model. The nonlinearity is due to the temperature dependence of the blood perfusion rate. The Taylor expansion technology is first employed to linearize the nonlinear bioheat equation and then the DRM and the MFS coupled with the analog equation technique are respectively used to derive the particular and homogeneous solutions. Satisfaction of the governing equations and boundary conditions at interpolation points and boundary collocation points can determine all unknowns. Next, numerical experiments are performed to verify the developed meshless algorithm, with numerical results showing that accurate and convergent results can be obtained by using the proposed meshless method in solving the nonlinear bioheat transfer problems considered in the study. Results obtained from the proposed meshless model also show that changes in the blood perfusion rate in terms of temperature play a significant role in altering the temperature distribution within the tissue body. Finally, the sensitivities of the three positive constants in the quadratic form of the blood perfusion rate are evaluated to investigate the temperature changes in the tissue attributable to various parameters. It is found that variations in the second and third coefficients in the expression of quadratic blood perfusion rate can cause evident temperature change.

Chapter 5 Transient Nonlinear Bioheat Transfer with Temperature-dependent Blood Perfusion Rate

5.1 Problem Description

This chapter deals with transient nonlinear bioheat transfer in biological skin tissue. Bioheat behaviour is governed by the well-known Pennes bioheat transfer equation [18]

$$k\nabla^2 T(\mathbf{x},t)+\rho_b c_b \omega_b \left(T_b - T(\mathbf{x},t)\right)+Q_r+Q_m=\rho c\frac{\partial T(\mathbf{x},t)}{\partial t} \tag{5.1}$$

where T is the temperature, ρ the tissue density, c the tissue specific heat, k the tissue thermal conductivity, ρ_b the blood density, c_b the blood specific heat, ω_b the blood perfusion rate, T_b the arterial temperature, Q_r the spatial heat sources, Q_m the metabolic heat generation rate, t the time and ∇^2 the standard Laplacian operator.

As described in Chapter 4, blood flow accelerates with the increase of temperature in the environmental tissue. Thus, the blood perfusion rate can be viewed as a function of tissue temperature [154]. In this case, the governing equation (5.1) can be rewritten in the form of a nonlinear equation as

$$k\nabla^2 T(\mathbf{x},t) + \rho_b c_b \omega_b(T)\left(T_b - T(\mathbf{x},t)\right) + Q_r + Q_m = \rho c \frac{\partial T(\mathbf{x},t)}{\partial t} \tag{5.2}$$

In this study, two types of blood perfusion rate are considered, the linear form and the exponential form.

- Linear form in terms of T [51, 147, 148]

$$\omega_b\left(T\right) = a_1 + a_2 T \tag{5.3}$$

- Exponential form in terms of T [35, 48, 52, 148]

$$\omega_b\left(T\right) = a_1 e^{a_2 T} \tag{5.4}$$

where a_1 and a_2 are positive constants.

For the sake of convenience, a new temperature variable θ is introduced

$$\theta = T - T_b \tag{5.5}$$

Then, the nonlinear governing equation (5.2) can be rewritten in terms of the new variable θ as

$$k\nabla^2\theta - \rho_b c_b \omega_b(\theta + T_b)\theta + Q_r + Q_m = \rho c \frac{\partial \theta}{\partial t} \tag{5.6}$$

or

$$\frac{k}{\rho c}\nabla^2\theta - \frac{\rho_b c_b}{\rho c}\omega_b\left(\theta + T_b\right)\theta + \frac{Q_t}{\rho c} = \frac{\partial\theta}{\partial t} \tag{5.7}$$

where

$$Q_t = Q_r + Q_m \tag{5.8}$$

represents the generalized interior heat source term including the metabolic heat of the tissue and the spatial heat source caused by laser heating or others.

Further, Eq. (5.7) can be expressed in the general unsteady Poisson equation form as

$$\frac{\partial\theta}{\partial t} = \frac{k}{\rho c}\nabla^2\theta + f\left(\theta\right) \tag{5.9}$$

with the following nonlinear source term

$$f\left(\theta\right) = -\frac{\rho_b c_b}{\rho c}\omega_b\left(\theta + T_b\right)\theta + \frac{Q_t}{\rho c} \tag{5.10}$$

Besides the governing equation (5.9), the boundary conditions of the problem and initial condition should be added to form a complete PDE system. Here, the two-dimensional rectangular skin model shown in Figure 4.1 is studied and the same boundary conditions (4.13)-(4.15) are used in the computation. In addition, the initial condition of the problem is given by

$$\theta\left(\mathbf{x}, t = 0\right) = \theta_0\left(\mathbf{x}\right) \tag{5.11}$$

where $\theta_0\left(\mathbf{x}\right)$ is a specific function.

5.2 Algorithm Implementation

In this section, the transient nonlinear PDE system consisting of the nonlinear governing equation (5.9), the boundary conditions (4.13)-(4.15), and the initial condition (5.11) is solved by the meshless method coupled with the OSM involving a two-level time-stepping scheme, the DRM and the MFS, as developed in the next section.

5.2.1 The Operator Splitting Method

To solve this transient nonlinear PDE system, the concept of operator splitting [79] is first used. At this time, the time-dependent governing equation (5.9) can be expressed as a sum of two operators, L_1 and L_2

$$\frac{\partial \theta}{\partial t} = L_1 + L_2 \tag{5.12}$$

with

$$L_1 = \frac{k}{\rho c} \nabla^2 \theta \tag{5.13}$$

$$L_2 = f(\theta) \tag{5.14}$$

For Eq. (5.12), a solution in time can be obtained by a two-level time-stepping scheme including [79]

- The second-order Adams-Bashforth scheme

$$\frac{\theta^{n+1/2}-\theta^{n}}{\Delta t}=\frac{3}{2}f\left(\theta^{n}\right)-\frac{1}{2}f\left(\theta^{n-1}\right) \tag{5.15}$$

- The second-order Adams-Moulton scheme

$$\frac{\theta^{n+1}-\theta^{n+1/2}}{\Delta t}=\frac{1}{2}\left(\frac{k}{\rho c}\nabla^{2}\theta^{n+1}+\frac{k}{\rho c}\nabla^{2}\theta^{n}\right) \tag{5.16}$$

which are respectively employed to model the nonlinear operator L_2 and the Laplacian operator L_1. In Eqs. (5.15) and (5.16), θ^{n-1}, θ^{n}, θ^{n+1} and $\theta^{n+1/2}$ are the temperature at the previous time step $(n-1)$, the current time step (n), the next time step $(n+1)$ and the half time step $(n+\frac{1}{2})$, respectively. $\Delta t = t^{n+1}-t^{n}$ is the length of the time step.

Adding Eq. (5.16) to Eq. (5.15) yields

$$\frac{\theta^{n+1}-\theta^{n}}{\Delta t}=\frac{3}{2}f\left(\theta^{n}\right)-\frac{1}{2}f\left(\theta^{n-1}\right)+\frac{1}{2}\left(\frac{k}{\rho c}\nabla^{2}\theta^{n+1}+\frac{k}{\rho c}\nabla^{2}\theta^{n}\right) \tag{5.17}$$

Further, replacing θ^{n} with $2\theta^{n}-\theta^{n}$ in Eq. (5.17) yields

$$\frac{\theta^{n+1}+\theta^{n}-2\theta^{n}}{\Delta t}=\frac{3}{2}f\left(\theta^{n}\right)-\frac{1}{2}f\left(\theta^{n-1}\right)+\frac{k}{2\rho c}\nabla^{2}\left(\theta^{n+1}+\theta^{n}\right) \tag{5.18}$$

If a new variable θ^* defined by

$$\theta^* = \frac{\theta^{n+1} + \theta^n}{2} \tag{5.19}$$

is introduced, Eq. (5.18) can be transformed to

$$\frac{2\theta^*}{\Delta t} - \frac{2\theta^n}{\Delta t} = \frac{3}{2} f\left(\theta^n\right) - \frac{1}{2} f\left(\theta^{n-1}\right) + \frac{k}{\rho c}\nabla^2\theta^* \tag{5.20}$$

which can be rearranged in the form

$$\nabla^2\theta^* - \frac{2\rho c}{k\Delta t}\theta^* = -\frac{\rho c}{k}\left[\frac{3}{2} f\left(\theta^n\right) - \frac{1}{2} f\left(\theta^{n-1}\right)\right] - \frac{2\rho c}{k\Delta t}\theta^n \tag{5.21}$$

Clearly, Eq. (5.21) is a type of modified Helmholtz equation and θ^* is a generalized function to be determined at each time step. The right nonhomogeneous term in Eq. (5.21) is explicitly known by the previous values of θ^{n-1} and θ^n. Then, the values of θ^{n+1} can be obtained through Eq. (5.19).

Unlike the backward time-stepping scheme, this scheme requires the function values at step (*n*) and the previous step (*n*-1) [155]. Therefore, it cannot start by itself. To begin, the function value at the first time step can be evaluated by the extrapolated explicit forward Euler scheme presented here [79, 132]

$$\frac{\partial\theta}{\partial t} = \frac{\theta^1 - \theta^0}{\Delta t} \tag{5.22}$$

Then we have

$$\rho c \frac{\theta^1 - \theta^0}{\Delta t} = \frac{k}{\rho c} \nabla^2 \theta^1 + f\left(\theta^0\right) \tag{5.23}$$

If the initial guess is set at θ_0, the value of θ_1 for the first time step can be calculated according to Eq. (5.23). Furthermore, the iteration with time can commence from Eq. (5.21).

For the sake of simplicity, Eq. (5.21) is rewritten as

$$\nabla^2 \theta^* - \lambda^2 \theta^* = F \tag{5.24}$$

with

$$\lambda^2 = \frac{2\rho c}{k \Delta t} \tag{5.25}$$

and

$$F = -\frac{\rho c}{k}\left[\frac{3}{2} f\left(\theta^n\right) - \frac{1}{2} f\left(\theta^{n-1}\right)\right] - \frac{2\rho c}{k \Delta t} \theta^n \tag{5.26}$$

As well, the boundary condition equations (4.13)-(4.15) should be modified for the time iteration so that a complete PDE system can be formed in conjunction with the governing equation (5.24) and the modified boundary conditions

$$\begin{cases} \theta^* = \dfrac{\theta_c + \theta^{n-1}}{2} & \text{at boundary } \Gamma_1 \\ -k \dfrac{\partial \theta^*}{\partial n} = 0 & \text{at boundaries } \Gamma_2 \text{ and } \Gamma_3 \\ \theta^* = \dfrac{\theta_s + \theta^{n-1}}{2} & \text{at boundary } \Gamma_4 \end{cases} \tag{5.27}$$

In this subsection, the DRM using RBFs and the MFS using fundamental solutions are applied to solve the modified Helmholtz equation system (5.24)-(5.27). Both methods are based on boundary or internal collocation and have been successfully applied to similar nonhomogeneous problems [59, 60, 62]. The methods are described in detail.

5.2.2 RBF for Particular Solutions

First, the DRM is introduced by simply setting

$$b(\mathbf{x}) = \lambda^2 \theta^*(\mathbf{x}) + F \tag{5.28}$$

and then Eq. (5.24) can be expressed as the following nonhomogeneous Laplace equation

$$\nabla^2 \theta^*(\mathbf{x}) = b(\mathbf{x}) \tag{5.29}$$

According to the linear feature of the Laplace operator, the solution to the Laplace equation (5.29) can be expressed as [60, 62]

$$\theta^*(\mathbf{x}) = \theta_h(\mathbf{x}) + \theta_p(\mathbf{x}) \tag{5.30}$$

where $\theta_h(\mathbf{x})$ is a homogeneous solution satisfying

$$\nabla^2 \theta_h(\mathbf{x}) = 0 \tag{5.31}$$

and $\theta_p(\mathbf{x})$ is a particular solution satisfying

$$\nabla^2 \theta_p(\mathbf{x}) = b(\mathbf{x}) \tag{5.32}$$

Generally, the particular solution cannot be determined exactly. In order to find the approximated particular solution, the RBF approach is employed [61, 66, 139, 153]. The source term $b(\mathbf{x})$ is first approximated by a series of RBFs in the domain of interest [139, 153]

$$b(\mathbf{x}) = \sum_{i=1}^{M} \alpha_i \phi_i(r) \tag{5.33}$$

where ϕ_i stands for a set of RBFs that are defined in terms of the Euclidian distance r between any two interpolation points located in the domain, and α_i are the corresponding interpolating coefficients. M is the number of interpolation points.

Then, the particular solution of Eq. (5.32) is represented in a form similar to that in Eq. (5.33) [61, 66, 139, 153]

$$\theta_p(\mathbf{x}) = \sum_{i=1}^{M} \alpha_i \Phi_i(r) \tag{5.34}$$

where $\Phi_i(r)$ are a set of particular solution kernels satisfying the following differential equation

$$\nabla^2 \Phi_i(r) = \phi_i(r) \tag{5.35}$$

In this analysis, the one-order TPS $\phi_i(r) = r^2 \ln r$ is employed for RBF interpolation. In this case, expressions of the particular solution kernel can be written as [60]

$$\Phi_i(r) = \frac{2\ln r - 1}{32} r^4 \tag{5.36}$$

5.2.3 MFS for Homogeneous Solutions

On the other hand, the homogeneous solution satisfying the Laplace equation (5.31) can be obtained by means of the MFS, in which the linear combination of fundamental solutions in terms of a series of source points $\mathbf{s}_j$ outside the domain is used to approximate the homogeneous solution at an arbitrary field point $\mathbf{x}$, that is,

$$\theta_h(\mathbf{x}) = \sum_{j=1}^{N} \beta_j G_j(\mathbf{x}) \tag{5.37}$$

where N is the number of fictitious source points, β_j are source intensity and $G_j(\mathbf{x}) = G(\mathbf{x}, \mathbf{s}_j)$ is the fundamental solution to the linear Laplace operator [156]

$$\nabla^2 G(\mathbf{x}, \mathbf{s}_j) + \delta(\mathbf{x}, \mathbf{s}_j) = 0 \tag{5.38}$$

and has the form

$$G_j(\mathbf{x}) = -\frac{1}{2\pi} \ln \sqrt{\left(x - x_s^j\right)^2 + \left(y - y_s^j\right)^2} \tag{5.39}$$

5.2.4 Complete Solutions

With the obtained particular and homogeneous approximations, the full solution of the nonhomogeneous Laplace equation (5.29) can be written in the form

$$\theta^*(\mathbf{x}) = \sum_{i=1}^{M} \alpha_i \Phi_i(\mathbf{x}) + \sum_{j=1}^{N} \beta_j G_j(\mathbf{x}) \tag{5.40}$$

The normal derivative of the full solution can then be given by

$$\frac{\partial \theta^*(\mathbf{x})}{\partial n} = -\sum_{i=1}^{M} \alpha_i \frac{\partial \Phi_i(\mathbf{x})}{\partial n} - \sum_{j=1}^{N} \beta_j \frac{\partial G_j(\mathbf{x})}{\partial n} \tag{5.41}$$

For the purpose of simplicity, Eqs. (5.40) and (5.41) are written in matrix form as

$$\theta^*(\mathbf{x}) = \mathbf{U}^*(\mathbf{x})\mathbf{c} \tag{5.42}$$

$$\frac{\partial \theta^*(\mathbf{x})}{\partial n} = \mathbf{Q}^*(\mathbf{x})\mathbf{c} \tag{5.43}$$

where

$$\mathbf{U}^*(\mathbf{x}) = \begin{bmatrix} \Phi_1(\mathbf{x}) & \cdots & \Phi_M(\mathbf{x}) & G_1(\mathbf{x}) & \cdots & G_N(\mathbf{x}) \end{bmatrix} \tag{5.44}$$

$$\mathbf{Q}^*(\mathbf{x}) = \begin{bmatrix} -\frac{\partial \Phi_1(\mathbf{x})}{\partial n} & \cdots & -\frac{\partial \Phi_M(\mathbf{x})}{\partial n} & -\frac{\partial G_1(\mathbf{x})}{\partial n} & \cdots & -\frac{\partial G_N(\mathbf{x})}{\partial n} \end{bmatrix} \tag{5.45}$$

$$\mathbf{c}^{\mathrm{T}} = \begin{bmatrix} \alpha_1 & \cdots & \alpha_M & \beta_1 & \cdots & \beta_N \end{bmatrix} \tag{5.46}$$

Then, applying equation (5.42) and (5.43) to the original governing equation (5.24) at M interpolation points in the domain and the boundary conditions at N boundary collocation points leads to the following system of equations

$$\begin{cases} \left[\mathbf{B}^*(\mathbf{x}_i) - \lambda^2 \mathbf{U}^*(\mathbf{x}_i)\right]\mathbf{c} = F(\mathbf{x}_i) & i = 1 \to M \\ \mathbf{U}^*(\mathbf{x}_j)\mathbf{c} = \dfrac{\theta_c + \theta^{n-1}}{2} & j = 1 \to N_1 \\ \mathbf{Q}^*(\mathbf{x}_k)\mathbf{c} = 0 & k = 1 \to N_2 \\ \mathbf{Q}^*(\mathbf{x}_l)\mathbf{c} = 0 & l = 1 \to N_3 \\ \mathbf{U}^*(\mathbf{x}_m)\mathbf{c} = \dfrac{\theta_s + \theta^{n-1}}{2} & m = 1 \to N_4 \end{cases} \tag{5.47}$$

where N_i $(i = 1, 2, 3, 4)$ are respectively the number of collocation points on the four edges of the rectangular domain and $N_1 + N_2 + N_3 + N_4 = N$. $\mathbf{B}^*$ is the Laplacian operator matrix in the form

$$\mathbf{B}^*(\mathbf{x}_i) = \nabla^2 \mathbf{U}^*(\mathbf{x}_i) = \left[\phi_1(\mathbf{x}_i) \quad \cdots \quad \phi_M(\mathbf{x}_i) \quad 0 \quad \cdots \quad 0\right] \tag{5.48}$$

The unknown coefficient vector $\mathbf{c}$ can be determined by solving the linear equation system (5.47), and then the temperature variable θ^* at each time step can be calculated from Eq. (5.40) or (5.42). Due to the symmetry of the bioheat model in the rectangular domain, only half of the domain is chosen as the solution domain. Figure 5.1 shows an illustration of the 32 collocations, 32 source points and 63 interpolation points for the half rectangular domain in the calculation.

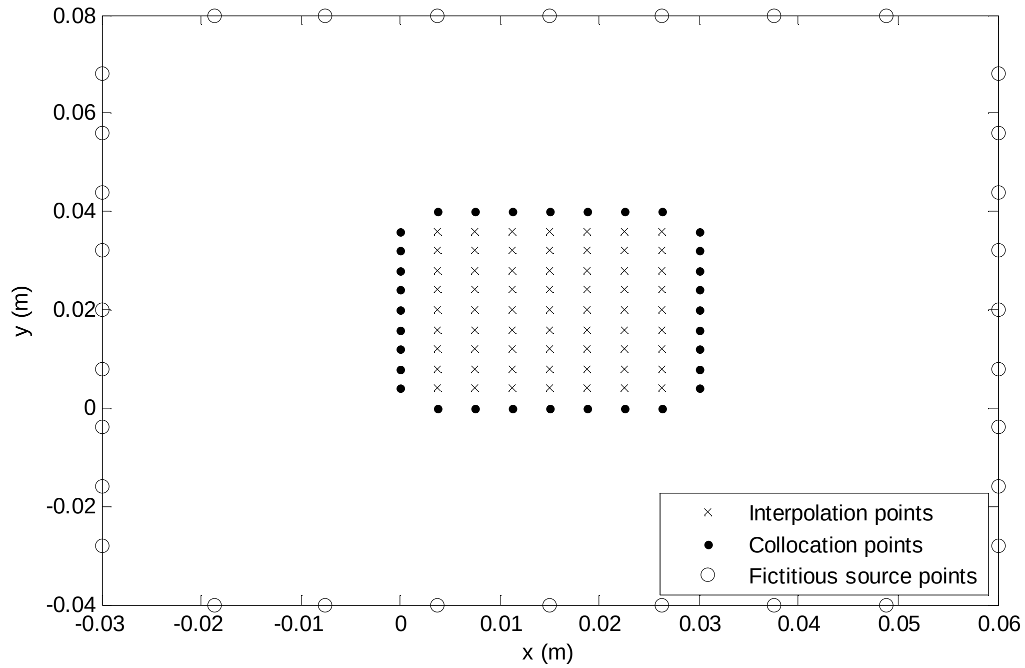

Figure 5.1 Collocation scheme with 63 interpolation points and 32 boundary collocations

5.3 Results and Discussion

In this section, the efficiency and accuracy of the proposed method for analysing transient nonlinear bioheat transfer in a 2D skin tissue are validated by the finite element software ANSYS through a benchmark example. The thermal parameters of the 2D skin tissue model used in the calculation are given in Table 5.1 [59, 148, 149].

The ANSYS Transient thermal toolbox is employed to simulate bioheat transfer in biological material. The mesh generated by ANSYS is shown in Figure 5.2, in which 647 elements and 733 nodes are generated for finite element analysis [157].

Table 5.1 Thermal properties of the skin

Thermal parameters	*Value*
Thermal conductivity k ($\mathrm{Wm^{-1}K^{-1}}$)	0.5
Density of blood ρ_b ($\mathrm{kgm^{-3}}$)	1000
Specific heat of blood c_b ($\mathrm{Jkg^{-1}K^{-1}}$)	4200
Spatial heat Q_r ($\mathrm{Wm^{-3}}$)	30000
Metabolic heat Q_m ($\mathrm{Wm^{-3}}$)	4200
Arterial temperature T_b (ºC)	37
Temperature of body core T_c (ºC)	37
Temperature of skin surface T_s (ºC)	25

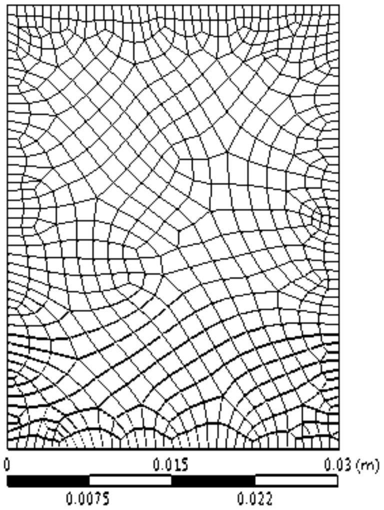

Figure 5.2 Finite element mesh used in ANSYS

5.3.1 Validation of the Proposed Method

For the purpose of comparison, consider that the blood perfusion rate is a linear function of tissue temperature $\omega_b(T) = a_1 + a_2 T$, where $a_1 = 0.0005$ and $a_2 = 0.0001$. A total of 63 interpolation points and 32 boundary collocations (see Figure 5.1) are used to calculate the transient temperature distribution. Numerical results along the *x* axis at three time instants, Δt =50s, 80s and 100s, are presented to show the accuracy and stability of the second-order Adams-Bashforth and Adams-Moulton schemes. From Figure 5.3, it can be seen that the results from the proposed algorithm with fewer collocation points are in good agreement with the results from the ANSYS Transient thermal toolbox. The relative error of the results from the proposed method with respect to those from the Transient thermal toolbox of ANSYS is less than 0.5%.

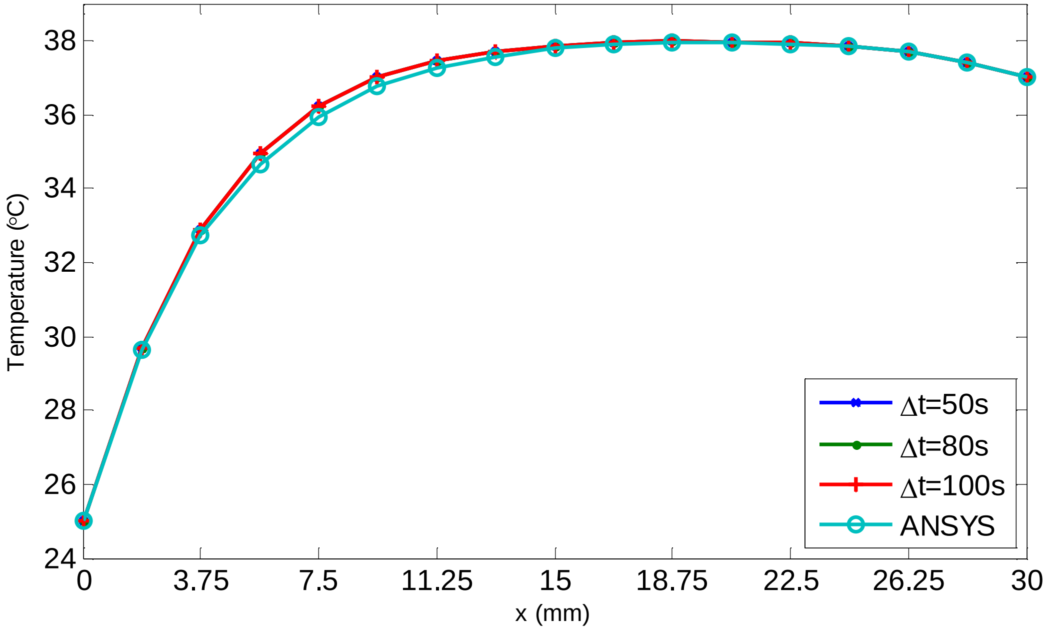

Figure 5.3 Results of temperature along *x* axis for the linear case of blood perfusion rate

Next, the exponential case of the TDBPR $\omega_b(T) = a_1 e^{a_2 T}$ with $a_1 = 0.0005$ and $a_2 = 0.01$ is considered. Again, numerical results along the *x* axis at three time instants Δt =50s, 80s and 100s are evaluated and shown in Figure 5.4. It is evident that there is negligible difference between the results from the proposed algorithm and those from the ANSYS Transient thermal toolbox.

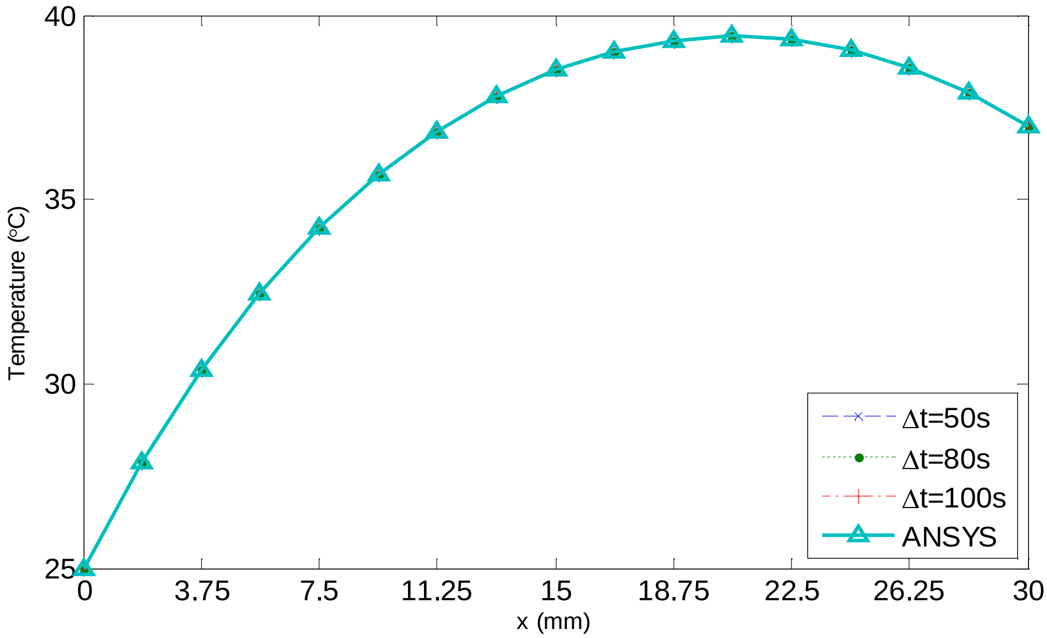

Figure 5.4 Results of temperature along *x* axis for the exponential case of blood perfusion rate

Figure 5.5 presents the temperature variation from *t*=0s to *t*=2560s at the point (1.875mm, 0) on the *x* axis for the case of a linear blood perfusion rate. It can be seen from Figure 5.5 that the variation of temperature with time from the proposed meshless method is almost identical to that obtained from ANSYS, although fewer unknowns are used in the proposed method.

From the above numerical results, the convergence and accuracy of the present meshless method with the higher-order Adams-Bashforth and Adams-Moulton time-stepping schemes are validated for transient nonlinear bioheat analysis in the rectangular model of skin tissue.

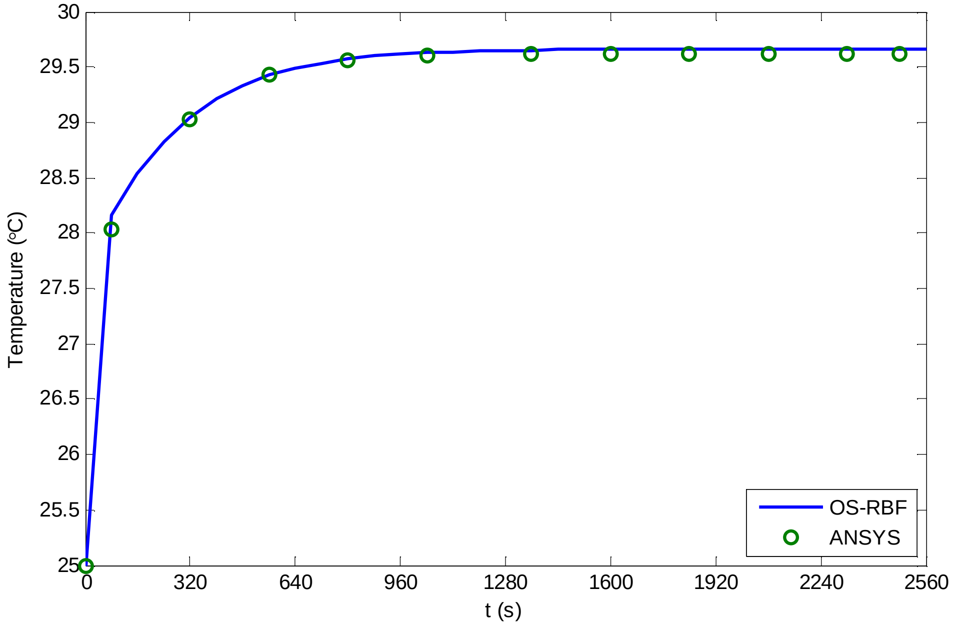

Figure 5.5 Variation of temperature with time for the linear case of blood perfusion rate

More numerical results are now presented to illustrate temperature distribution in the solution domain caused by different TDBPRs. In Figures 5.6 and 5.7, the temperature distribution in the skin tissue along the *x* axis at different times is presented. The steady state in Figure 5.6 is reached much earlier (linear case, at about 1600s) than that in Figure 5.7 (exponential case, at about 8000s). It is also noted that the slope of the steady-state temperature curve along the *x* axis increases and then decreases from left to right for both linear and exponential cases. However, the slope in the linear case appears greater than that in the exponential case in the region close to the left surface, which has a lower environmental temperature, whereas the slope in the linear case becomes less than that in the exponential case in the region close to the right surface, which has a higher body core temperature. Moreover, the exponential-form blood perfusion rate produces a higher interior temperature in the region close to x=18.75mm than that for the linear-form rate. The main reason is that the exponential-form blood perfusion rate generally has a lower value than that of the linear form with the coefficients given above. In the region close to the left of the surface, where the skin tissue temperature is evidently lower than the blood temperature, the greater blood perfusion rate means that more heat flows from blood to skin tissue, causing a rapid increase of the tissue temperature. Thus there is greater temperature gradient in this region for the linear case than the exponential case. When the tissue temperature exceeds the blood temperature, a greater blood perfusion rate causes more heat to flow from tissue to blood and leads to the tissue temperature decrease.

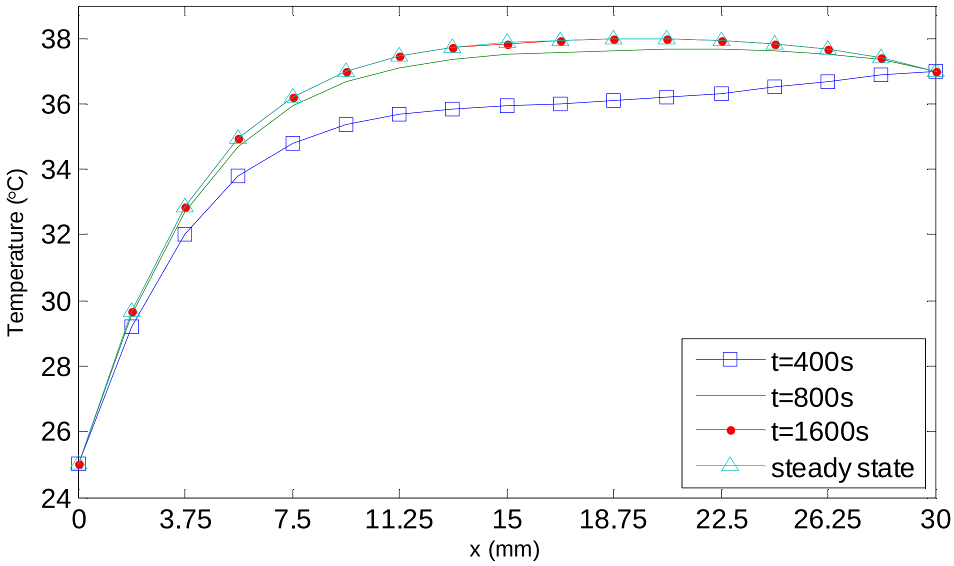

Figure 5.6 Temperature variation vs time along *x* axis for the linear form of blood perfusion rate

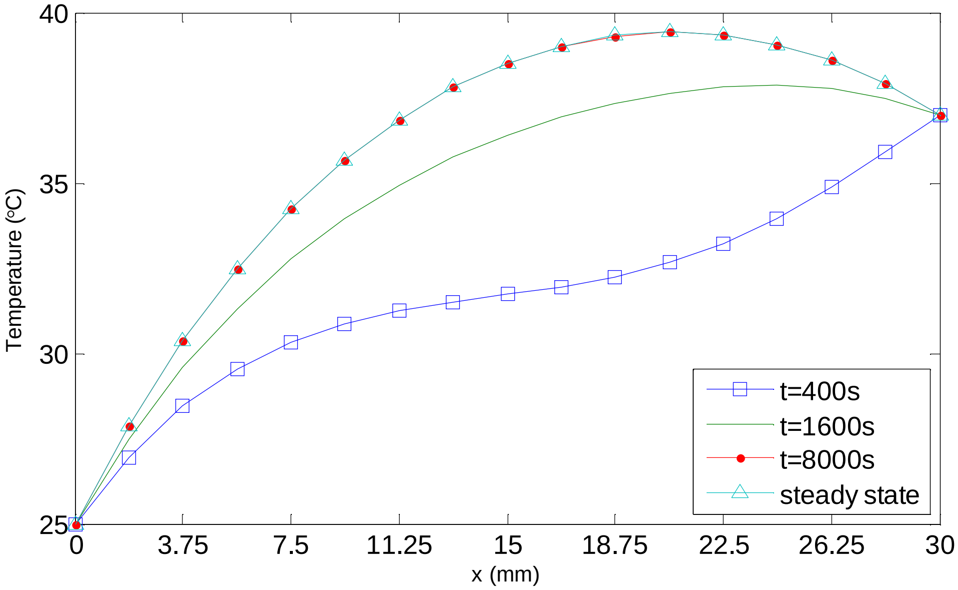

Figure 5.7 Temperature variation vs time along *x* axis for the exponential form of blood perfusion rate

5.3.2 Sensitivity Analysis

In this subsection, the linear case of TDBPR $\omega_b(T) = a_1 + a_2 T$ is considered for the sensitivity analysis of temperature to the constant coefficients a_1 and a_2. First, the coefficient a_2 is set to be constant 0.0002 and the constant a_1 is assumed to be 0.005, 0.0005 and 0.00005. As evident in Figure 5.8, the steady-state temperatures are quite close to each other when $a_1 = 0.00005$ and $a_1 = 0.0005$. But the skin temperature curve has a relatively larger gap from the two curves mentioned above when $a_1 = 0.005$. The three temperature curves intersect at the point (12.65mm, 0), at which the skin temperature is approximately 37°C. Therefore, from the left surface of the skin tissue to the approximate location point (12.65mm, 0), the greater blood perfusion rate indicates that more heat flow transfer occurs between the blood and skin tissue. If the blood temperature is higher than that in the skin tissue, more heat flows from blood to skin tissue, causing a rapid increase in skin temperature. If the blood temperature is lower than that in the skin tissue, more heat flow transfers from skin tissue to blood, causing a rapid decrease in skin temperature. It can be seen that blood perfusion protects the skin tissue from extreme temperature increases or decreases caused by the environment.

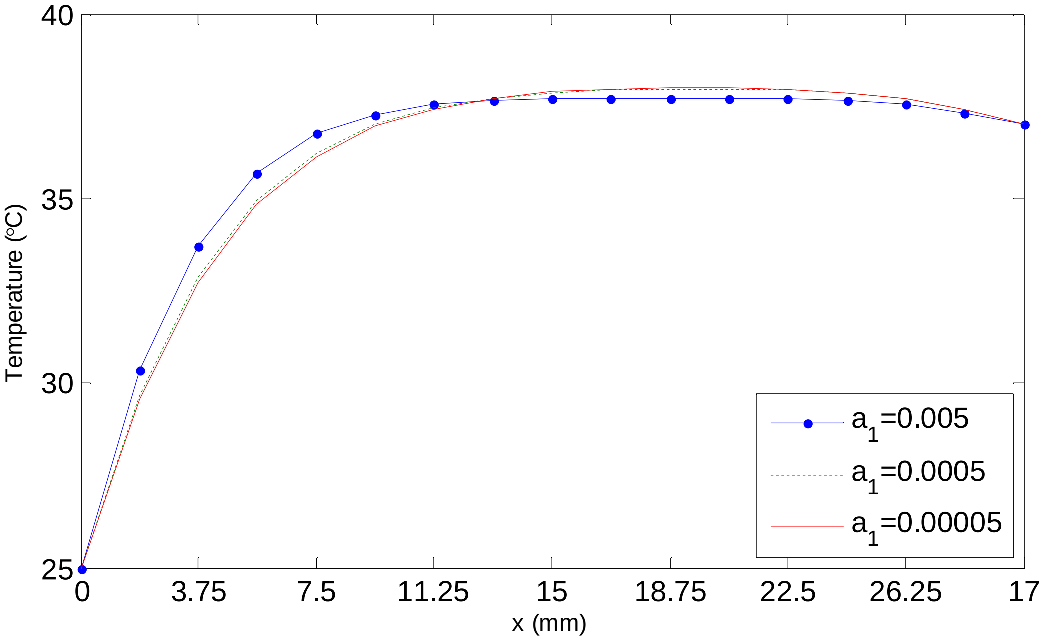

Figure 5.8 Sensitivity of temperature to *a_1* in the linear case of blood perfusion rate

To study the effect of a_2 on skin temperature, we assume the first constant a_1 to be 0.0005 and the second constant a_2 is set as 0.00002, 0.0002 and 0.002. From Figure 5.9, it can be seen that variation of the constant a_2 causes a more rapid change in the steady-state temperature curve than that due to variation of the constant a_1. In particular, when the constant $a_2 = 0.002$, the curve of the tissue temperature is steeper than the other two curves. The highest value of the skin temperature appears at the approximate location (7.5mm, 0), which is closer to the left boundary of the skin tissue than to the other two curves. From location (15mm,

0) to (26.25mm, 0), the skin tissue temperature is stable at a certain level when the constant $a_2 = 0.002$.

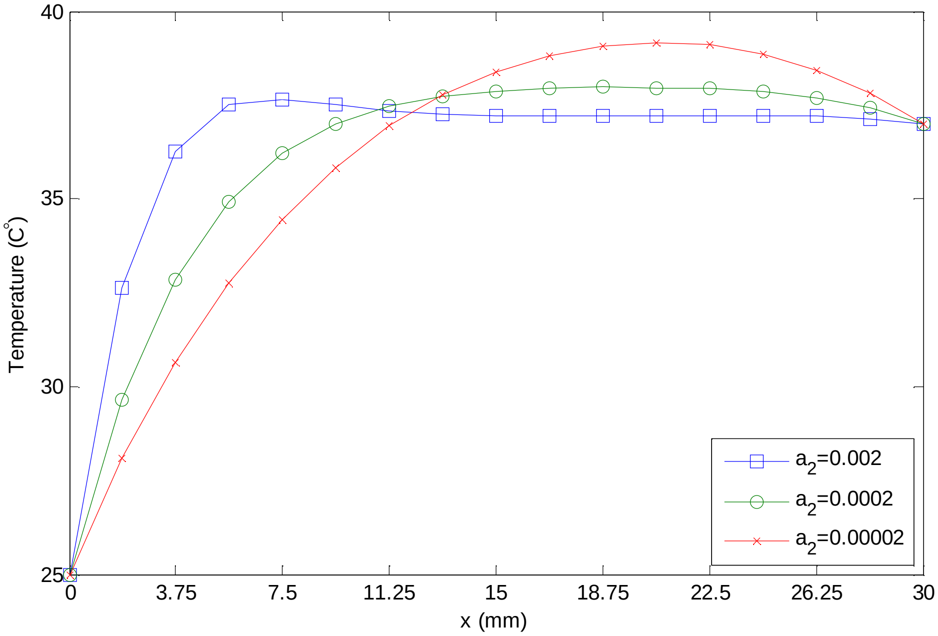

Figure 5.9 Sensitivity of temperature to *a₂* in the linear case of blood perfusion rate

Next, the sensitivity of temperature to the constant coefficients $a_i \ (i = 1, 2)$ is investigated by considering the exponential case of TDBPR $\omega_b(T) = a_1 e^{a_2 T}$. Assume that the constant a_2 is 0.01, and the constant a_1 is tested at 0.005, 0.0005 and 0.00005. Compared with the linear case shown in Figure 5.9, the difference or gap between each skin temperature curve is relatively greater, as shown in Figure 5.10.

Similarly, the three temperature curves with different values of constant a_1 intersect at almost the same point (the distance from the left boundary being roughly 13.125mm). This finding means that, at location (13.125mm, 0), the skin temperature has almost the same value of 37.75ºC for different values of constant a_1. Figure 5.10 illustrates the stronger regulatory and protective effect of the exponential-form blood perfusion rate than that in the linear case (see Figure 5.9).

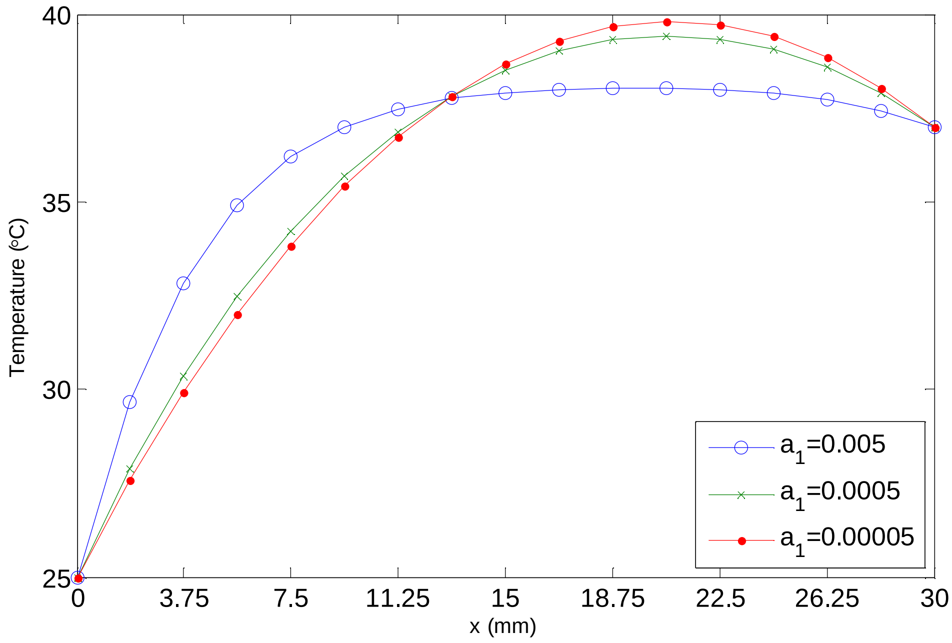

Figure 5.10 Sensitivity of temperature to a_1 in the exponential case of blood perfusion rate

Again, assume constant a_1 to be 0.0005, while constant a_2 is set to be 0.03, 0.01 and 0.003. As evident from Figure 5.11, when constant $a_2 = 0.03$, the temperature of the skin tissue increases more steeply before the point (11.25mm, 0), but the curve is flatter than the temperature curves with smaller values of a_2. Compared with the effect of the different values of a_1 in Figure 5.10, the increase in the value of a_2 causes a greater reduction of the peak value of the skin tissue temperature and the temperature becomes more stable from location (11.25mm, 0) to (26.25mm, 0). In summary, an increase in the value of constant a_2 has higher sensitivity to the temperature of skin tissue than an increase in the value of constant a_1. Simultaneously, it is found that an increase in the blood perfusion rate causes the temperature of the skin tissue to reach its final steady state more quickly and reduces the peak value of the tissue temperature. That means that if the skin tissue absorbs a large amount of biological heat from its environment, the blood perfusion effect causes the temperature to reach a certain value quickly and reduces the risk of burning of the skin tissue.

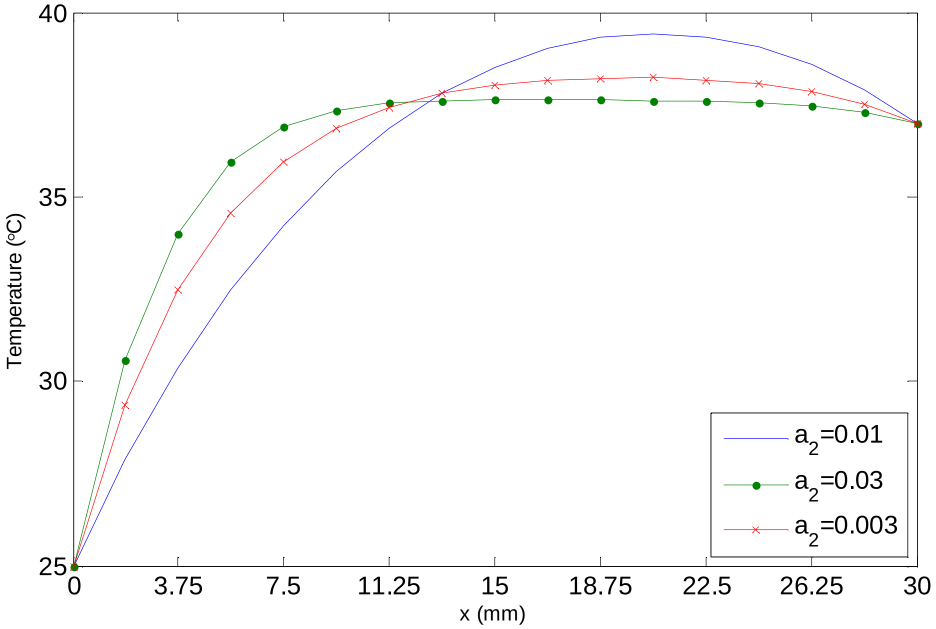

Figure 5.11 Sensitivity to a_2 in the exponential case of blood perfusion rate

5.4 Summary

In this chapter, an operator splitting technique coupled with the DRM and the MFS is presented to develop a mesh-free algorithm for solving the transient nonlinear bioheat transfer in a 2D rectangular skin model with a TDBPR. Use of the operator splitting technique including two-level second-order time-stepping schemes makes it possible to establish an accurate and convergent solution procedure for transient and nonlinear cases, and then the DRM and the MFS are respectively employed to solve the obtained modified Helmholtz equation system at each time step. This meshless method is dependent only on the internal interpolating points and boundary collocation points of the domain, and thus is really meshless and dimension-independent. The numerical results demonstrate the accuracy and efficiency of the meshless method in the analysis of the transient nonlinear bioheat transfer problem under consideration, with very few interpolation and collocation points. Moreover, the analysis of temperature change sensitivity to the constant coefficients in the linear and exponential expressions of the blood perfusion rate demonstrates the increase in the constant a_2 in the linear case. It is found that the exponential case has a more significant influence on the tissue temperature distribution than the constant a_1, and an increase in its value results in a relatively fast increase in the tissue temperature in the region close to the outer surface and, simultaneously, the peak temperature value decreases. This reflects the regulatory and protective effect of the blood perfusion rate in biological tissue.

Chapter 6 Conclusion and Future Work

6.1 Conclusions

In the present work, a transient HFS-FEM algorithm is developed for analysing bioheat transfer in two-dimensional skin tissue under laser irradiation. The effects of blood perfusion, metabolic heat and spatial heating induced by a Gaussian type laser beam are considered by way of the Pennes bioheat governing equation. Numerical results from the HFS-FEM coupled with RBF are first validated by comparison with analytical solutions, and good agreement is observed.

In the next step, a meshless DRM-MFS algorithm is developed for analysing the nonlinear bioheat transfer in a 2D skin model. The nonlinearity is due to the temperature dependence of the blood perfusion rate. The Taylor expansion technology is first employed to linearize the nonlinear bioheat equation and then the DRM and the MFS coupled with the analog equation technique are used to derive the particular and homogeneous solutions. Satisfaction of the governing equations and boundary conditions at interpolation points and boundary collocation points can determine all unknowns. Next, numerical experiments are performed to verify the developed meshless algorithm and numerical results show that accurate and convergent results can be obtained by using the proposed meshless method in solving the nonlinear bioheat transfer problems considered. Also, results obtained from the proposed meshless model show that the change in the blood perfusion rate in terms of the temperature variable plays a significant role in altering the temperature distribution within the tissue body. It is also found that variations of the second and third coefficients in the expression of the quadratic blood perfusion rate can cause evident temperature change.

In the third step, an operator splitting technique coupled with the DRM and the MFS is presented to develop a mesh-free algorithm for solving transient nonlinear bioheat transfer in a 2D model of skin tissue with a TDBPR. Use of the operator splitting technique with two-level second-order time-stepping schemes makes it possible to establish an accurate and convergent solution procedure for transient and nonlinear cases, and then the DRM and the MFS are employed to solve the obtained modified Helmholtz equation system at each time step. This meshless method is dependent only upon the internal interpolating points and boundary collocation points of the domain, and thus is really meshless and dimension-independent. The numerical results demonstrate the accuracy and efficiency of the meshless method in the analysis of the transient nonlinear bioheat transfer problem under consideration, with very few interpolation and collocation points. It is found that the exponential case has a more significant influence on the tissue temperature distribution than the constant a_1 , and an increase in its value results in a relatively fast increase in the tissue temperature in the region close to the outer surface, and simultaneously, the peak temperature value decreases. This reflects the regulatory and protective effect of blood perfusion rate in biological tissue.

Finally, the proposed HFS-FEM method is effective for calculating the transient state temperature distribution in a 2D human eye model. Good agreement of the simulation results between the proposed HFS-FEM and ABAQUS are observed. These findings mean that we can obtain almost the same simulation results by HFS-FEM, with many fewer elements and a lower degree of freedom, compared with ABAQUS. Therefore, the effectiveness of the proposed HFS-FEM is proved in solving the transient linear bioheat transfer problem in a 2D human eyeball model. This method provides an effective option in the simulation of both the steady state and the transient state bioheat transfer model.

6.2 Future Work

In future work, the author and colleagues would like to develop the current two-dimensional skin tissue models from homogeneous tissue with an isotropic single property to three layers with different thermal properties. Also the multiple sub-domains, namely the cornea, aqueous humor, lens, vitreous and sclera with different thermal properties, in the two-dimensional human eyeball model need to be considered and calculated in the analysis of transient bioheat in an eyeball with laser interaction.

For the transient term in the Pennes bioheat transfer governing equation, the Laplace transform method would be used to solve the transient state bioheat transfer problem rather than the previous finite difference method.

Furthermore, the three-dimensional (3D) linear bioheat transfer, 3D nonlinear bioheat model and 3D linear bioheat model in tissues under laser injection models would be used in the bioheat transfer problems.

Next, the radial integration method would be applied to solve the 2D and 3D singular and domain integrals generated in the governing functional rather than the previous RBF method used.

Appendix A Parameter Values and Description

c	Specific heat of tissue ($\mathrm{Jkg^{-1}K^{-1}}$)
c_b	Specific heat of blood ($\mathrm{Jkg^{-1}K^{-1}}$)
h_∞	Convection coefficient of ambient fluid ($\mathrm{Wm^{-2}K^{-1}}$)
k	Thermal conductivity of tissue ($\mathrm{Wm^{-1}K^{-1}}$)
L	Width of 2D skin model (m)
P_{in}	Laser power setting (W)
q	Heat flux ($\mathrm{Wm^{-2}}$)
Q_m	Metabolic heat of tissue ($\mathrm{Wm^{-3}}$)
Q_r	Spatial heat ($\mathrm{Wm^{-3}}$)
Q_t	Sum of metabolic heat and spatial heat ($\mathrm{Wm^{-3}}$)
t	Time (s)
Δt	Time step (s)

T	Temperature of tissue (ºC)
T_a	Artery temperature (ºC)
T_c	Temperature of body core (ºC)
T_∞	Sink temperature of ambient fluid (ºC)
ρ	Density of tissue (kgm^{-3})
ρ_b	Density of blood (kgm^{-3})
σ	Standard deviation of laser beam profile (m)
ω_b	Blood perfusion rate ($m^3s^{-1}m^{-3}$)
μ_a	Absorption coefficient of tissue (m^{-1})
P	Pre-exponential factor (s^{-1})
ΔE	Activation energy ($Jkmol^{-1}$)
R	Universal gas constant ($Jkmol^{-1}K^{-1}$)

Appendix B MATLAB Code

```
function [NT,TC,UC]=MFS_RBF_2DNonlinearSkinModel
% Iteratively solve 2D transient bioheat problems in nonlinear skin bioheat model using the DRM-MFS and operator splitting technique
%
% **** 2D transient nonlinear equation of skin bioheat:
%       kD2t(T)+wb*rhob*cb*(T-Tb)+Qr+Qm=rho*c*dT/dt
% with B.C.
%      Potential B.C:    T1=Tc   T4=Ts   q2=q3=0
% where T is the sought field function
%
%----------------------------------------------------------------
% **** Variable statments:
%   NDIM: Dimensions of the problem
%   NDN: Number of DOFs at each point
%
%   NNR: Number of nodes on the physical boundary
%   RC = NNR by NDIM matrix: Coordinates of boundary nodes
%   RN = NNR by NDIM matrix: Normal at boundary nodes
%   KODE = NNR by NDN matrix: Types of given boundary conditions
%   FI = NNR by NDN matrix: Values of given boundary conditions
```

```
%
%   NNV: Number of source nodes outside the domain
%   VC = NNV by NDIM matrix: Coordinates of source nodes
%
%   NNI: Number of interpolation points in the domain
%   IC = NNI by NDIM matrix: Coordinates of interpolation points
%
%   NT: Number of computing points in the domain
%   TC = NT by NDIM matrix: Coordinates of computing points
%
%   Title = 101 by 1 array: problem description
%

%****************************************************************

% Open input data file
XX=input('Input data file name: ','s'); % The name of input data file is *.txt
fp=fopen(XX,'rt');
if(fp<0)
    display('Could not find data file!');
    return;
end

% **** Initial guess at NNI interpolation points
[U0,UX0,UY0]=InitialGuess(NNI,IC);
%
U00=U0;
UX00=UX0;
```

```
UY00=UY0;

%

U0=U0-12;

U01=(30000+4200)*80/1000/4200*U0;

UX01=(30000+4200)*80/1000/4200*UX0;

UY01=(30000+4200)*80/1000/4200*UY0;


% **** Iteration loop

eps=1.0e-4;

nor=1;

Numit=0;

N=NNV+NNI; % default selection is NNR=NNV

while nor>=eps

    Numit=Numit+1;

    disp('Number of iteration =');

    disp(Numit);

    if Numit>1

        U0=U01;

        UX0=UX01;

        UY0=UY01;

        U01=U1;

        UX01=UX1;

        UY01=UY1;

    end

    % ***** Form the system matrix and right hand vector

    HH=zeros(N,N);

    FF=zeros(N,1);

    [HH,FF]=FMAT(NDIM,NDN,NNR,RC,RN,KODE,FI,NNV,VC,NNI,IC,...,
U0,UX0,UY0,U01,UX01,UY01); % Modified
```

```
    % **** Solve the linear system of equations
    [FF,Condnum]=SVDSolver(N,HH,FF);
    % **** Compute u and ux, uy at interpolation points
    U1=zeros(NNI,1);
    UX1=zeros(NNI,1);
    UY1=zeros(NNI,1);
    [U1,UX1,UY1]=SolutionIP(NDIM,NDN,NNV,VC,NNI,IC,FF);
    UStepXY=zeros(NT,3);
    UStepXY=TPC(NDIM,NDN,NNV,VC,NNI,IC,NT,TC,FF);
    UStep=zeros(NT,1);
    UStep=UStepXY(:,1)+37;
    nor=norm(U1-U0);
    if Numit>500
        error('Warning: Exceed the maximum number of iteration!');
        return;
    end
end
disp('Solving nonlinear system of equations is OK!');

% *********** Give quantities at computing points ***********
UC=zeros(NT,3);
UC=TPC(NDIM,NDN,NNV,VC,NNI,IC,NT,TC,FF);

% *********** Output results ***********
OUTPUT(NDIM,NDN,NNR,NNV,NNI,NT,TC,UC,Title,U0,UX0,UY0,Numit);

close all;
```

```
%============================================

% Subroutine Initial Guess

%============================================

function [U0,UX0,UY0]=InitialGuess(NNI,IC)

% Give the initial guess at interpolation points

X=IC(:,1);

Y=IC(:,2);

U0=zeros(NNI,1); % column vector

UX0=zeros(NNI,1);

UY0=zeros(NNI,1);



%============================================

% Subroutine FMAT

%============================================

function [HH,FF]=FMAT(NDIM,NDN,NNR,RC,RN,KODE,FI,NNV,VC,NNI,IC,...,

U0,UX0,UY0,U01,UX01,UY01)

% Form the system matrix HH and the right hand vector FF

% declaration of global variables

global TypeRBF cparameter OrderN;

N=NNV+NNI; % total unknowns

HH=zeros(N,N);

FF=zeros(N,1);

%

k=0.5; % Thermal conductivity

rho=1000; % Blood Density

a1=0.0005; % linear coefficient

a2=0.0002; % linear coefficient
```

```
cb=4200; % Specified heat

Tb=37; % Blood temperature

deltat=80; % Time step

% Satisfy boundary conditions at NNR nodes

for i=1:NNR

    x=RC(i,1);

    y=RC(i,2);

    nx=RN(i,1);

    ny=RN(i,2);

    for j=1:N

        if (j<=NNV)

            xj=VC(j,1);

            yj=VC(j,2);

            [h,hx,hy]=FDS2D(x,y,xj,yj);

        else

            xj=IC(j-NNV,1);

            yj=IC(j-NNV,2);

            % [h,hx,hy,hxx,hxy,hyy]=RBF2D(x,y,xj,yj);

            % Modified

            [h,hx,hy]=BigRBF2D(x,y,xj,yj);

        end

        qx=k*hx;

        qy=k*hy;

        q=-(qx*nx+qy*ny);

        if (KODE(i,1)==0) % Specified potential

            HH(i,j)=h;

        elseif (KODE(i,1)==1) % Specified flux

            HH(i,j)=q;

        elseif (KODE(i,1)==2) % Specified mixture of potential and flux
```

```
            HH(i,j)=Henv*h-q;
        end
    end
    FF(i,1)=FI(i);
end
% Satisfy the governing equation at NNI interior interpolation points
for i=1:NNI
    x=IC(i,1);
    y=IC(i,2);
    u=U0(i,1);
    ux=UX0(i,1);
    uy=UY0(i,1);
    u1=U01(i,1);
    ux1=UX01(i,1);
    uy1=UY01(i,1);
    %
    wb=a1+a2*(u+Tb); % Linear case
    wb1=a1+a2*(u1+Tb);
    f1=-rho*cb/rho/cb*wb*u+(30000+4200)/rho/cb;
    f2=-rho*cb/rho/cb*wb1*u1+(30000+4200)/rho/cb; % Modified 3rd paper
    An=2*rho*cb/k/deltat;
    for j=1:N
        if (j<=NNV)
            xj=VC(j,1);
            yj=VC(j,2);
            [h,hx,hy,hxx,hxy,hyy]=FDS2D(x,y,xj,yj);
            BB=0; % M
            UU=h; % M
        else
```

```
            xj=IC(j-NNV,1);

            yj=IC(j-NNV,2);

            [h,hx,hy,hxx,hxy,hyy]=RBF2D(x,y,xj,yj);

            BB=h;

            [hh,hx,hy]=BigRBF2D(x,y,xj,yj);

            UU=hh; % Calculate capital Fai for RBF

        end

        HH(i+NNR,j)=BB-An*UU;

    end

    FF(i+NNR,1)=CFXY(x,y,f1,f2,u1);

end



%============================================

% Subroutine BigRBF2D

%============================================

%

function [h,hx,hy]=BigRBF2D(x,y,xj,yj)

% Particular solution kernels h and its derivatives at field point (x,y)

% (xj,yj): the central point


rx=x-xj;

ry=y-yj;

r=sqrt(rx^2+ry^2);


% Thin plate spline RBF=(r^2)*ln(r)


if (r+1==1) % r=0

      lnr=1.0;
```

```
else
      lnr=log(r);
end

h=(2*lnr-1)/32*r^4;
hx=(4*lnr-1)/16*r^2*rx;
hy=(4*lnr-1)/16*r^2*ry;


%===========================================
% Subroutine CFXY
%===========================================
function f=CFXY(x,y,f1,f2,u1)
% Compute f(x,y) at a given point (x,y)
% x, y and f are scales
Qm=4200;
Qr=30000; % Can be adjusted according to different outer factors such as later power adjustment
Qt=Qr+Qm;
k=0.5; % Thermal conductivity
rho=1000; % Modified
c=4200; % Modified
deltat=80; % Modified
f=-rho*c/k/2*(3*f2-f1)-2*rho*c/k/deltat*u1;


%===========================================
% Subroutine FDS2D
%===========================================
```

```
function [h,hx,hy,hxx,hxy,hyy]=FDS2D(x,y,xj,yj)
% Compute the fundamental solution at the field point (x,y) and the source
% point(xj,yj)
% x, y, xj, yj are scales
rx=x-xj;
ry=y-yj;
r=sqrt(rx^2+ry^2);
if (r+1==1)
    error('Distance of the field pint and the source point should be nonzero!');
end
rx=rx/r;
ry=ry/r;
h=log(1.0/r)/(2*pi);               % u*
hx=-(1.0/2/pi/r)*rx;               % du*/dx
hy=-(1.0/2/pi/r)*ry;               % du*/dx
hxx=-(1.0/2/pi)*(ry*ry-rx*rx)/r/r; % d2u*/dx/dx
hxy=(1.0/pi)*(rx*ry)/r/r;          % d2u*/dx/dy
hyy=-hxx;                          % d2u*/dy/dy


%===========================================
% Subroutine RBF2D
%===========================================
%
function [h,hx,hy,hxx,hxy,hyy]=RBF2D(x,y,xj,yj)
% Compute RBF at the field point (x,y) and the central
% point(xj,yj)
```

```
% x, y, xj, yj are scales
% Differential scheme
rx=x-xj;
ry=y-yj;
r=sqrt(rx^2+ry^2);
% Thin plate spline RBF=(r^n)ln(r)
n=2;
rn=r^n;
rn1=r^(n-1);
rn2=r^(n-2);
rn3=r^(n-3);
rn4=r^(n-4);
if (r+1==1) % r=0
      lnr=1.0;
else
      lnr=log(r);
end

h=rn*lnr;
hx=rn2*rx*(n*lnr+1);
hy=rn2*ry*(n*lnr+1);
hxx=rn4*rx*rx*((n*n-2*n)*lnr+2.0*(n-1))+rn2*(n*lnr+1);
hxy=rn4*rx*ry*((n*n-2*n)*lnr+2.0*(n-1));
hyy=rn4*ry*ry*((n*n-2*n)*lnr+2.0*(n-1))+rn2*(n*lnr+1);



%============================================
% Subroutine EQUIL
%============================================
```

```
%
function [A,b]=EQUIL(n,A,b)
% Equilibration treatment of Ax=b
%
% Determine the maximum element in each row and store them in column vector
% temp
temp=(max(abs(A')))';
% Elements in each row divide the maximum element
for i=1:n
    A(i,:)=A(i,:)/temp(i);
end
b=b./temp;


%===========================================
% Subroutine SVDSolver
%===========================================

function [x,condnum]=SVDSolver(n,A,b)
% The system of linear equations (SLE) solver using standard SVD
%            [U,S,V]=svd(A) and A=U*S*V'
% where A is a square matrix, U and V are unitary matrices and S is a
% diagonal matrix with nonnegative elements in decreasing order for linear
% system A*x=b, finally we have x= V*[diag(1/sj)]*U'*b and in the process
% we simply replace 1/sj by zero if sj=0
%
x=zeros(n,1);
% equilibration treatment
[A,b]=EQUIL(n,A,b);
```

```
% condition number
condnum=cond(A);
% SVD
[U,S,V]=svd(A);
% zeroing the small singular values
for i=1:n
    if (S(i,i)+1)==1
        S(i,i)=0;
    else
        S(i,i)=1/S(i,i);
    end
end
% solve x= V*[diag(1/sj)]*U'*b
x=V*(S*U'*b);
clear U S V A b;



%============================================
% Subroutine SolutionIP
%============================================

function [U1,UX1,UY1]=SolutionIP(NDIM,NDN,NNV,VC,NNI,IC,FF)
% Compute potential and its derivatives at interpolation points
N=NNV+NNI; % Total number of knowns
U=zeros(NNI,3);
for i=1:NNI
    x=IC(i,1);
    y=IC(i,2);
    for j=1:N
```

```
        if j<=NNV
            xj=VC(j,1);
            yj=VC(j,2);
            [h,hx,hy,hxx,hxy,hyy]=FDS2D(x,y,xj,yj);
        else
            xj=IC(j-NNV,1);
            yj=IC(j-NNV,2);
            % [h,hx,hy,hxx,hxy,hyy]=RBF2D(x,y,xj,yj);
            [h,hx,hy]=BigRBF2D(x,y,xj,yj);
        end
        U(i,1)=U(i,1)+FF(j,1)*h;
        U(i,2)=U(i,2)+FF(j,1)*hx;
        U(i,3)=U(i,3)+FF(j,1)*hy;
    end
end
U1=U(:,1);
UX1=U(:,2);
UY1=U(:,3);


%============================================
% Subroutine TPC
%============================================
%
function UC=TPC(NDIM,NDN,NNV,VC,NNI,IC,NT,TC,FF)
% Compute potential and its derivatives at computing points
N=NNV+NNI; % Total number of knowns
UC=zeros(NT,3);
for i=1:NT
```

```
    x=TC(i,1);
    y=TC(i,2);
    for j=1:N
        if (j<=NNV)
            xj=VC(j,1);
            yj=VC(j,2);
            [h,hx,hy,hxx,hxy,hyy]=FDS2D(x,y,xj,yj);
        else
            xj=IC(j-NNV,1);
            yj=IC(j-NNV,2);
            % [h,hx,hy,hxx,hxy,hyy]=RBF2D(x,y,xj,yj);
            [h,hx,hy]=BigRBF2D(x,y,xj,yj);
        end
        UC(i,1)=UC(i,1)+FF(j,1)*h;
        UC(i,2)=UC(i,2)+FF(j,1)*hx;
        UC(i,3)=UC(i,3)+FF(j,1)*hy;
    end
end
```

Bibliography

[1] Xu F, Lu TJ, Seffen KA. Biothermomechanics of skin tissues. Journal of the Mechanics and Physics of Solids 2008;56(5): 1852-84.

[2] Whitton JT, Everall JD. The thickness of the epidermis. British Journal of Dermatology 1973;89(5): 467-76.

[3] Elwassif MM, Kong Q, Vazquez M, Bikson M. Bio-heat transfer model of deep brain stimulation induced temperature changes. Engineering in Medicine and Biology Society, 2006 EMBS '06 28th Annual International Conference of the IEEE2006. 3580-83.

[4] Kotte ANTJ, Leeuwen GMJv, Lagendijk JJW. Modelling the thermal impact of a discrete vessel tree. Physics in Medicine and Biology 1999;44(1): 57.

[5] Mishima S, Maurice DM. The effect of normal evaporation on the eye. Experimental Eye Research 1961;1(1): 46-52.

[6] Wieringen Nv, Kotte ANTJ, Leeuwen GMJv, Lagendijk JJW, Dijk JDPv, Nieuwenhuys GJ. Dose uniformity of ferromagnetic seed implants in tissue with discrete vasculature: a numerical study on the impact of seed characteristics and implantation techniques. Physics in Medicine and Biology 1998;43(1): 121.

[7] Qin QH, Zhang WC. A new meshless method for 2D heat transfer in skin tissues with moving boundary. Universal Journal of Engineering Mechanics 2013;1: 50-70.

[8] Zhang ZW, Wang H, Qin QH. Analysis of transient bioheat transfer in the human eye using hybrid finite element model. Applied Mechanics and Materials 2014;553: 356-61.

[9] Wang H, Qin QH. Computational bioheat modeling in human eye with local blood perfusion effect. Human Eye Imaging and Modeling2012. 311-28.

[10] Yen A, Braverman IM. Ultrastructure of the human dermal microcirulation: the horizontal plexus of the papillary dermis Journal of Investigative Dermatology 1976;66(3): 131-42.

[11] Conrad MC, Anderson JL, Garrett JB. Chronic collateral growth after femoral artery occlusion in the dog. Journal of Applied Physiology 1971;31(4): 550-55.

[12] Hales JRS, Iriki M, Tsuchiya K, Kozawa E. Thermally-induced cutaneous sympathetic activity related to blood flow through capillaries and arteriovenous anastomoses. Pflügers Archiv 1978;375(1): 17-24.

[13] Koijk JFvd, Crezee J, Leeuwen GMJv, Battermann JJ, Lagendijk JJW. Dose uniformity in MECS interstitial hyperthermia: the impact of longitudinal control in model anatomies. Physics in Medicine and Biology 1996;41(3): 429.

[14] Belmiloudi A. Analysis of the impact of nonlinear heat transfer laws on temperature distribution in irradiated biological tissues: mathematical models and optimal controls. Journal of Dynamical and Control Systems 2007;13(2): 217-54.

[15] Arkin H, Xu LX, Holmes KR. Recent developments in modeling heat transfer in blood perfused tissues. Biomedical Engineering, IEEE Transactions on 1994;41(2): 97-107.

[16] Akbarzadeh AH, Pasini D. Phase-lag heat conduction in multilayered cellular media with imperfect bonds. International Journal of Heat and Mass Transfer 2014;75(0): 656-67.

[17] Alexis K, Gerard van L, Jacob de B, John van der K, Hans C, Jan L. A description of discrete vessel segments in thermal modelling of tissues. Physics in Medicine and Biology 1996;41(5): 865.

[18] Pennes HH. Analysis of tissue and arterial blood temperatures in the resting human forearm. Journal of Applied Physiology 1948;1(2): 93-122.

[19] Fung YC. Biomechanics: Motion, Flow, Stress, and Growth: Springer-Verlag; 1990.

[20] Alessandro S, Rodolfo R, Chiara C. Eye rotation induced dynamics of a Newtonian fluid within the vitreous cavity: the effect of the chamber shape. Physics in Medicine and Biology 2007;52(7): 2021.

[21] Brinkmann R, Radt B, Flamm C, Kampmeier J, Koop N, Birngruber R. Influence of temperature and time on thermally induced forces in corneal collagen and the effect on laser thermokeratoplasty. Journal of Cataract & Refractive Surgery 2000;26(5): 744-54.

[22] Chua KJ, Ho JC, Chou SK, Islam MR. On the study of the temperature distribution within a human eye subjected to a laser source. International Communications in Heat and Mass Transfer 2005;32(8): 1057-65.

[23] Ooi EH, Ang WT, Ng EYK. A boundary element model of the human eye undergoing laser thermokeratoplasty. Computers in Biology and Medicine 2008;38(6): 727-37.

[24] Koijk JFvd, Crezee J, Lagendijk JJW. Thermal properties of capacitively coupled electrodes in interstitial hyperthermia. Physics in Medicine and Biology 1998;43(1): 139.

[25] Wainwright PR. Computational modelling of temperature rises in the eye in the near field of radiofrequency sources at 380, 900 and 1800 MHz. Physics in Medicine and Biology 2007;52(12): 3335.
[26] Hutton DV. Fundamentals of Finite Element Analysis. Boston: McGraw-Hill: Higher Education; 2004.
[27] Wang H, Qin QH. FE approach with Green’s function as internal trial function for simulating bioheat transfer in the human eye. Archives of Mechanics 2010;62(6): 493-510.
[28] Bakker JF, Paulides MM, Neufeld E, Christ A, Kuster N, Rhoon GCv. Children and adults exposed to electromagnetic fields at the ICNIRP reference levels: theoretical assessment of the induced peak temperature increase. Physics in Medicine and Biology 2011;56(15): 4967.
[29] Niemz MH. Laser-Tissue Interactions-Fundamentals and Applications. 3th ed: Springer-Verlag; 2007.
[30] Scott JA. The computation of temperature rises in the human eye induced by infrared radiation. Physics in Medicine and Biology 1988;33(2): 243.
[31] Guiot C, Madon E, Allegro D, Piantà PG, Baiotto B, Gabriele P. Perfusion and thermal field during hyperthermia. Experimental measurements and modelling in recurrent breast cancer. Physics in Medicine and Biology 1998;43(10): 2831.
[32] Fuentes D, Walker C, Elliott A, Shetty A, Hazle JD, Stafford RJ. Magnetic resonance temperature imaging validation of a bioheat transfer model for laser-induced thermal therapy. International Journal of Hyperthermia : The Official Journal of European Society for Hyperthermic Oncology, North American Hyperthermia Group 2011;27(5): 453-64.
[33] Corvi A, Innocenti B, Mencucci R. Thermography used for analysis and comparison of different cataract surgery procedures based on phacoemulsification. Physiological Measurement 2006;27(4): 371.
[34] Ng EYK, Tan HM, Ooi EH. Boundary element method with bioheat equation for skin burn injury. Burns 2009;35(7): 987-97.
[35] Lang J, Erdmann B, Seebass M. Impact of nonlinear heat transfer on temperature control in regional hyperthermia. Biomedical Engineering, IEEE Transactions on 1999;46(9): 1129-38.
[36] Pfefer TJ, Barton JK, Smithies DJ, Milner TE, Nelson JS, van Gemert MJC, et al. Modeling laser treatment of port wine stains with a computer-reconstructed biopsy. Lasers in Surgery and Medicine 1999;24(2): 151-66.
[37] Ng EYK, Tan HM, Ooi EH. Prediction and parametric analysis of thermal profiles within heated human skin using the boundary element method. Philosophical Transactions of the Royal Society 2010. 655-78.

[38] Akbarzadeh A, Chen Z. Heat conduction in one-dimensional functionally graded media based on the dual-phase-lag theory. Proceedings of the Institution of Mechanical Engineers, Part C: Journal of Mechanical Engineering Science 2012.

[39] Ezzat MA, Fayik MA. Fractional fourier law with three phase lag of thermoelasticity. Mechanics of Advanced Materials and Structures 2013;20(8): 593-602.

[40] Marqa MF, Colin P, Nevoux P, Mordon SR, Betrouni N. Focal laser ablation of prostate cancer: numerical simulation of temperature and damage distribution. Biomedical Engineering Online 2011;10: 45.

[41] Shibib KS. Thermal damage due to incidental continuous CO2 laser irradiation on human skin. Thermal Science 2010;14(2): 451-58.

[42] Ansari MA, Massudi R. Study of short-pulse laser propagation in biological tissue by means of the boundary element method. Lasers in Medical Science 2011;26(4): 503-08.

[43] Deng ZS, Liu J. Monte Carlo method to solve multidimensional bioheat transfer problem. Numerical Heat Transfer, Part B: Fundamentals 2002;42(6): 543-67.

[44] Zhou JH, Chen JK, Zhang YW. Simulation of laser-induced thermotherapy using a dual-reciprocity boundary element model with dynamic tissue properties. IEEE Transactions on Biomedical Engineering 2010;57(2): 238-45.

[45] Liu J, Xu LX. Boundary information based diagnostics on the thermal states of biological bodies. International Journal of Heat and Mass Transfer 2000;43(16): 2827-39.

[46] Majchrzak E. Numerical modelling of bio-heat transfer using the boundary element method. Journal of Theoretical and Applied Mechanics 1998;36(2): 437-55.

[47] Xu F, Wang PF, Lin M, Lu TJ, Ng EYK. Qualification and the underlying mechanism of skin thermal damage: A review. Journal of Mechanics in Medicine and Biology 2010;10: 373-400.

[48] Erdmann B, Lang J, Seebab M. Adaptive solutions of nonlinear parabolic equations with application to hyperthermia treatments. Proc. CHT'97 - Advances in Computational Heat Transfer 1997;103-10.

[49] Nilsson A. Blood flow, temperature, and heat loss of skin exposed to local radiative and convective cooling. Journal of Investigative Dermatology 1987;88(5): 586-93.

[50] Miyamoto Y, Kaysser WA, Rabin BH, Kawasaki A, Ford RG. Functionally graded materials: Design, processing and applications. Kluwer Academic Publishers; 1999.

[51] Deng ZS, Liu J. Parametric studies on the phase shift method to measure the blood perfusion of biological bodies. Medical Engineering & Physics 2000;22(10): 693-702.

[52] Kim BM, Jacques SL, Rastegar S, Thomsen S, Motamedi M. Nonlinear finite-element analysis of the role of dynamic changes in blood perfusion and optical properties in laser coagulation of tissue. Selected Topics in Quantum Electronics, IEEE Journal of 1996;2(4): 922-33.

[53] Drizdal T, Togni P, Visek L, Vrba J. Comparison of constant and temperature dependent blood perfusion in temperature prediction for superficial hyperthermia. Radio Engineering 2010;19(2): 281-89.

[54] Jirousek J, Wróblewski A, Qin QH, He XQ. A family of quadrilateral hybrid-Trefftz p-elements for thick plate analysis. Computer Methods in Applied Mechanics and Engineering 1995;127(1–4): 315-44.

[55] Qin QH. Variational formulations for TFEM of piezoelectricity. International Journal of Solids and Structures 2003;40(23): 6335-46.

[56] Qin QH. Hybrid Trefftz finite-element approach for plate bending on an elastic foundation. Applied Mathematical Modelling 1994;18(6): 334-39.

[57] Jiang W, Zhong R, Qin QH, Tong Y. Homogenized finite element analysis on effective elastoplastic mechanical behaviors of composite with imperfect interfaces. International Journal of Molecular Sciences 2014;15(12): 23389-407.

[58] Ding KZ, Qin QH, Cardew-Hall M. A new integration algorithm for the finite element analysis of elastic-plastic problems. Proc of 9th International Conference on Inspection, Appraisal, Repairs & Maintenance of Structures, Fuzhou, China, 20-21 October: CI-Premier PTY LTD, ISBN: 981-05-3548-1; 2005. 209-16.

[59] Cao L, Qin QH, Zhao N. An RBF–MFS model for analysing thermal behaviour of skin tissues. International Journal of Heat and Mass Transfer 2010;53(7–8): 1298-307.

[60] Wang H, Qin QH. A meshless method for generalized linear or nonlinear Poisson-type problems. Engineering analysis with boundary elements 2006;30(6): 515-21.

[61] Wang H, Qin QH, Kang YL. A new meshless method for steady-state heat conduction problems in anisotropic and inhomogeneous media. Archive of Applied Mechanics 2005;74(8): 563-79.

[62] Wang H, Qin QH, Kang YL. A meshless model for transient heat conduction in functionally graded materials. Computational Mechanics 2006;38(1): 51-60.

[63] Wang H, Qin QH, Liang XP. Solving the nonlinear Poisson-type problems with F-Trefftz hybrid finite element model. Engineering Analysis with Boundary Elements 2012;36(1): 39-46.

[64] Cui Y-h, Qin QH, Wang J-S. Application of HT finite element method to multiple crack problems of Mode I, II and III. Chinese Journal of Engineering Mechanics 2006;23(3): 104-10.

[65] Katsikadelis JT. The analog equation method - a powerful BEM-based solution technique for solving linear and nonlinear engineering problems. In: C.A. B, editor. Boundary Element Method XVI. Southampton: CLM Publications; 1994. 167-82.

[66] Wang H, Qin QH. Some problems with the method of fundamental solution using radial basis functions. Acta Mechanica Solida Sinica 2007;20(1): 21-29.

[67] Gokul KC, Gurung DB, Adhikary PR. FEM approach for transient heat transfer in human eye. Applied Mathematics 2013;4(10B): 30-36.

[68] Qin QH, Huang Y. The study and prospect of solutions on the nonlinear problem of plates. Chinese Journal of Engineering Mechanics 1990;7(4): 10-18.

[69] Diao S, Qin QH, Dong J. On branched interface cracks between two piezoelectric materials. Mechanics Research Communications 1996;23(6): 615-20.

[70] Yu SW, Feng XQ, Qin QH. On several problems of macro/micro failure mechanics. Key Engineering Materials 1998;145: 51-60.

[71] Qin QH. On nonlinear solutions for dislocations in a bimaterial solid. Structural integrity and fracture: proceedings of the International Conference on Structural Integrity and Fracture, SIF 2002, Perth, Australia, 25-27 September 2002 2002: 71-79.

[72] Hong X-C, Qin QH. Bifurcation of limit cycles in a cubic hamiltonian system with some special perturbed terms. International Journal of Mathematical Sciences 2007;6(2): 187-98.

[73] Hong X-C, Qin QH. Bifurcation of limit cycles in two given planar polynomial systems. Recent Advances in Computer Science and Information Engineering 2012: 705-13.

[74] Trakic A, Liu F, Crozier S. Transient temperature rise in a mouse due to low-frequency regional hyperthermia. Physics in Medicine and Biology 2006;51(7): 1673.

[75] Feng Y, Fuentes D, Hawkins A, Bass J, Rylander M, Elliott A, et al. Nanoshell-mediated laser surgery simulation for prostate cancer treatment. Engineering with Computers 2009;25(1): 3-13.

[76] Chen Y CS, Rashed YF, Golberg MA. A mesh-free method for linear diffusion equations. Numerical Heat Transfer, Part B: Fundamentals 1998;33(4): 469-86.

[77] Golberg MAC, C.S. An efficient mesh-free method for nonlinear reaction-diffusion equations. Model Model Eng Sci 2001;2: 87-95.

[78] Qin QH, Ma H. A second-order scheme of precise time-step integration method for dynamic analysis with respect to long-term integration and transient responses. Applied Mathematical Modeling: Nova Science Pub Inc; 2008. 145-83.

[79] Balakrishnan K, Sureshkumar R, Ramachandran PA. An operator splitting-radial basis function method for the solution of transient nonlinear Poisson problems. Computers & Mathematics with Applications 2002;43(3–5): 289-304.

[80] Peaceman DW, H. H. Rachford J. The numerical solution of parabolic and elliptic differential equations. Journal of the Society for Industrial and Applied Mathematics 1955;3(1): 28-41.

[81] Flyckt VMM, Raaymakers BW, Kroeze H, Lagendijk JJW. Calculation of SAR and temperature rise in a high-resolution vascularized model of the human eye and orbit when exposed to a dipole antenna at 900, 1500 and 1800 MHz. Physics in Medicine and Biology 2007;52(10): 2691-701.

[82] Laakso I. Assessment of the computational uncertainty of temperature rise and SAR in the eyes and brain under far-field exposure from 1 to 10 GHz. Physics in Medicine and Biology 2009;54(11): 3393.

[83] Issa RI, Oliveira PJ. Numerical prediction of phase separation in two-phase flow through T-junctions. Computers & Fluids 1994;23(2): 347-72.

[84] Andreas K, Theodoros S. Numerical model of heat transfer in the human eye with consideration of fluid dynamics of the aqueous humour. Physics in Medicine and Biology 2010;55(19): 5653.

[85] Flyckt VMM, Raaymakers BW, Lagendijk JJW. Modelling the impact of blood flow on the temperature distribution in the human eye and the orbit: fixed heat transfer coefficients versus the Pennes bioheat model versus discrete blood vessels. Physics in Medicine and Biology 2006;51(19): 5007.

[86] Mainster MA, White TJ, Tips JH. Corneal thermal response to the CO2 laser. Applied Optics 1970;9(3): 665-67.

[87] Paruch M. Numerical simulation of bioheat transfer process in the human eye using finite element method. Scientific Research of the Institute of Mathematics and Computer Science 2007;6(1): 199-204.

[88] Narasimhan A, Jha KK. Bio-heat transfer simulation of retinal laser irradiation. International Journal for Numerical Methods in Biomedical Engineering 2012;28(5): 547-59.

[89] Brinkmann R, Geerling G, Kampmerier J, Koop N, Radt B, Birngruber R. Laser thermokeratoplasty: analysis of in vitro results and refractive changes achieved in a first clinical study. Proc SPIE 3192, Medical Applications of Lasers in Dermatology, Ophthalmology, Dentistry, and Endoscopy 1997;180.

[90] Wang H, Qin QH, Han MY. Hybrid finite element simulation for bioheat transfer in the human eye. In: Ng EYK, Acharya UR, Rangayyan RM, Suri JS, editors. Ophthalmological Imaging and Applications. New York: CRC Press; 2014. 409-25.

[91] Cao L, Qin QH, Zhao N. A new RBF-Trefftz meshless method for partial differential equations. IOP Conference Series: Materials Science and Engineering 2010;10: 012217.

[92] Gao Y, Wang H, Qin QH. Orthotropic Seepage Analysis using hybrid finite element method. Journal of Advanced Mechanical Engineering 2015;2(1): 1-13.

[93] Wang H, Qin QH, Kang YL. The method of fundamental solutions with radial basis functions approximation for thermoelastic analysis. Journal of Dalian University of Technology 2006;46(S1): 46-51.

[94] Wang H, Qin QH. Hybrid FEM with Fundamental solutions as trial functions for Heat Conduction Simulation. Acta Mechanica Solida Sinica 2009;22(5): 487-98.

[95] Wang H, Qin QH, Yao WA. Improving accuracy of opening-mode stress intensity factor in two-dimensional media using fundamental solution based finite element model. Australian Journal of Mechanical Engineering 2012;10(1): 41.

[96] Wang H, Qin QH. Numerical implementation of local effects due to two-dimensional discontinuous loads using special elements based on boundary integrals. Engineering Analysis with Boundary Elements 2012;36(12): 1733-45.

[97] Cao C, Qin QH. Hybrid fundamental solution based finite element method: theory and applications. Advances in Mathematical Physics 2015;2015: Article ID: 916029, 38 pages.

[98] Cao C, Yu A, Qin QH. Mesh reduction strategy: Special element for modelling anisotropic materials with defects. Proceedings of the 36th International Conference on Boundary Elements and Other Mesh Reduction Methods, 22 - 24 October, 2013, Dalian, China2013. 61.

[99] Qin QH. Fundamental solution based finite element method. J Appl Mech Eng 2013;2: e118.

[100] Qin QH, Mai YW. BEM for crack-hole problems in thermopiezoelectric materials. Engineering Fracture Mechanics 2002;69(5): 577-88.

[101] Qin QH. Nonlinear analysis of Reissner plates on an elastic foundation by the BEM. International Journal of Solids and Structures 1993;30(22): 3101-11.

[102] Wang H, Qin QH. Implementation of fundamental-solution based hybrid finite element model for elastic circular inclusions. Proceedings of the Asia-

Pacific Congress for Computational Mechanics, 11th-14th Dec 2013, Singapore2013.

[103] Ma H, Guo Z, Qin QH. Two-dimensional polynomial eigenstrain formulation of boundary integral equation with numerical verification. Applied Mathematics and Mechanics 2011;32(5): 551-62.

[104] Ma H, Yan C, Qin QH. Eigenstrain boundary integral equations with local Eshelby matrix for stress analysis of ellipsoidal particles. Mathematical Problems in Engineering 2014;2014: 947205.

[105] Ma H, Yan C, Qin QH. Local Eshelby matrix enhanced eigenstrain BIE for 3-d analysis of particles in full space. 11th World Congress on Computational Mechanics (WCCM XI), July 20 - 25, 2014, Barcelona, Spain2014.

[106] Qin QH. The Trefftz Finite and Boundary Element Method. Southampton: WIT Press; 2000.

[107] Qin QH. Trefftz finite element method and its applications. Applied Mechanics Reviews 2005;58(5): 316-37.

[108] Wang H, Qin QH. A fundamental solution-based finite element model for analyzing multi-layer skin burn injury. Journal of Mechanics in Medicine and Biology 2012;12(05).

[109] Wang H, Cao LL, Qin QH. Hybrid graded element model for nonlinear functionally graded materials. Mechanics of Advanced Materials and Structures 2012;19(8): 590-602.

[110] Cao LL, Wang H, Qin QH. Fundamental solution based graded element model for steady-state heat transfer in FGM. Acta Mechanica Solida Sinica 2012;25(4): 377-92.

[111] Zhao N, Cao LL, Qin QH. Application of Trefftz method to heat conduction problem in functionally graded materials. Recent Patents on Space Technology 2011;1(2): 158-66.

[112] Wang H, Qin QH. The method of fundamental solutions for thermoelastic analysis of functionally graded materials. Functionally Graded Materials 2012: 123-56.

[113] Wang H, Qin QH. Special fiber elements for thermal analysis of fiber-reinforced composites. Engineering Computations 2011;28(8): 1079-97.

[114] Wang H, Qin QH. A fundamental solution based FE model for thermal analysis of nanocomposites. Boundary Elements and Other Mesh Reduction Methods Xxxiii 2011;52: 191-202.

[115] Kompiš V, Murčinková Z, Rjasanow S, Grzhibovskis R, Qin QH. Computational simulation methods for composites reinforced by fibres. computational structural engineering. Proceedings of the International Symposium on Computational Structural Engineering, Held in Shanghai, China, June 22-24, 2009 2009: 63.

[116] Wang H, Han MY, Yuan F, Xiao ZR. Fundamental-solution-based hybrid element model for nonlinear heat conduction problems with temperature-dependent material properties. Mathematical Problems in Engineering 2013;2013.

[117] Qin QH, Wang H. Fundamental solution based FEM for nonlinear thermal radiation problem. 12th International Conference on Boundary Element and Meshless Techniques (BeTeq 2011), ed EL Albuquerque, MH Aliabadi, EC Ltd, Eastleigh, UK2011. 113-18.

[118] Wang H, Qin QH. Fundamental solution-based hybrid finite element analysis for non-linear minimal surface problems. Recent Developments in Boundary Element Methods: A Volume to Honour Professor John T Katsikadelis 2010: 309.

[119] Wang H, Qin QH. Fundamental-solution-based finite element model for plane orthotropic elastic bodies. European Journal of Mechanics-A/Solids 2010;29(5): 801-09.

[120] Wang H, Qin QH. Fracture analysis in plane piezoelectric media using hybrid finite element model. Proceedings of the 13th International Conference of fracture2013.

[121] Wang H, Qin QH. Fundamental-solution-based hybrid FEM for plane elasticity with special elements. Computational Mechanics 2011;48(5): 515-28.

[122] Qin QH, Wang H. Special circular hole elements for thermal analysis in cellular solids with multiple circular holes. International Journal of Computational Methods 2013;10(4): 1350008.

[123] Wang H, Qin QH. A new special element for stress concentration analysis of a plate with elliptical holes. Acta Mechanica 2012;223(6): 1323-40.

[124] Charny CK. Mathematical models of bioheat transfer. Advances in Heat Transfer 1992;22: 19-155.

[125] Ozisik MN. Heat Conduction. John Wiley & Sons; 1993.

[126] Shrivastava D, Vaughan JT. A generic bioheat transfer thermal model for a perfused tissue. Journal of Biomechanical Engineering 2009;131(7): 074506-06.

[127] Wang H, Qin QH. Computational bioheat modeling in human eye with local blood perfusion effect. In: E.Y.K. Ng JHT, U.R. Acharya, J.S Suri (ed.), editor. Human Eye Imaging and Modeling: CRC Press; 2012. 311-28.

[128] Brinkmann R, Koop N, Droege G, Grotehusmann U, Huber A, Birngruber R. Investigations on laser thermokeratoplasty. 1994. 120-30.

[129] Balakrishnan K, Ramachandran PA. The method of fundamental solutions for linear diffusion-reaction equations. Mathematical and Computer Modelling 2000;31(2-3): 221-37.

[130] Berger JR, Karageorghis A, Martin PA. Stress intensity factor computation using the method of fundamental solutions: mixed-mode problems. International Journal for Numerical Methods in Engineering 2007;69(3): 469-83.

[131] Chen J, Shieh H, Tsai J, Lee J. Equivalence between Trefftz method and method of fundamental solutions for the Green's function of concentric spheres using the addition theorem and image concept. Mesh Reduction Methods BEM/MRM XXXI, WIT Press; 2009.

[132] Qin QH, Wang H. Matlab and C programming for Trefftz Finite Element Methods: New York: CRC Press; 2008.

[133] Qin QH. Green's Function and Boundary Elements of Multifield Materials: Elsevier, Oxford; 2007.

[134] Chen W, Wang H, Qin QH. Kernel Radial Basis Functions. Computational Mechanics: Springer Berlin Heidelberg; 2009. 347-47.

[135] Wang H, Qin QH, Kang Y-l. The method of fundamental solutions with radial basis functions approximation for thermoelastic analysis. Journal of Dalian University of Technology 2006;46(S1): 46-51.

[136] Golberg MA, Chen CS, Bowman H, Power H. Some comments on the use of radial basis functions in the dual reciprocity method. Computational Mechanics 1998;21(2): 141-48.

[137] Cheng AHD. Particular solutions of Laplacian, Helmholtz-type, and polyharmonic operators involving higher order radial basis functions. Engineering Analysis with Boundary Elements 2000;24(7-8): 531-38.

[138] Bernal F, Kindelan M. On the enriched RBF method for singular potential problems. Engineering Analysis with Boundary Elements 2009;33(8–9): 1062-73.

[139] Chen CS, Kuhn G, Li J, Mishuris G. Radial basis functions for solving near singular Poisson problems. Communications in Numerical Methods in Engineering 2003;19(5): 333-47.

[140] Muleshkov AS, Golberg MA, Chen CS. Particular solutions of Helmholtz-type operators using higher order polyhrmonic splines. Computational Mechanics 1999;23(5): 411-19.

[141] Frahm K, Andersen O, Arendt-Nielsen L, Morch C. Spatial temperature distribution in human hairy and glabrous skin after infrared CO2 laser radiation. BioMedical Engineering 2010;9(1): 69.

[142] Ren Z, Liu J, Wang C, Jiang P. Boundary element method (BEM) for solving normal or inverse bio-heat transfer problem of biological bodies with complex shape. Journal of Thermal Science 1995;4(2): 117-24.

[143] Ng EYK, Chua LT. Comparison of one- and two-dimensional programmes for predicting the state of skin burns. Burns 2002;28(1): 27-34.

[144] Simpson CR, Kohl M, Essenpreis M, Cope M. Near-infrared optical properties of ex vivo human skin and subcutaneous tissues measured using the Monte Carlo inversion technique. Physics in Medicine and Biology 1998;43(9): 2465-78.

[145] Chen SS, Wright NT, Humphrey JD. Phenomenological evolution equations for heat-induced shrinkage of a collagenous tissue. Biomedical Engineering, IEEE Transactions on 1998;45(10): 1234-40.

[146] Mercer GN, Sidhu HS. A heat transfer model describing burns to the skin from automotive airbags. ANZIAM Journal 2005;47: 339-54.

[147] Xu LX, Zhu L, Holmes KR. Thermoregulation in the canine prostate during transurethral microwave hyperthermia, part II: blood flow response. International Journal of Hyperthermia 1998;14(1): 65-73.

[148] Zhang ZW, Wang H, Qin QH. Method of fundamental solutions for nonlinear skin bioheat model. Journal of Mechanics in Medicine and Biology 2014;14(4): 1450060.

[149] Zhang ZW, Wang H, Qin QH. Transient bioheat simulation of the laser-tissue interaction in human skin using hybrid finite element formulation. Molecular & Cellular Biomechanics 2012;9(1): 31-53.

[150] Ng EYK, Chua L. Mesh-independent prediction of skin burns injury. Journal of Medical Engineering & Technology 2000;24(6): 255-61.

[151] Golberg MA, Chen CS, Rashed YF. The annihilator method for computing particular solutions to partial differential equations. Engineering Analysis with Boundary Elements 1999;23(3): 275-79.

[152] Partridge PW, Brebbia CA, Wrobel LC. The dual reciprocity boundary element method. Computational Mechanics Publications; 1992.

[153] Wang H, Qin QH. Meshless approach for thermo-mechanical analysis of functionally graded materials. Engineering Analysis with Boundary Elements 2008;32(9): 704-12.

[154] Raaymakers BW, Kotte ANTJ, Lagendijk JJW. How to apply a discrete vessel model in thermal simulations when only incomplete vessel data are available. Physics in Medicine and Biology 2000;45(11): 3385.

[155] Hughes TJR, Pister KS, Taylor RL. Implicit-explicit finite elements in nonlinear transient analysis. Computer Methods in Applied Mechanics and Engineering 1979;17–18, Part 1(0): 159-82.

[156] Brebbia CA. Boundary Element Methods in Engineering 1982.

[157] Zhang ZW, Wang H, Qin QH. Meshless method with operator splitting technique for transient nonlinear bioheat transfer in two-dimensional skin tissues. International Journal of Molecular Sciences 2015;16(1): 2001-19.